MEASUREMENTS OF PROTON-PROTON AND PROTON-IRON INELASTIC CROSS SECTIONS USING CHARGED COSMIC RAY HADRONS OF ENERGY GREATER THAN 70 GeV

by

Gordon Dean DeMeester

A dissertation submitted in partial fulfillment
of the requirements for the degree of
Doctor of Philosophy
(Physics)
in The University of Michigan
1971

Doctoral Committee:

Professor Lawrence W. Jones, Chairman
Professor Frederick T. Haddock
Professor Alfred Z. Hendel
Associate Professor Gordon L. Kane
Professor Jens C. Zorn

ACKNOWLEDGEMENTS

I would like to thank Professor Lawrence W. Jones, my thesis advisor, and Dr. Donald E. Lyon, Jr., for their guidance, encouragement, and assistance which have been extremely valuable during the entire course of the experiment.

I am grateful to Dr. P. V. Ramana Murthy for his advice and guidance during my graduate work. The contributions to the data analysis by Dr. K. N. Erickson are greatly appreciated.

I would like to acknowledge the many others who have worked on the Echo Lake experiment. In particular Dr. A. E. Bussian, B. W. Loo, Dr. R. F. Roth, and P. R. Viswanath of The University of Michigan, Dr. D. D. Reeder, Dr. J. G. Learned, and R. J. Wilkes of the University of Wisconsin, W. Winter, R. Brown and J. Hicks of the Wisconsin Physical Sciences Laboratory, Dr. F. E. Mills of Brookhaven National Laboratory, and Dr. B. Cork of Argonne National Laboratory, for their efforts during the design, construction, and execution of the experiment.

I would like to express appreciation to the University of Denver for the use of their Echo Lake laboratory, and to the National Center for Atmospheric Research at Boulder, Colorado and the University of Wisconsin physics department for the use of their computing facilities during the earlier stages of the analysis.

This work was supported by the National Science Foundation.

Finally, I would like to thank my wife, Carol, for her patience, encouragement, and assistance in preparing this thesis.

ABSTRACT

MEASUREMENTS OF PROTON-PROTON AND PROTON-IRON INELASTIC CROSS SECTIONS USING CHARGED COSMIC RAY HADRONS OF ENERGY GREATER THAN 70 GeV

by

Gordon Dean DeMeester

Chairman: L. W. Jones

Proton-proton inelastic cross sections were measured at energies greater than 70 GeV by using cosmic ray hadrons that were incident on a liquid hydrogen target. The experiment was conducted at the University of Denver High Altitude Laboratory near Echo Lake, Colorado. It employed wide gap spark chambers on either side of the hydrogen target and an ionization calorimeter. The proton-proton inelastic cross section was found to be 32.4 ± 3.6 mb at 109 GeV and 32.3 ± 3.2 mb at 342 GeV. The particles that did not interact in the target but in the calorimeter were used both for a study of the calorimeter behavior and to determine the proton-iron inelastic cross section. This cross section was found to be 800 ± 7 mb in the energy interval from 70 to 900 GeV. There was no experimental evidence that either of these cross sections were energy dependent.

TABLE OF CONTENTS

LIST OF TABLES

LIST OF FIGURES

CHAPTER I. INTRODUCTION

One of the fundamental quantities in the study of strong interactions is the proton-proton total cross section. The size and energy dependence of this quantity are intimately related to many of the theories concerning the behavior of interacting particles. The cross section at very high energies is particularly useful for the comparison of various models and the understanding of strong interactions. The experiment described in this thesis was constructed to furnish the first direct experimental measurement of the proton-proton inelastic cross section above 70 GeV by using cosmic ray hadrons and a liquid hydrogen target. This cross section is related to the total cross section through the optical theorem and the slope parameter of differential elastic scattering which has been measured at accelerators for energies up to 70 GeV. An extrapolation of these accelerator measurements and a measurement of the inelastic cross section may be used to study the behavior of the total cross section at high energies. The flux of cosmic ray hadrons incident on the apparatus was about 75 percent protons and 25 percent charged pions. The results are corrected accordingly so that they correspond to proton-proton interactions.

This thesis also reports a proton-iron inelastic cross section between 70 and 800 GeV. Although this cross section does not have the fundamental importance of the proton-proton cross section, it is a valuable complementary result. This cross section was determined from

a study of interactions in the ionization calorimeter that was used to measure the energy of each incident hadron. Analysis of the calorimeter information also showed remarkable agreement with the calorimeter model of W. V. Jones [1]. The calorimeter results are significant inasmuch as they further the understanding of this important experimental tool for the energy measurement of very high energy particles.

A. Experimental Method

The three main features of the experiment were a liquid hydrogen target, wide gap spark chambers, and an ionization calorimeter. One feature of the experiment that is unique among cosmic ray experiments to date is the use of the liquid hydrogen target. The spark chambers were used to observe the charged hadrons entering the hydrogen target and the hadron and possibly the secondaries from an interaction leaving the target. From this information the ratio of the number of hadrons that interacted in the target and the number of those that did not interact in the target was deduced. This ratio was determined for each of several energy intervals from 70 to 1000 GeV. The proton-proton inelastic cross section was calculated from this ratio. The observed cross section required a large correction because of a systematically low energy measurement of events that interacted in the hydrogen coupled with the steeply falling cosmic ray hadron energy spectrum. This correction was studied in two ways. One was an experimental approach in which the correction was determined for the proton-nucleus interactions in the target walls, and that correction applied to the

proton-proton inelastic cross sections. The other way of studying systematic errors involved computer generation of interactions and simulation of the energy measurement in order to study the effect of the interaction coordinates on the energy determination. The first direct measurement of the inelastic cross section and of the properties of proton-proton interactions at energies greater than 70 GeV was the prime motivation for this experiment. The observed properties of the interactions in the liquid hydrogen are reported elsewhere [2].

An alternative method of measuring the total or inelastic cross section is an attenuation experiment. This method involves measuring a beam flux with and without a target in the beam path. With this method, the cross section is then determined from the ratio of the properly normalized transmitted fluxes measured with "target in" and "target out". Corrections required because of a systematically low energy measurement of particles that interact in the hydrogen are not necessary with this kind of analysis. However, the attenuation method requires both a longer run, and a way of doing a series of target full, target empty runs which does not include long term systematic biases.

A third method of measuring the inelastic cross section is to determine the average path length in target material before the first interaction occurs. This method, useful only with thick targets, was used to determine the interaction length of hadrons in iron and thus the proton-iron cross section.

Before a detailed description of this experiment is presented, some of the total and inelastic cross section measurements of other

experiments will be discussed. Most of the cross section measurements at accelerator energies were done using the attenuation method.

B. Proton-Proton Cross Section Measurements

Generally, at accelerator energies, proton-proton inelastic cross sections are not measured directly. Instead, the total and elastic cross sections are measured. These three quantities are related by $\sigma_T = \sigma_e + \sigma_i$, where the subscripts T, e, and i refer to the total, elastic, and inelastic cross sections, respectively. The results of total cross section measurements between 10 and 30 GeV are shown in Fig. 1. [3]. These measurements alone indicate that the total cross section is falling very slowly at higher energies. The solid line in Fig. 1, indicating the inelastic cross section at accelerator energies, is the difference between the total cross section measurements and the elastic cross section measurements of K. N. Foley et al. and D. Hartung et al. [4].

Significant proton-proton inelastic cross section measurements have been made at higher energies with data from the Proton Satellites 1, 2, and 3 [5]. In those experiments two targets were used. One target was polyethylene and the other was carbon. The values of the cross section were obtained using the difference method with associated errors of about 20 percent. The calorimeters used were made of iron and scintillator. However, the total thickness was about one-third that of the Echo Lake calorimeter. The final calculated proton-proton cross sections are shown in Fig. 1. These measurements are consistent

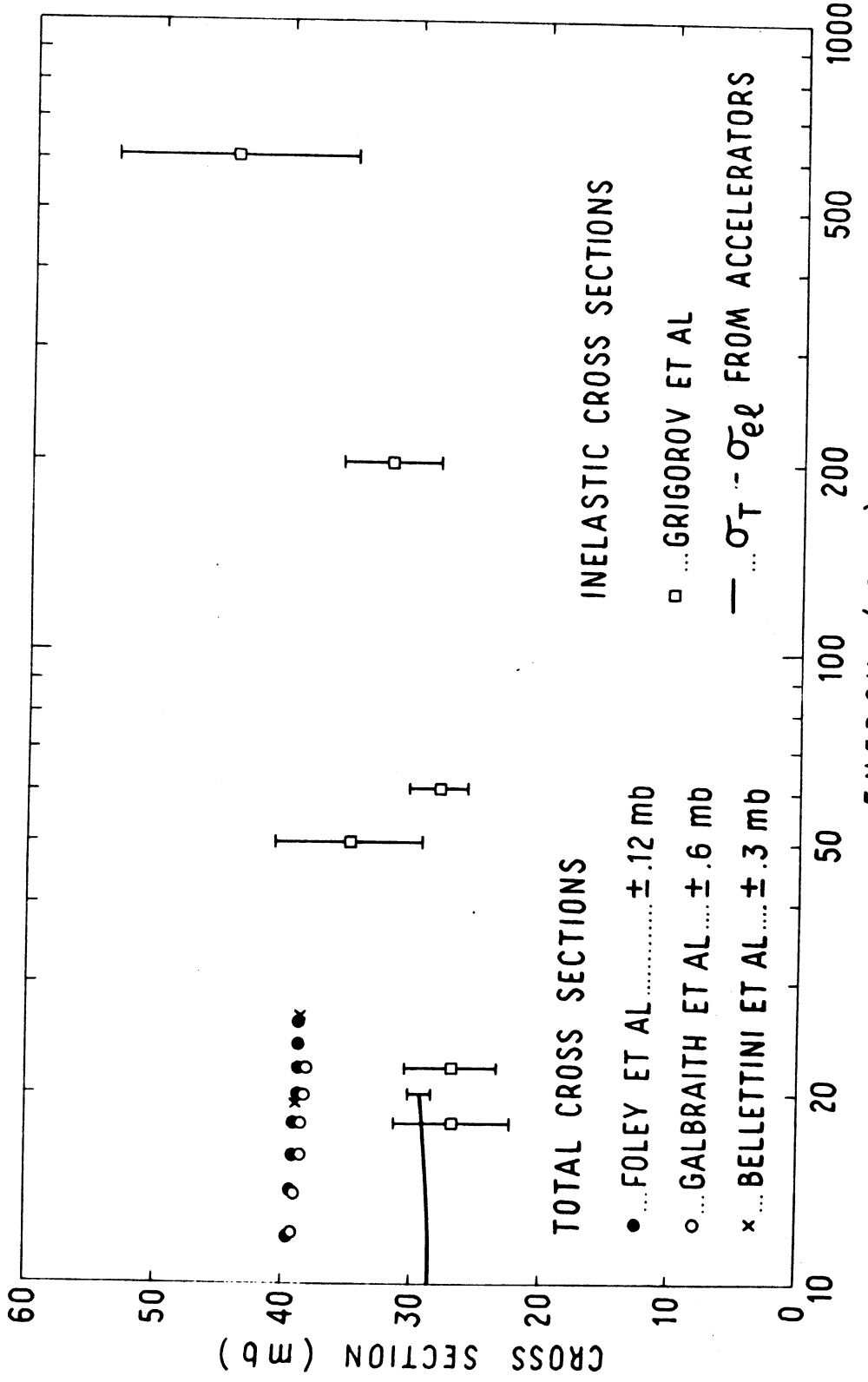

FIG. 1 HIGH ENERGY PROTON-PROTON CROSS SECTION DATA.

with a flat, or slowly rising, inelastic cross section. It is noteworthy that the proton-carbon cross sections measured in the same experiment are apparently rising with energy. The data fit the empirical relation

$$\sigma_{pC} = (216 \pm 7)\,[1. + (0.068 \pm 0.012)\,\log_e (E/20)] \qquad \text{(mb)}$$

between 20 and 600 GeV. The increase in the proton-proton cross section was reported to be consistent with this result.

C. Proton-Proton Cross Section Theory

Various models have been constructed to describe proton-proton interactions at very high energies. Some of the suggested optical and Regge models are discussed in this section. Two simple optical models are presented; one that treats the target nucleus as a sphere with constant opacity, the other with a Gaussian distribution of opacity. The optical model is used in Chapter IV to convert the observed hadron-iron cross section into a proton-iron cross section. Also, the optical model slope parameter of the differential elastic scattering peak extrapolated from accelerator measurements may be used to relate the measured inelastic cross section to the total cross section. The Regge models discussed in this section do not predict a cross section. Instead, experimental measurements of the total cross section may be used to determine parameters of the models. The results of this experiment are not sufficiently accurate to distinguish between the three Regge models discussed in this chapter.

Neglecting spin dependence, the asymptotic wave function of a plane wave incident on a scattering center is represented in the center of mass, (c.m.) coordinate system as

$$\psi = e^{i\vec{k}\cdot\vec{r}} + \frac{e^{ikr}}{r} f(\theta) \quad .$$

The plane wave is represented by the first term, $e^{i\vec{k}\cdot\vec{r}}$ and the scattered spherical wave is represented by the second term, $(e^{ikr}/r)f(\theta)$. The complex function $f(\theta)$ is the scattering amplitude and $\vec{k} = (\vec{p}_{cm}/h)$. The imaginary part of the scattering amplitude in the forward direction Im $f(0)$, is related to the total cross section by the optical theorem

$$\text{Im } f(0) = \frac{p_{cm}}{4\pi} \sigma_T \quad .$$

Optical models have been considered that treat the target nucleus as an opaque sphere that scatters an incoming plane wave [6]. Three variations of this model are discussed that differ in the opacity assigned to the target nucleus. They are expressed in an impact parameter representation, where b is the transverse distance between the lines of flight of the centers of the two nucleons. An impact parameter expansion of the scattering amplitude is defined by

$$f(x) = 2k \int_0^\infty h(b)\, J_o(bx)\, b\, db \quad .$$

The function $J_o(bx)$ is the zeroth order Bessel function with the argument bx, where $x = \sqrt{-t}$ and t is the relativistic four momentum transfer. A useful form of the complex function h(b), is

$$h(b) = \frac{a_b - 1}{2i} \quad .$$

An optical model with constant opacity, (1 - a), has the scattering amplitude,

$$f(\theta) = ik(1 - a) \int_o^R bJ_o(kb\theta)\, db \quad .$$

This pure imaginary scattering amplitude results in total, elastic, and inelastic cross sections which are

$$\sigma_T = 2\pi R^2(1 - a) \quad ,$$

$$\sigma_e = \pi R^2(1 - a)^2 \quad ,$$

$$\sigma_i = \pi R^2(1 - a^2) \quad .$$

If, instead of a constant, the opacity is assumed to be Gaussian in the impact parameter

$$1 - a_b = \alpha \exp(-5b^2/2R^2) \quad ,$$

then the scattering amplitude is

$$f(\theta) = ik\alpha \int_o^\infty b \exp\left[-\frac{5}{2}\frac{b^2}{R^2}\right] J_o(kb\theta)\, db \quad .$$

This amplitude results in total and elastic cross sections which are

$$\sigma_T = \frac{4\pi}{5} \alpha R^2$$

and

$$\sigma_e = \frac{\pi}{5} \alpha^2 R^2 \ .$$

Differential elastic scattering measurements and these optical models may be used to obtain a value of the total cross section calculated from a measurement of the inelastic cross section. In both of the optical models discussed, the diffraction scattering differential cross section at small scattering angles and a specified energy is given by

$$\frac{d\sigma}{dt} = \frac{\sigma_T^2}{16\pi\hbar^2} e^{+At} \ .$$

The scattering amplitude must be totally imaginary for this equation to be correct. From existing accelerator data the ratio of the real to the imaginary parts of the scattering amplitude is small and decreases with increasing energy [7]. The parameter A, is a slope parameter determined by accelerator experiments to be slowly increasing with energy. G. G. Beznogikh et al. [8] report that in the energy range of 12 to 70 GeV, the slope parameter A, as a function of total energy squared s, in GeV^2 is

$$A = (6.8 \pm 0.3) + (0.94 \pm 0.18) \log_e (s) \ .$$

The experimental measurements to determine this parameter were in the four momentum transfer interval

$$0.008 < |t| < 0.12 \qquad (\text{GeV/c})^2 .$$

Assuming that the differential cross section formula holds approximately at all t, integration over all four momentum transfers results in an elastic cross section

$$\sigma_e = \frac{1}{16\pi\hbar^2 A}\sigma_T^2 .$$

Therefore, the total cross section is

$$\sigma_T = \frac{\sigma_T^2}{16\pi\hbar^2 A} + \sigma_i$$

or

$$\sigma_T = \frac{B}{2} - [(B/2)^2 - B\sigma_i]^{1/2} ,$$

where

$$B = 16\pi\hbar^2 A .$$

This equation relates the total cross section to the measured inelastic cross section. As an example, at 20 GeV/c the slope parameter is about 8.2 $(\text{GeV/c})^{-2}$ [9] and the inelastic cross section is about 29.5 mb, therefore

$$B = (2.178 \times 10^{-47}\ \text{GeV}^2\ \text{sec}^2) \cdot 8.2(\text{c/GeV})^2 = 160.7\ \text{mb}.$$

This value of B, when used in the expression for the total cross section, gives

$$\sigma_T = 38.9 \text{ mb} \quad ,$$

that is to be compared with a total cross section measurement of 39 mb.

Difficulties are encountered with optical models in fitting the elastic differential cross section data over a large range of $|t|$. In order to fit his experimental data, A. Krisch [10] stressed the need for three types of strong interactions with an elastic differential cross section fit by a superposition of three exponentials with the variable $p_\perp^2$, the transverse momentum squared. This model however, does not successfully predict angular distributions or the measured values of the ratio of the real to imaginary part of the scattering amplitude in the forward direction.

By introducing complex angular momenta, the relativistic scattering amplitude, A(s,t), has been written as a sum of terms coming from simple poles which are the only singularities in the upper half of the complex angular momentum plane. With the proper approximations and assumptions at very high energies the relativistic scattering amplitude, A(s,t), is

$$A(s,t) = \sum_k \beta_k(t) \frac{1 - \eta_k e^{-i\pi\alpha_k(t)}}{\sin \pi\alpha_k(t)} \left[\frac{s}{s_k}\right]^{\alpha_k(t)} \quad ,$$

where the residue, $\beta_k(t)$, contains all the t-dependent terms. The sum extends over all relevant Regge poles. η_k is a signature factor, and s_k is a scale energy. The quantities s and t are the well-known relativistic invariants and $\alpha(t)$ is the Regge trajectory often approximated by the linear form $\alpha(t) = \alpha_o + \alpha_1 t$.

Regge pole models have been constructed which furnish a phenomenological description of most accelerator data and which may be used to project observed trends to asymptotic energies [11], [12]. The existence and contributions of various trajectories which are included in the model model as contributing to the scattering amplitude constitutes the difference between many of the models.

The t-channel Regge poles may be associated with observed meson states. In an application of such a model, Barger and Olsson [12] include only neutral non-strange vector and tensor meson state contributions to the total cross section. In addition to the trajectories associated with these mesons, a Pomeranchuk trajectory with maximal intercept $\alpha_p(0) = 1$ was introduced to give constant asymptotic cross sections. Fitting accelerator data with this model, the proton-proton total cross section at 1000 GeV was about 36 mb and at asymptotic energies about 35.7 mb.

Cabbibo, Horwitz, Kokkedee, and Ne'eman [13] proposed a model using "an algebra of currents" and some quark considerations. There was no Pomeranchuk contribution to the scattering amplitude and the intercepts of the two trajectories, $\alpha_p'(0)$ and $\alpha_s(0)$, were less than one. This resulted in a slowly vanishing asymptotic cross section. A fit

of this model to accelerator data indicated a proton-proton total cross section of 31 mb at 1000 GeV.

Frautschi and Margolis [14] proposed a model which includes both Regge poles and a contribution to the scattering amplitude from a vacuum Regge cut. Negative contributions to the amplitude from this cut result in a proton-proton total cross section which approaches from below an asymptotic limit. They estimated the asymptotic total cross section with corrections for secondary trajectories to be about 55 mb. More recently, in an attempt to explain the experimental results from Serpukhov of negative mesons interacting with protons, Barger and Phillips [15] have used a similar model. They also used this model in a fit to the proton-proton total cross section data and predict an asymptotic limit of 46 mb.

One of the definite restrictions on the growth of the total cross section is the Froissart bound [11]. This result proved from the axioms of quantum field theory states

$$\sigma_T(s) = C \log_e^2 \left[\frac{s}{s_o}\right] \quad \text{as} \quad s \to \infty .$$

D. Survey of Proton-Iron Inelastic Cross Sections

Proton-nucleus absorption cross sections have been studied both at accelerators and in cosmic ray experiments. G. Bellettini, G. Cocconi et al. [16] reported proton-nucleus absorption cross sections at 20 GeV from an experiment conducted at CERN. In that experiment it was shown that the absorption cross section was proportional to the

area covered by the nuclei, $A^{2/3}$, where A is the atomic number. Interpolation between their reported absorption cross sections for aluminum and copper results in a calculated proton-iron cross section of 800 mb. The total cross sections were determined to one or two percent, but the calculation of the elastic cross section had associated errors of five percent. The inelastic cross section which is the difference between the total and elastic cross sections has possible errors of six or seven percent. More recently, J. Engler et al. [17] reported neutron-nucleus total cross sections which were used in a similar fashion to calculate a proton-iron inelastic cross section of 727 mb at 21 GeV/c. In this calculation the ratio of inelastic to total cross section determined by G. Bellettini was applied to Engler's measurements with similar errors.

At energies higher than this, absorption cross section data is reported from experiments using cosmic rays as incident hadrons. Two different kinds of experiments will be mentioned. One is a "bad geometry" absorption experiment and the other an interaction length measurement using a calorimeter.

The "bad geometry" type of experiment is an attenuation experimen comparing the observed counting rate of a detector, above a set energy threshold, with and without an absorber in the "beam." A proton-iron absorption cross section of 610 ± 30 mb was determined in this way by Brenner and Williams [18] in an experiment conducted at Echo Lake, Colorado.

Calorimeter experiments determine absorption cross sections on the basis of the distribution of interaction depths of the incident hadrons. The two best examples of previously reported measurements of this type are the experiments of N. A. Dobrotin et al. [19] and E. L. Andronikashivili et al. [20] . The results of this latter group are similar to the results obtained in this experiment. They reported a hadron-iron interaction length of 130 ± 6 gm/cm^2 corresponding to an absorption cross section of 710 ± 35 mb over the energy range of 50 to 1000 GeV.

CHAPTER II. THE EXPERIMENT

A. General Description

The experiment described in this thesis was conducted at the University of Denver High Altitude Laboratory near Echo Lake, Colorado. The experimental site is at a height of 3231 m above sea level, or at a depth in the atmosphere of 715 gm/cm^2. This location was chosen in order to obtain a reasonable flux of unaccompanied cosmic ray hadrons. The flux of hadrons is attenuated in the atmosphere so that the flux with energy greater than 100 GeV at sea level is about 7 percent of the flux at Echo Lake. The experimental apparatus had a useful admittance (solid angle-area product) of 0.94 m^2 sr and a trigger rate of about 20 incident hadrons per hour with energy above 90 GeV.

Both the intensity and the constituents of the unaccompanied hadron flux have been studied by various groups at different altitudes [21]. The surviving primary proton flux was the desired beam of incident particles. However, the hadron flux that triggered the apparatus consisted of both pions and protons. The pions were produced in the interactions of the primary cosmic ray flux with the atmosphere above the apparatus. In order to eliminate hadrons that were accompanied by other secondaries from a previous collision an array of anti-coincidence shower counters was placed around the hydrogen target in its midplane. This array of counters, altogether 7.68 m^2, was used to eliminate most of the pion flux and reject all hadrons with accompanying particles

that simultaneously deposit energy in the calorimeter. The fraction of pions in the "beam" was calculated in this experiment so that the appropriate small correction could be made to the measured cross sections. This correction was 8 percent for the proton-proton cross section and 6 percent for the proton-iron cross section.

The experimental arrangement is shown in Fig. 2. The system was triggered when an unaccompanied charged particle traversed the top counter and more than a threshold energy of either 36 or 90 GeV was deposited in the calorimeter. Each event consisted of a charged cosmic ray hadron which satisfied the triggering requirements, passed through the top wide gap spark chamber, possibly interacted in the liquid hydrogen target, and continued alone or with secondaries into a second wide gap spark chamber and the ionization calorimeter. The two wide gap spark chambers were used to obtain a photographic record of the tracks in each spark chamber. The photographs of two events, one which interacted in the hydrogen and one which did not, are shown in Figs. 3 and 4, respectively. The coordinates and direction cosines of hadrons entering and leaving the target were determined from the measurement of tracks on the film. The ionization calorimeter was used to measure the energy of each event as well as to provide the energy estimate used in the trigger. The top 200 gm/cm^2 of the calorimeter was a series of ten iron plate spark chambers with 1.9 cm gaps. This set of spark chambers was used to observe the range of secondaries in order to differentiate between δ-rays and hadronic secondaries. The spark chambers, hydrogen target, ionization calorimeter, and associated

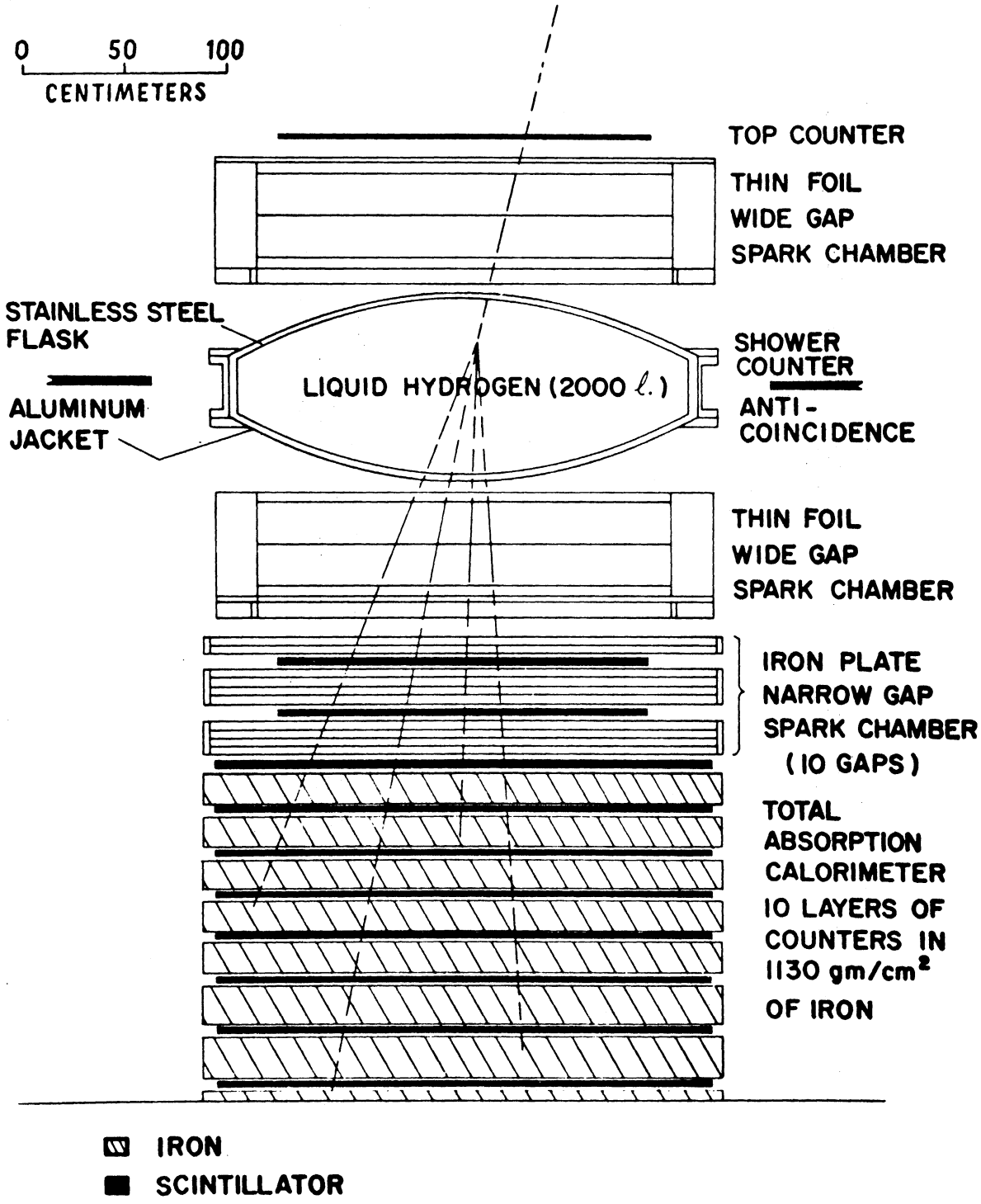

FIG. 2 FRONT VIEW OF EXPERIMENTAL ARRANGEMENT.

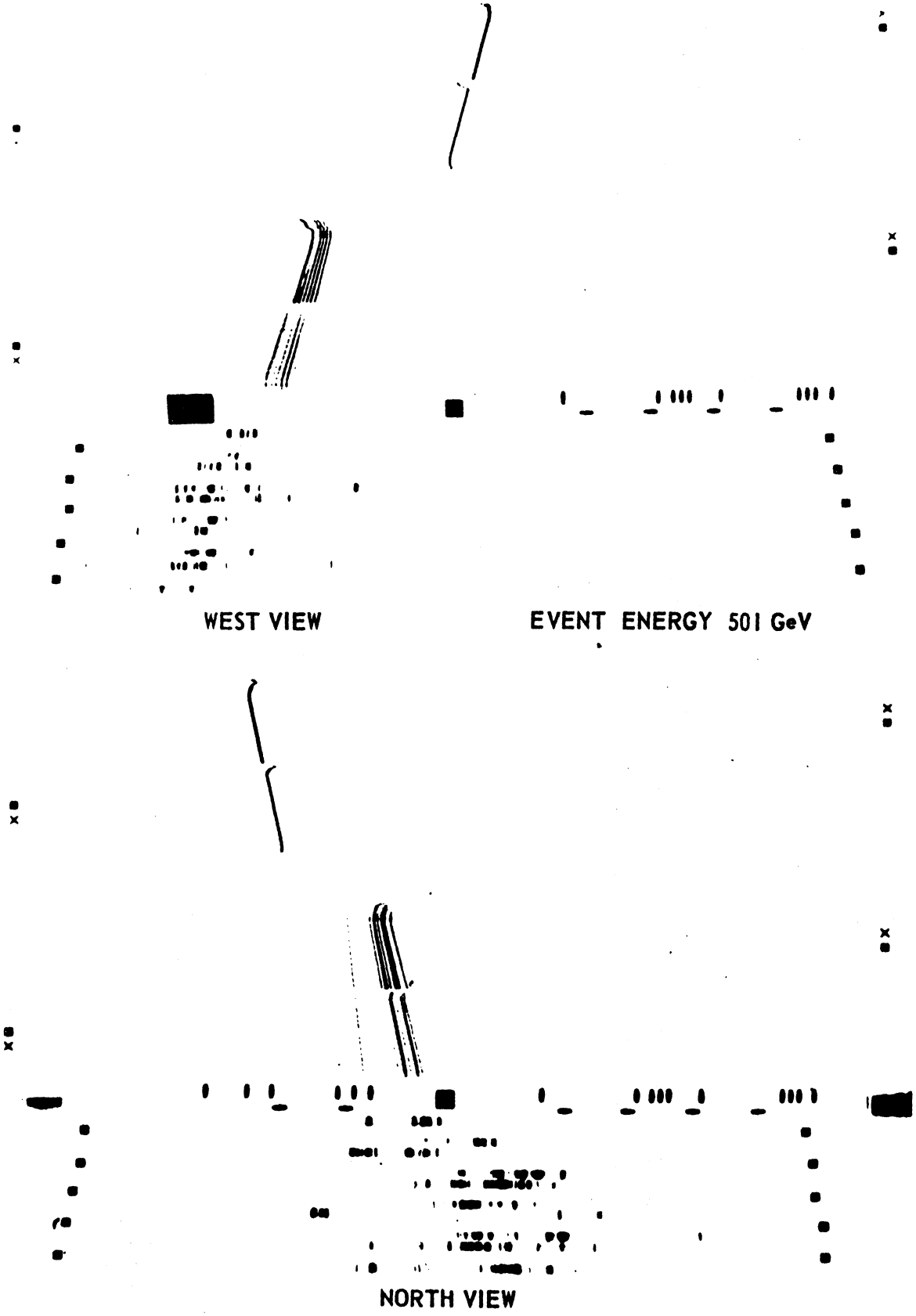

FIG. 3 EXAMPLE OF THE TWO STEREO PHOTOGRAPHS OF AN INTERACTING EVENT.

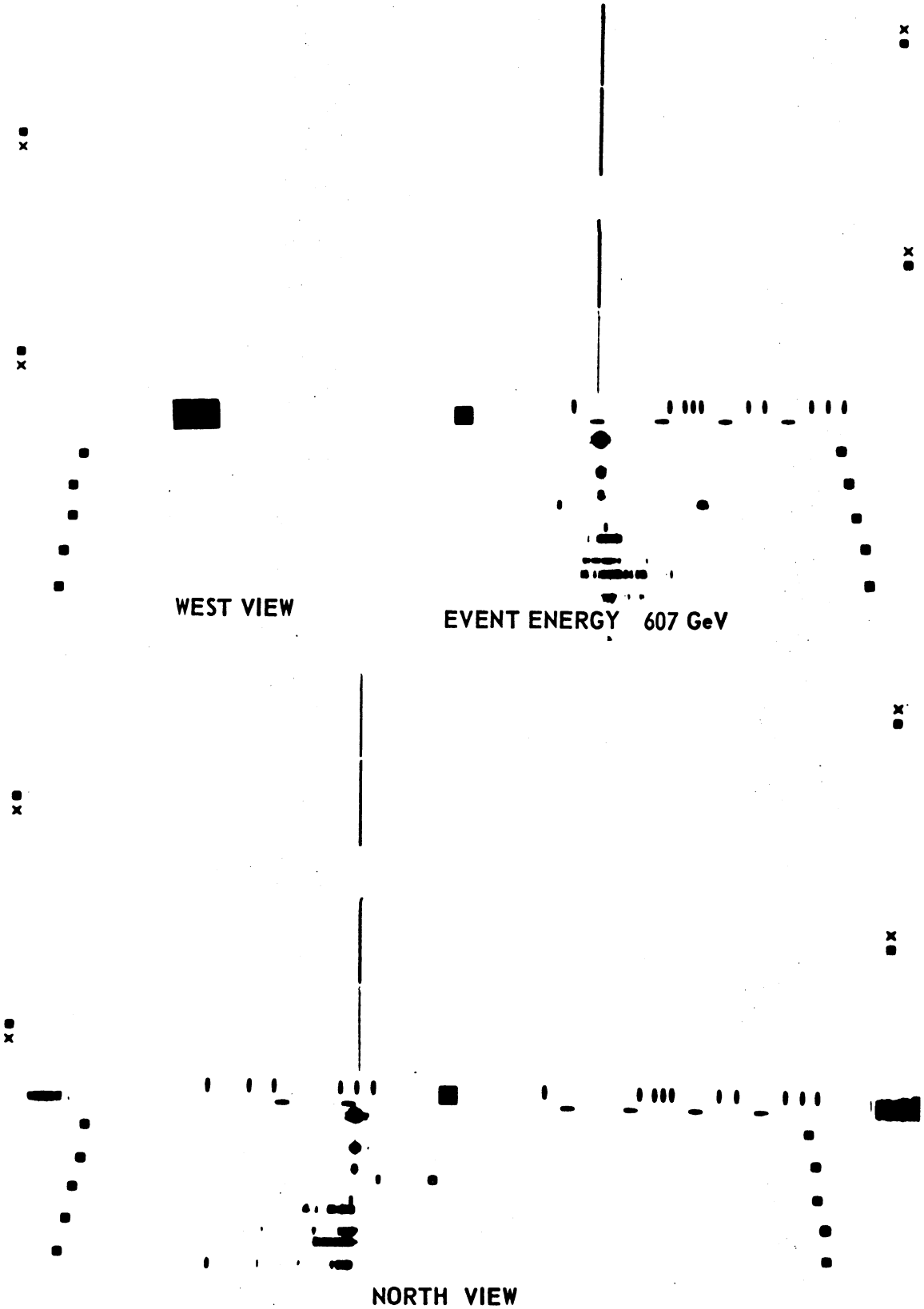

FIG. 4 EXAMPLE OF THE TWO STEREO PHOTOGRAPHS OF AN EVENT WHICH DID NOT INTERACT IN THE TARGET.

electronics and optics will be described in detail in the following sections. The calibration procedure will also be discussed. More detailed discussions of the energy measurement are presented in the next chapter.

B. Spark Chambers and Optics

The two wide gap spark chambers used to determine the trajectory of charged tracks were constructed with two 20.3 cm gaps in which sparks were photographed. A center foil of 0.0051 cm aluminum was pulsed by a Marx generator for each event and the sparks developed in 20.3 cm gaps between this foil and two similar ones on either side of it. There was a 5.1 cm dummy gap above the upper foil and below the lower one so that all three foils were suspended in the same way and the distance between them would be the same everywhere. They were suspended from a 2 x 2 m^2 frame of 1.22 cm thick plate glass. The relative intensity of the sparks in the two gaps was controlled by resistance between the two outer foils and the Marx generator ground. In order to eliminate spark distortion due to a fringe field of the spark chamber foils, closed loops of wire were wrapped around the glass every 1.27 cm. Between each successive loop were four 4.7 kΩ resistors forming a string of 16 resistors across each gap in each of the four corners of the spark chamber. These resistors resulted in an effective resistance of 9.4 kΩ between the center foil and Marx generator ground and established a constant voltage gradient at the glass to eliminate a fringe field.

Standard "spark chamber neon" (90 percent Ne, 10 percent He) was used and good multiple spark efficiency was achieved in the spark

chambers. To maintain gas purity, this gas was continuously recirculated at 100 ℓ/hr through a hot calcium oven and a container of Linde grade 13 molecular sieve at liquid nitrogen temperature.

The Marx generators consisted of eight Barium Titanate capacitors of 3900 pF each. These were charged in parallel to +14 kV and discharged in series dividing the available charge between the capacitance of the Marx generator and the 300 pF of the spark chamber. The first stage was triggered with a -12 kV pulse from a Science Accessories pulser. With this system the spark chambers were charged and the voltages clipped by the sparks about 150 nsec after a coincidence indicated an interesting event. If no spark developed, the resistor strings used to form a constant voltage gradient at the glass discharged the chamber with an RC time constant of 5 μsec.

Ten narrow gap spark chambers formed the initial 200 gm/cm^2 of the calorimeter. Each of these spark chambers was constructed from two 203 x 254 cm^2 iron plates 1.27 cm thick, one of which was on either side of a 1.91 cm spark gap. The spark chambers were stacked one on top of the other except where the scintillators for the first two layers of the calorimeter were inserted. They were viewed through 2.54 cm of lucite and each had ten internal epoxy-fiberglass 1.27 cm diameter pillars to support the weight of the iron above the gaps. The spark chambers were pulsed in pairs by a bank of five paralleled 3900 pF capacitors charged to 12 kV. A Science Accessories pulser primed the spark gaps to apply the stored charge of the capacitor banks to the spark chambers. No clearing field and no recirculation of gas were

necessary. There were 6 cc of ethyl alcohol added to the iron plate spark chamber neon to reduce edge sparking.

Each event in the spark chambers was photographed in 90 degree stereo along with binary coded information displayed on neon data lights. Two Giannini "Flight Research" model number 204, 35 mm cameras equipped with Leitz 120 mm lenses were used with Eastman Kodak Tri-X film. A system of front surfaced mirrors, made by sandwiching honeycomb metal with glass, was used to arrange the information on the film with a demagnification of 65.5:1 at the center of the spark chambers.

C. Hydrogen Target

Figure 5 shows details of the construction of the liquid hydrogen target which was designed and built at Lawrence Radiation Laboratory (LRL). Liquid hydrogen was contained within an inner flask made of 304 stainless steel. The useful volume of hydrogen was defined by a vertical cylinder 34.3 cm tall and 205.7 cm in diameter, covered on the ends by spherical sections with a radius of 205.7 cm. The spherical sections of the inner steel flask were 0.12 cm thick and of the outer aluminum jacket were 0.76 cm thick. This much aluminum in the "beam line" was required in order that the target meet the LRL safety requirements. The stainless steel flask was required to withstand an internal test pressure of 2.11 kg/cm^2 at room temperature. At liquid hydrogen temperature the flask could withstand about twice this pressure. The aluminum vacuum jacket was required to withstand an internal pressure of 7.03 kg/cm^2 and an external pressure of 1.41 kg/cm^2. The area between the flask and the outer aluminum vessel was evacuated to a pressure of 10^{-7} Torr. The vacuum minimized convective heat transfer

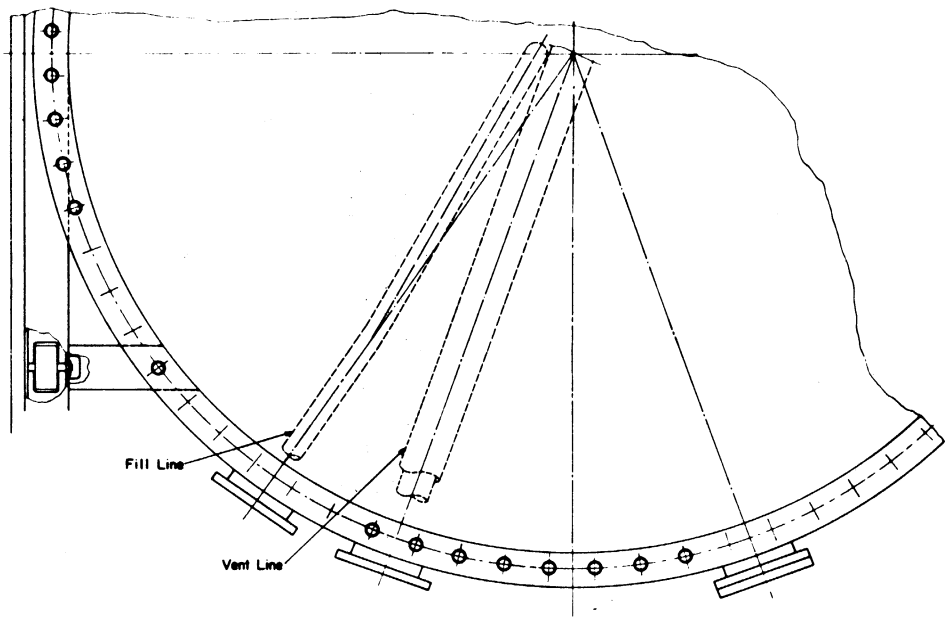

PLAN VIEW

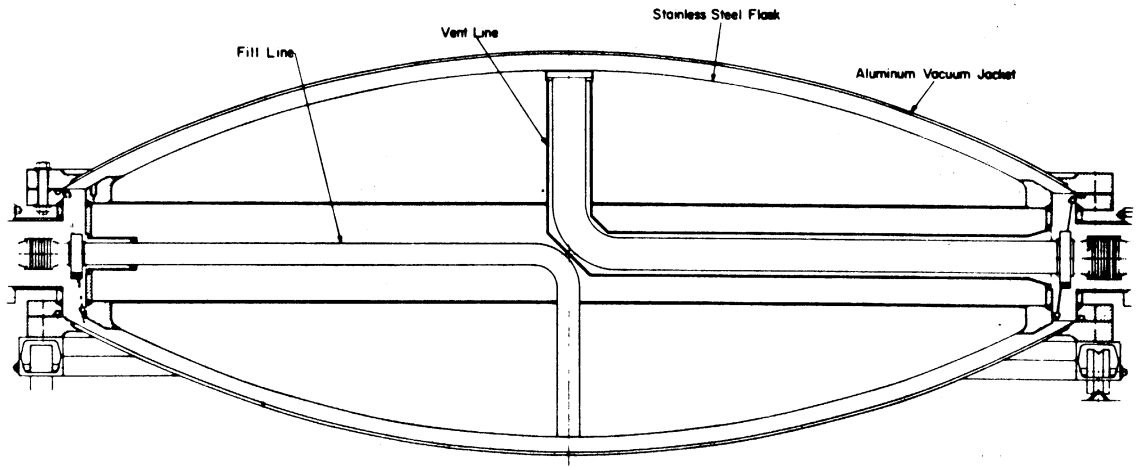

SECTION THROUGH FILL AND VENT LINES

FIG. 5 DETAILED DRAWING OF THE LIQUID HYDROGEN TARGET.

while twenty-five layers of superinsulation (6.35×10^{-4} cm aluminized mylar) reduced radiative heat transfer. The stainless steel flask was suspended around its periphery by 96 stainless steel 0.25 cm diameter rods 27.9 cm long. Calrod heaters were installed in the lower rim of the inner flask in case quick emptying was deemed advisable. The fill and vent lines extended to the center of the flask to minimize thermal stresses, especially during cool down. The heat gain of the inner vessel from the stainless steel rods, the fill and vent lines, the wires to the Calrod heaters, and from radiative and convective heat transfer was 26.7 watts.

There were two sets of carbon resistors to monitor the liquid level in the target. One set was in the fill line. The other was attached to the vertical sections of the fill and vent lines in the center of the target. The highest of the "calibration resistors" in the fill line was 2.15 cm below the highest part of the dome of the inner flask. The first thirty resistors in the fill line were spaced by 0.794 cm and the next ten by 1.588 cm. The first of the twelve resistors in the center of the target was 1.77 cm from the upper dome. These resistors were spaced by 8.08 cm. Voltage momentarily applied across a resistor would indicate at least a 30 percent difference in resistance between resistors in liquid or gaseous hydrogen. This was due to poorer heat dissipation of resistors in gas compared to those in liquid. Except for a few "calibration fills," the only time recorded was when the liquid level passed the internal flask resistors. The

boil off rate remained constant at about 72 liters per day. Figure 6 indicates the depth of hydrogen in the center of the target as a function of time. The liquid in the flask was "topped off" every seven to ten days.

D. Ionization Calorimeter

The hadrons that entered the calorimeter interacted and produced secondaries that either decayed or interacted again. The energy measurement of the calorimeter is based on the total energy deposited in the iron and scintillator by the primary particle and all the secondary particles produced when the primary particle interacts in the calorimeter. The hadronic and electromagnetic cascades produced ionization as the particles lost energy in the iron, ultimately transforming the energy of the incident particle into heat. Hadrons with greater than 70 GeV incident on a thick iron absorber lost less than one percent of their energy as neutrinos and muons [22]. The mechanics of the cascade process and the fraction of the total energy that is not observable as ionization is discussed in Appendix A. The ionization of the hadronic and electromagnetic cascades was sampled by ten layers of plastic scintillator inserted into the iron. The light observed in the scintillators by photomultiplier tubes was measured, calibrated with respect to the light observed when a single muon traversed the scintillator, and used to determine the energy of the incident hadron.

Many of the general features of the ionization calorimeter were shown in Fig. 2. The iron plates of the narrow gap spark chambers

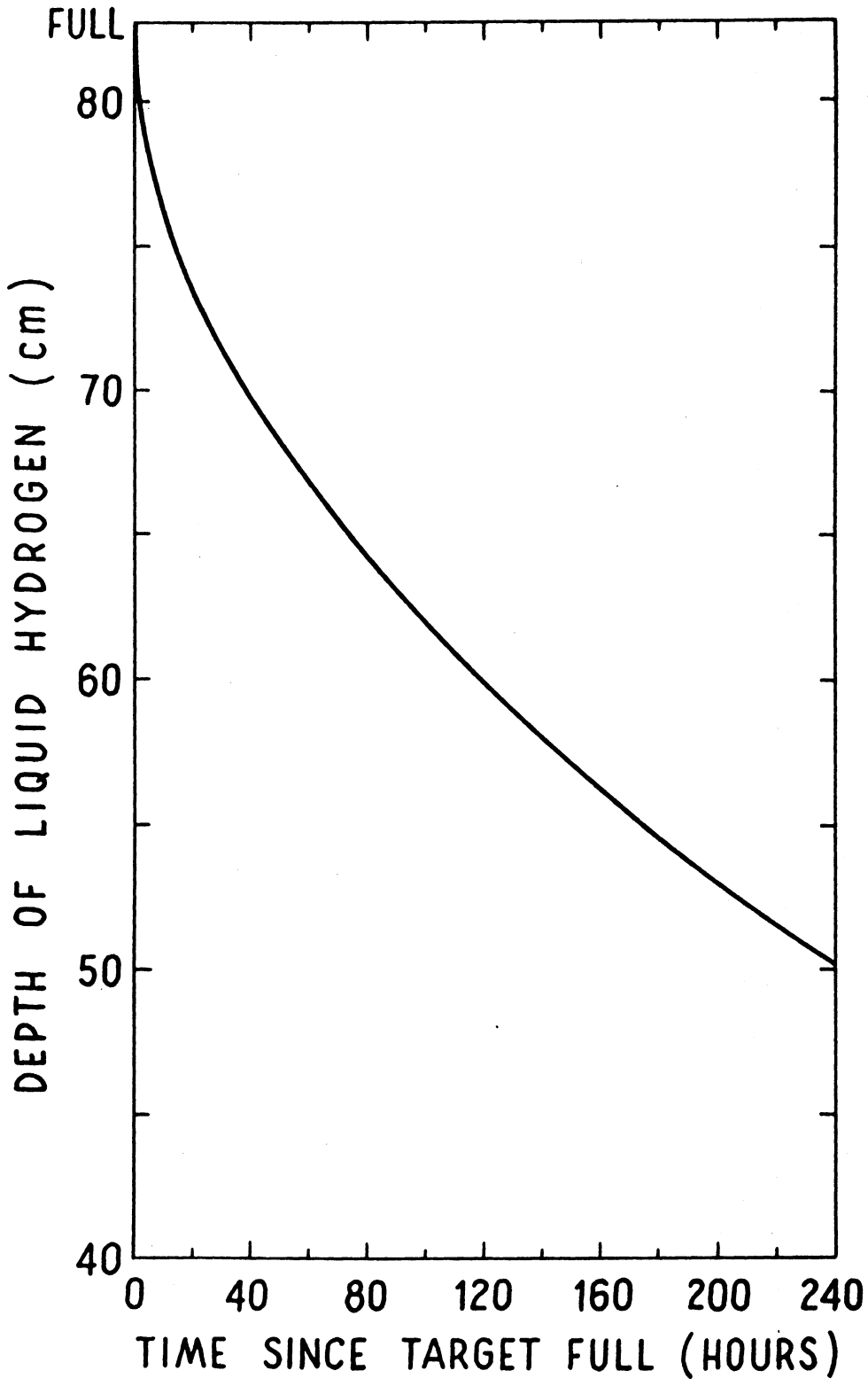

FIG. 6 DEPTH OF HYDROGEN IN THE TARGET AS A FUNCTION OF TIME.

previously described constitute the top 200 gm/cm^2 of the calorimeter. The remainder was constructed of 254 x 254 cm^2 plates of 1.27 cm thick iron. Layers of plastic scintillator were incorporated in the stack of iron about every proton interaction length. The scintillators sampled the ionization in the nuclear-electromagnetic cascade initiated by an incident hadron. Table I presents details of the size and placement of the scintillator layers, the two types of photomultiplier tubes used, and the thickness of iron from the top of the calorimeter down to the various scintillator layers. The thickness in gm/cm^2 of iron was determined using a density of 7.87 gm/cm^2 for the 1.27 cm thick iron plates. The vertical location of the scintillator layers is indicated with respect to a coordinate system with an origin at the center of the hydrogen target. The top counter and layers 1, 2, and 10 of the calorimeter were made of Pilot A scintillator. Layers 3 through 9 were made of Nuclear Enterprises NE102 scintillator.

At each place where a scintillator layer was inserted in the stack of iron there was a 1.27 cm rib in the center of the calorimeter to help support the accumulated weight of iron. This rib divided the calorimeter into two distinct halves. On either side of it two squares of scintillator were placed side by side in physical contact and wrapped in an aluminum, light-tight package. The scintillator packages were viewed through light pipes on both ends by a total of four photomultiplier tubes as indicated in Fig. 7. The area of the scintillator listed in Table I is half of a calorimeter layer or one of these packages.

Table I

Details of Placement and Size of Scintillators in the Calorimeter

Scintillator Layer	z-Coordinate (cm)	Depth of Iron from top of Calorimeter (gm/cm^2)	Area of One Side (m^2)	Thickness of Scintillator (cm)	Type of Photomultiplier Tubes
Top Counter Layer	120.13		0.914x1.829	1.91	RCA 6810
1	-131.3	40	0.914x1.829	1.91	RCA 6810
2	-155.7	120	0.914x1.829	1.91	RCA 6810
3	-184.9	210	1.219x2.438	3.81	EMI 9816
4	-205.8	330	1.219x2.438	3.81	EMI 9816
5	-226.4	450	1.219x2.438	3.81	EMI 9816
6	-247.6	570	1.219x2.438	3.81	EMI 9816
7	-267.6	690	1.219x2.438	3.81	EMI 9816
8	-287.9	810	1.219x2.438	3.81	EMI 9816
9	-313.7	970	1.219x2.438	3.81	EMI 9816
10	-338.8	1130	1.219x2.438	1.91	EMI 9816

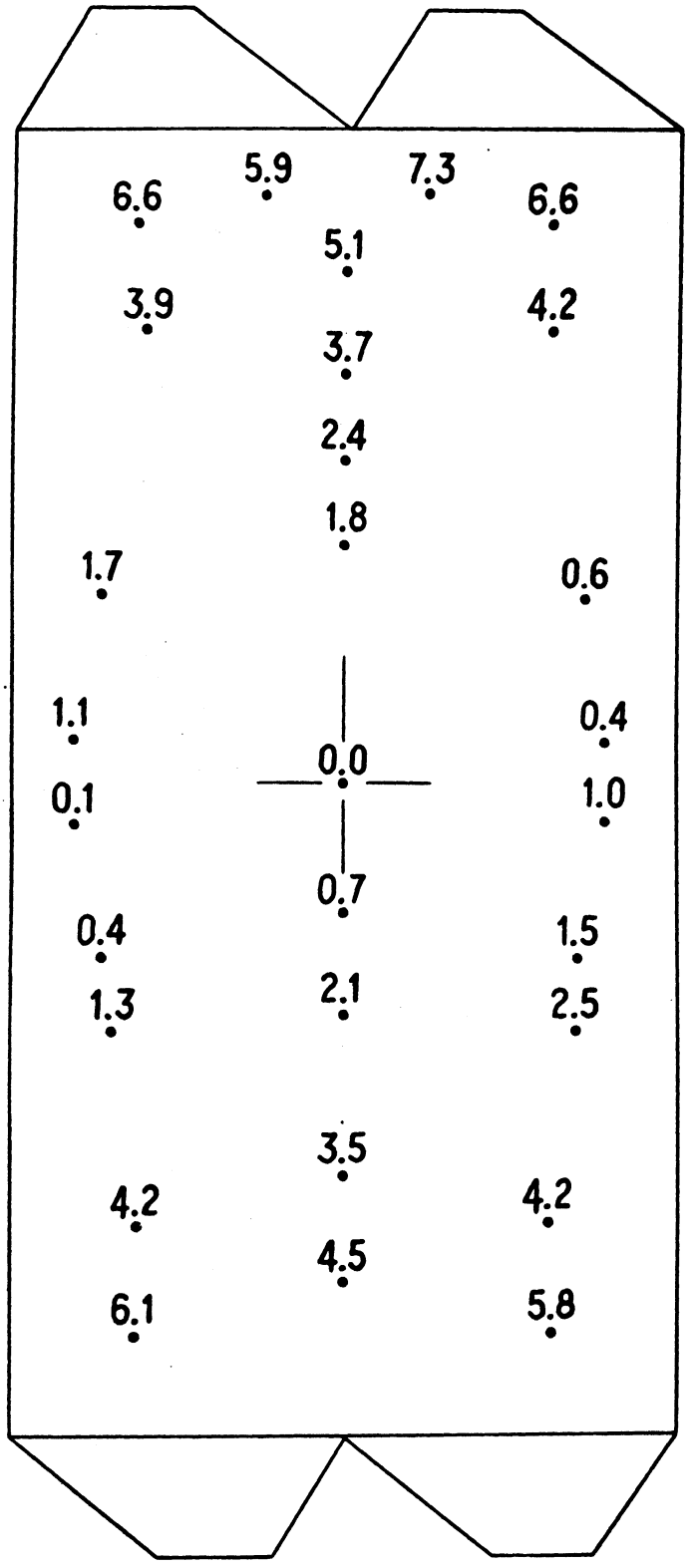

FIG. 7 DIAGRAM SHOWING THE RESPONSE OF HALF OF A CALORIMETER LAYER. NUMBERS REPRESENT ATTENUATION IN dB NECESSARY TO REDUCE LIGHT OUTPUT TO WHAT IT WOULD BE AT THE CENTER OF THE SCINTILLATOR.

The voltage signals from all eight phototubes in a calorimeter layer were passively summed to indicate the total amount of light observed in the whole layer of scintillator. The response of the top counter and layers 1, 2, and 10 was approximately the same no matter where a particle traversed the layer. Layer 10 was the least uniform of these counters and had a variation of less than 20 percent over the entire area. Much of this variation was in the proximity of the phototubes. This uniformity was not observed in layers 3 through 9. In these layers of NE102 scintillator the light was attenuated by its path length to the phototubes. A map of the response of half of a calorimeter layer was shown in Fig. 7. The numbers in the figure correspond to attenuation in dB and have associated systematic errors of $\pm$ 0.5 dB. This was the attenuation of the phototube output necessary in order to reduce the observed light from a single muon through that position so it was equivalent to the observed light from a single muon through the center. The ionization in the scintillator was calculated using the following equation to correct for the relative brightness of the observed light from various positons in the scintillator:

$$I_c = I_o (1. - 3.7013 \cdot 10^{-5} \cdot x^2) \quad .$$

In this equation I_o is the observed ionization at a position x cm from the center of the scintillator. The quantity I_c is the median ionization of single muons traversing the layer. The calibration procedure to determine I_c will be discussed in the next section.

The pulse height of the scintillator output at some (x,y) relative to the signal at the center of the layer, x = 0 , is indicated by the data points in Fig. 8. The inverse of the multiplicative correction factor applied to the observed ionization, I_o, is indicated by the solid line in that figure. The response of scintillator layers 3 through 9 was corrected in the energy determination of reconstructed events. The sum of the observed voltage signals from layers 1 through 9 was put through a discriminator and used to set an energy threshold for interesting events. There was no correction made for the scintillator response in the hadron trigger.

E. Electronics and Triggers

The electronics of the experiment consisted of two parts; a triggering system and an information recording system. Figure 9 is a block diagram of the trigger electronics and Fig. 10 shows the arrangement of electronics used in recording information about the events.

The two principle coincidence units which indicated that an interesting event had occurred are labeled in Fig. 9 as "MUONS CALIB." and"HADRON RUN." When the experimental apparatus was being triggered by hadron events, the output pulse from the "HADRON RUN" coincidence unit triggered the Marx generators and supplied a pulse to the information recording electronics via F4. The signal F4 was used as a gate pulse for the logarithmic analog to digital converters (LADC's) as well as a trigger for the camera control circuitry and recording logic. The "MUON CALIB." coincidence unit could be used to trigger the

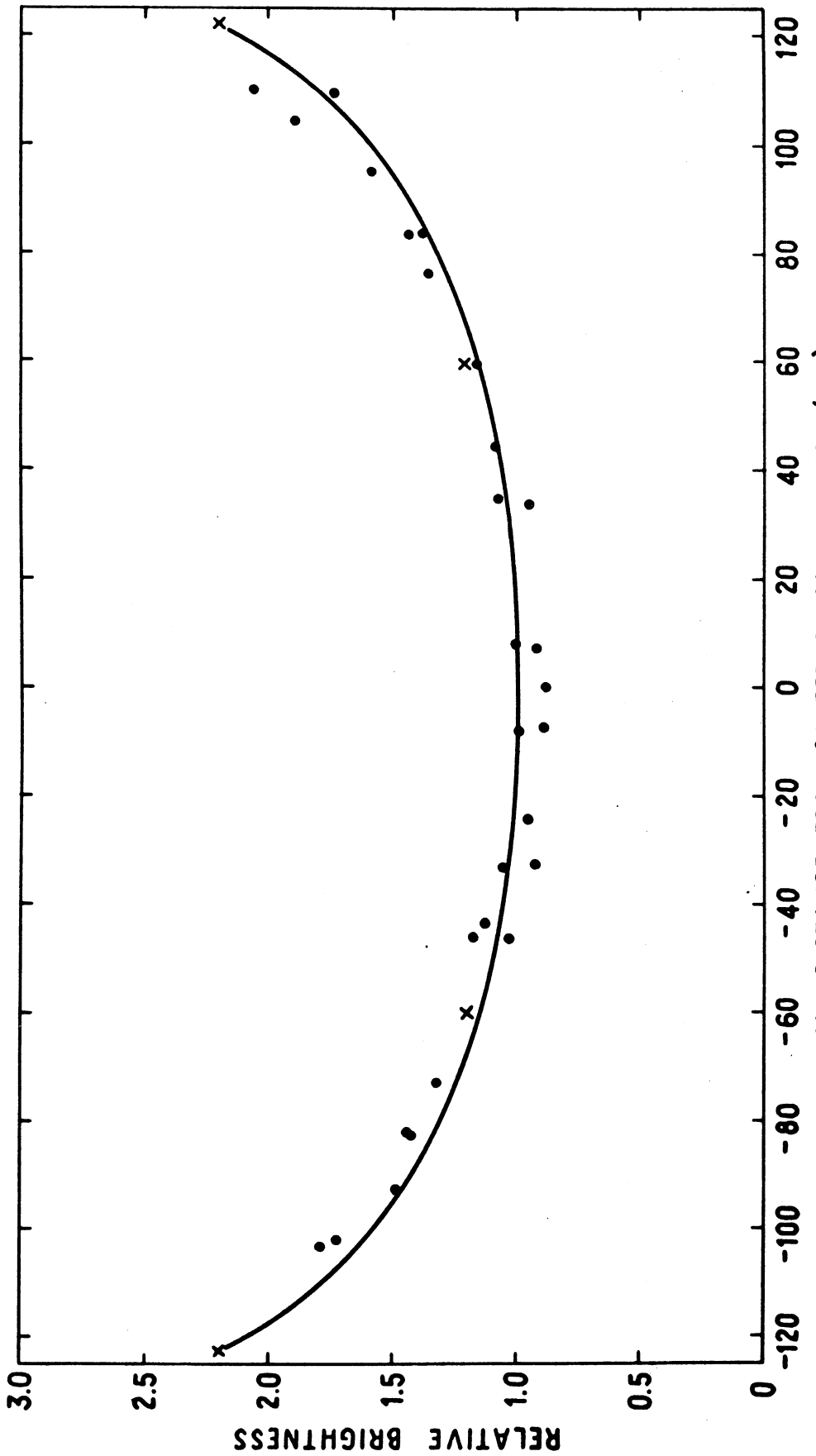

FIG. 8 OBSERVED RELATIVE BRIGHTNESS OF THE SCINTILLATOR RESPONSE AS A FUNCTION OF THE x-COORDINATE.

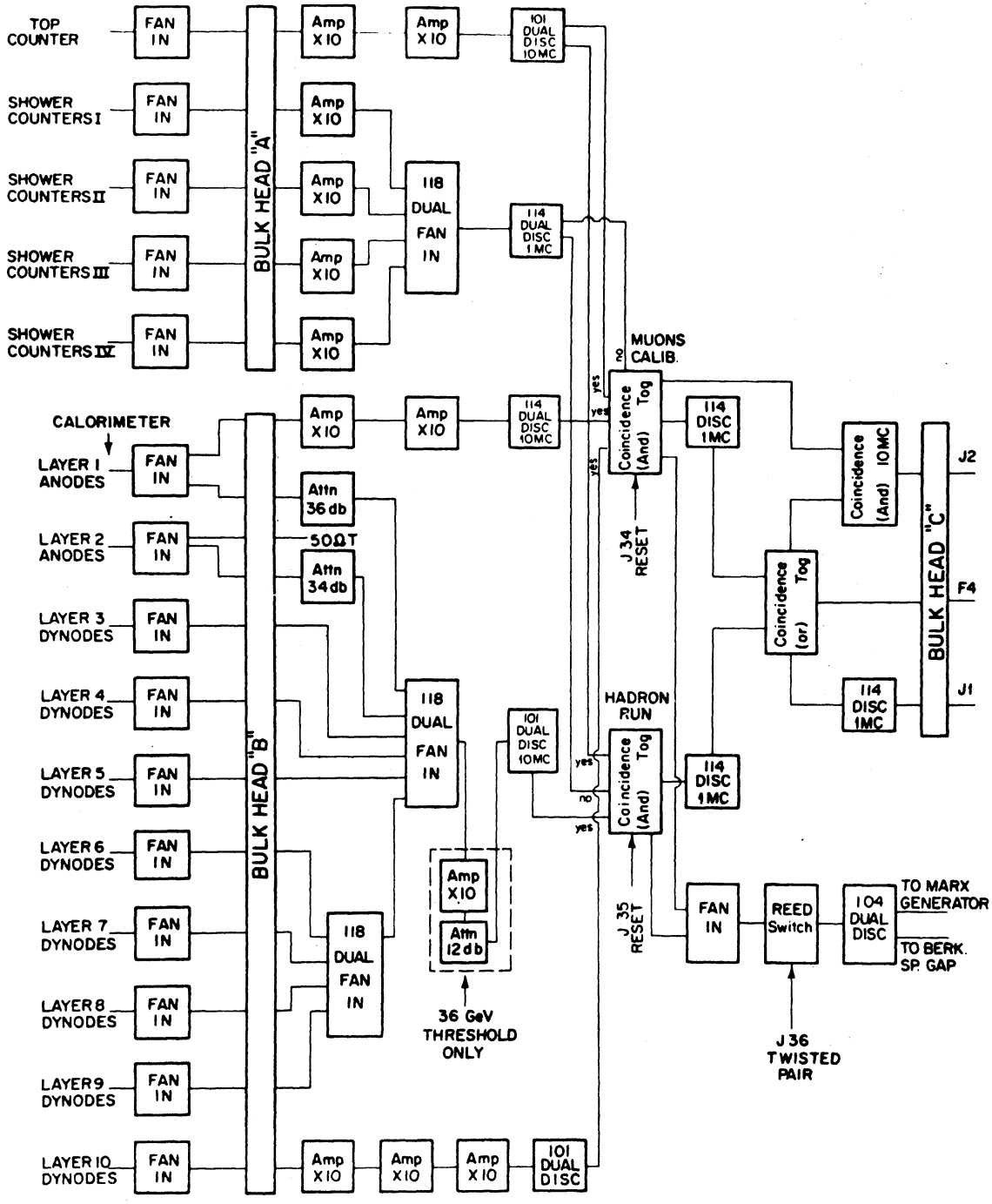

FIG. 9 BLOCK DIAGRAM OF THE TRIGGERING ELECTRONICS.

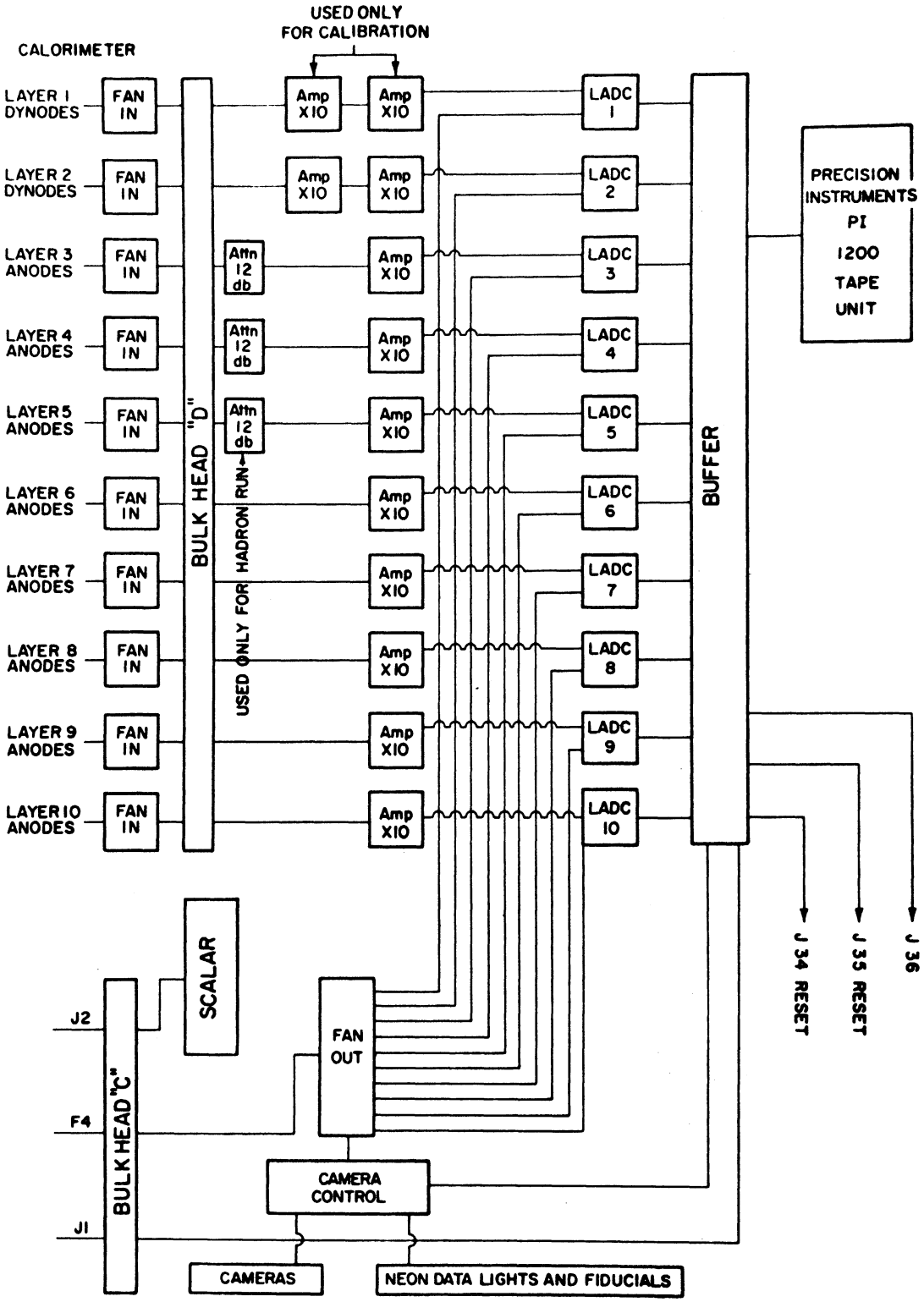

FIG. 10 BLOCK DIAGRAM OF ELECTRONICS USED TO RECORD INFORMATION ABOUT EVENTS.

same electronics. However, during a muon calibration the Marx generators were usually not triggered and pictures were not taken of the events. After the information about the hadron or muon event was recorded, the film advanced, and the Marx generators recharged, then the appropriate coincidence unit was reset by the buffer via J34 or J35. All the fast logic used in the trigger was Chronetics.

The inputs to the coincidence units consisted of signals from the top counter, a group of shower counters, layers 1 and 10 of the calorimeter, and a sum over layers 1 through 9. The top counter and the individual layers of the calorimeter have already been described. The shower counters were in four groups of six counters, each group along one side of the calorimeter. The signals from all the counters in a group were passively added, amplified, and summed with the output from the other groups. This signal was then used in anti-coincidence in both the muon and hadron triggers to reject events with accompanying shower particles. The summed signal from layers 1 through 9 of the calorimeter, using attenuators in the anode pulse of layers 1 and 2, was approximately proportional to the energy dissipated in the calorimeter. This summed signal was then used in the hadron coincidence to select events above a certain energy threshold. A summed voltage signal indicating ionization equivalent to that of 300 single muons corresponded to a 90 GeV event. Changing the energy threshold for hadron triggers was accomplished by amplifying the summed voltage. Because the response of calorimeter layers 3 through 9 depended on where the particles traversed the scintillator, using this summed signal did lead to trigger selection effects.

The coincidence criteria for a charged hadron were a signal from the top counter, no signal from the anti-shower array, and a summed calorimeter signal large enough to trigger a discriminator. This triggered the coincidence unit labeled "HADRON RUN." A simple variation of this triggering mode was used to measure the charged to neutral ratio of incident hadrons. In that case a hadron trigger was employed that required layer 2 of the calorimeter instead of the top counter. The charged to neutral ratio was used to calculate the pion to proton ratio in the incident flux so an appropriate correction could be made to the measured cross section to find the proton-proton cross section.

The muon trigger, using the coincidence unit labeled "MUON CALIB," was a threefold coincidence of the top counter, layer 1, and layer 10 of the calorimeter. It also had the shower counter array in anti-coincidence. This triggering mode was used mainly for muon calibration of the calorimeter, which is discussed in the next section.

The electronics shown in Fig. 10 were used to record information about events which triggered the system, either hadron or muon. The signal from each layer of the calorimeter was converted into a seven bit binary number by LeCroy 124L LADC's. An eighth bit indicated overflow of the LADC. This information was recorded on magnetic tape along with the event number, the run number, and other coded information. During the hadron runs, fiducials and event numbers were also recorded on film, along with the spark chamber photographs of each event.

F. Calibration Procedure

The median ionization of single muons observed in each layer was used as a reference to calibrate the calorimeter. The median muon pulse height was used to represent the average muon energy loss instead of the observed average pulse because of the distortion of the observed pulse height spectrum when two or more particles traversed a layer. This possibly introduced a small error into the measurement of the absolute energy, but the energy of each event relative to the others was not affected. The energy spectrum of the muons used to calibrate the calorimeter was dominated by muons with a range slightly greater than the calorimeter thickness, about 2 GeV. Deeper in the calorimeter the energy of the muons was less due to the ionization losses in the iron. The dE/dx of a 1 GeV muon in iron is 1.61 MeV/gm cm^{-2} and of 2 GeV muons is 1.72 MeV/ gm cm^{-2}. For the entire calorimeter the average ionization of a single muon was taken to be 1.7 MeV/gm cm^{-2}.

In order to detect and correct for systematic drifts in the photomultiplier tubes and the LADC's, a two step calibration procedure was repeated every seven to ten days. First, the LADC's were all calibrated with a pulser and a precision attenuator. Second, the median LADC measurement of the area under the gated voltage pulse of each layer was determined for single muons traversing the scintillator.

All of the LADC's were calibrated at the same time with a standard pulse fed through a variable attenuator. The pulse was attenuated in increments of 5 dB over a range of 0 to 80 dB. The LADC

measurements of eight pulses at each dB setting were recorded on magnetic tape. The useful range of the LADC's corresponded to an attenuation range of 60 to 70 dB, depending on the unit. This resulted in calibrated energy bins of approximately 0.5 dB per channel. The binary output of one of the LADC's vs. attenuation in dB is shown in Fig. 11. A straight line fits the curve quite well over most of the useful range.

The system was triggered by about 1500 muons to determine the median LADC measurement of the ionization of single muons. The summed voltage from each layer of the calorimeter was amplified and fed into the LADC's as indicated in Fig. 10. The binary output of the LADC's was recorded on magnetic tape for each of these events. The average ionization of amplified single muons was determined from the resultant distributions. The nonuniform response of layers 3 through 9 was studied to see how it affected the muon calibration. It caused a shift of, at most, one LADC channel, but because of the geometrical acceptance of the apparatus it was, on the average, much less.

The information recorded on magnetic tape from the LADC and muon calibrations was later used to convert the measured ionization of hadron events into a multiple of the average muon ionization. A curve similar to the one illustrated in Fig. 11 was determined in the calibration procedure for each LADC. The ordinate scale of dB corresponds to the amount of attenuation of the standard pulse by the precision attenuator. Little or no attenuation corresponds to the

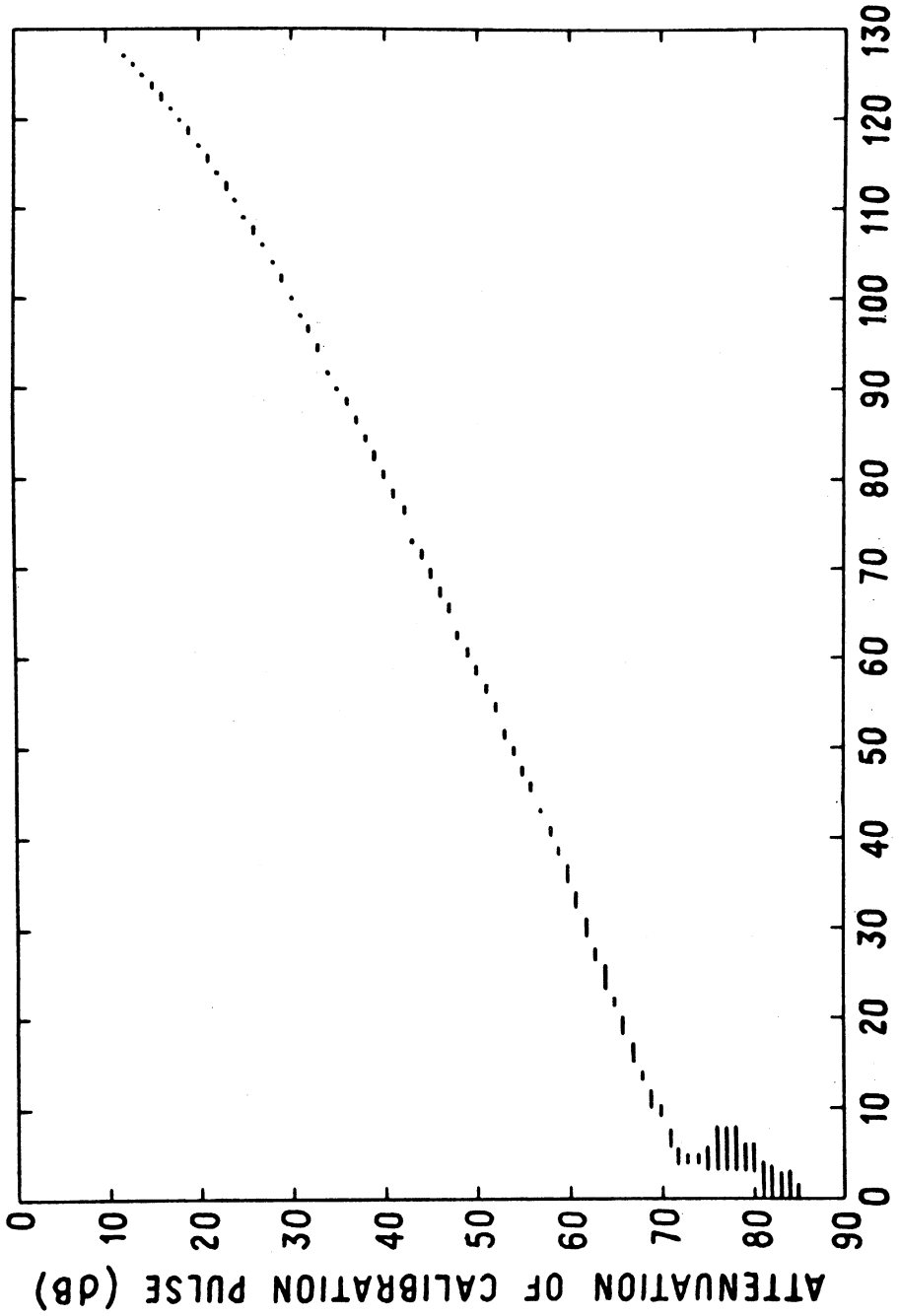

FIG. 11 RESPONSE OF A LOGARITHMIC ANALOG TO DIGITAL CONVERTER.

largest binary output available from the LADC, 177_8. In the following discussion, V_R is the standard pulse attenuated by some amount so that it would have an LADC binary output of 177_8 on the linear fit. The voltage signal from an individual layer, V_i, was measured by an LADC that was calibrated in terms of dB_i.

$$dB_i = 20 \log_{10} V_i/V_R \quad .$$

When the system was triggered by muons, the voltage from each calorimeter layer was amplified as indicated in Fig. 11 before it was received by the LADC. Hence, the LADC record of the muon events corresponds to an amplified muon pulse, V_μ. The following equation related this voltage to the unamplified muon pulse, V_1.

$$20 \log_{10} \frac{V_1}{V_R} = 20 \log_{10} \frac{V_1}{V_\mu} + 20 \log_{10} \frac{V_\mu}{V_R} \quad .$$

The calibration procedure determined the average muon response of the LADC in terms of attenuation of the precision attenuator. This is represented in the above equation by $20 \log_{10}(V_\mu/V_R)$. The other term on the right-hand side in that equation represents the additional attenuation of the precision attenuator necessary to correct for the amplification of the muon signal. The quantity determined was the voltage pulse of a single unamplified muon in terms of attenuation of the reference voltage pulse.

For each layer of the calorimeter the voltage received by the LADC was converted into a multiple of the voltage pulse of a single unamplified muon. In order to ensure that the number of "equivalent muons" was a simple multiple of the average ionization of single muons both the gain and the linear range of the phototubes was checked. The gains of the eight phototubes used in a layer were matched so that their useful range would be comparable. The linear range of the EMI 9816B phototubes was tested using a pulsed light source. These tests showed that the response of the phototubes was linear up to an anode current of 60 mA. The phototubes were operated such that they were within the linear range even when the ionization observed by a single phototube caused the LADC to overflow. With this operational range the summed voltage output from a calorimeter layer was proportional to the observed ionization. The following equation relates the ratio of voltage received by the LADC to the reference voltage of the LADC calibration.

$$\frac{V_h}{V_1} = \frac{V_h}{V_R} \cdot \frac{V_R}{V_1} \quad .$$

V_h represents the voltage received at the LADC when the system was triggered on hadrons. Rewritten in terms of the LADC output, calibrated with respect to the precision attenuator, this equation is

$$20 \log_{10} \frac{V_h}{V_1} = 20 \log_{10} \frac{V_h}{V_R} - 20 \log_{10} \frac{V_1}{V_R} \quad .$$

The term $20 \log_{10}(V_1/V_R)$ was determined by the LADC and muon calibration. The other term on the right-hand side represents the binary output of the LADC calibrated in terms of attenuation of the reference pulse. This equation uniquely determines the equivalent number of muons in a layer as a ratio of the measured hadron and muon ionization. Since 6.02 dB corresponds to a factor of 2 in a ratio of voltages, the equivalent number of muons is 2^T. T is the number of factors of 2 in the ratio of voltages.

$$T = | 20 \log_{10}(V_h/V_1)/6.02| \quad .$$

CHAPTER III. DATA ANALYSIS

The experimental data for a hydrogen inelastic cross section were accumulated between October, 1968 and May, 1969. During that time, 116,000 hadrons triggered the apparatus. Two 90 degree stereo photographs of the spark chamber system were taken for each event. An example of these pictures has been presented in Figs. 4 and 5. The calorimeter data for each event was recorded on magnetic tape along with the information from the muon and the LADC calibrations. In the subsequent sections the analysis of these data will be described. These include scanning and measuring of the film, reconstructing events, and assigning an energy to the events. Justification will also be furnished for the selection and interpretation of events used in calculating cross sections.

A. Scanning and Measuring

The purpose of scanning the film was to select from the total sample of triggers the single incident hadrons that interacted in the hydrogen and those that traversed the target without evidence of interaction. The stereo photographs of every hadron-like trigger were scanned side by side and the events sorted into three categories. The first consisted of all events that interacted in the hydrogen or target vessel and displayed more than one charged track in the lower wide gap spark chamber. Events with two charged tracks (prongs) were given special consideration in order to distinguish between an event with two charged hadron secondaries and an event with one charged hadron

accompanied by a δ-ray. The second category consisted of events with only one observed track entering and leaving the hydrogen target. Events were placed in one of these two groups if there was no evidence that more than one incident particle could have deposited energy in the calorimeter. The third category included all triggers that were rejected from the other two. It included triggers that resulted in no measurable tracks, as well as triggers where a track developed in only one of the wide gap spark chambers. In general, the multiple prong events corresponded to inelastic interactions, and single prong events corresponded to incident hadrons that did not inelastically interact in the target. However, there are three important exceptions: inelastic collisions where all the charged secondaries had a maximum opening angle less than 3 mr, inelastic collisions producing only neutral pions, and non-interacting events that were accompanied by a δ-ray. The number of inelastic collisions that were scanned as one-prong events was evaluated by a Monte Carlo program and will be discussed in Section E of this chapter. The non-interacting events accompanied by a δ-ray were distinguished from two and three prong inelastic collisions at the scanning table.

Most two-prong events consisted of a single hadron accompanied by a δ-ray. These δ-rays were knock-on electrons produced by collisions of the incident hadrons with orbital electrons in the target material. The δ-rays were identified by the following scanning criteria which are later justified in Section E of this chapter. The track that was most colinear with the incident particle was assumed to be the ongoing hadron. The other track or tracks were either produced secondary hadrons or δ-rays. A track with kinks resulting from scattering in the spark

chamber fail or gas was considered a δ-ray. Thus if one track of a two-prong event was not straight or if it showed no signs of producing ionization in the iron plate spark chambers, the event was grouped with the one-prong events. For the remaining two- and three-prong events the range in the iron plate spark chamber of the secondaries of δ-rays observed. If more than one charged prong produced a track in these spark chambers after the third gap, it was grouped with the multiple-prong events.

In the following discussions concerning single and multiple-prong events they will also be referred to as non-interacting and interacting events respectively. The observed interactions account for all but 4 to 5 percent of the true inelastic interactions. Also, less than 1 percent of the events that were grouped with the one-prong or non-interacting events were inelastic collisions. Events in both of these groups were measured and reconstructed. Points along the observed tracks in the upper and lower wide gap spark chambers were measured on the film along with fiducial marks. These measurements from the two stereo photographs were used to compute or "reconstruct" the trajectory of the particle in real space.

Events in the group of non-interacting hadrons were measured on a flying spot digitizer on line to a DDP-124 computer. This system, called the Michigan Automatic Scanning System, MASS, has a resolution of 10 μ on the film. When a dark track was observed by the scanner, the left- and right-hand edges were measured three times and the average interpolated to a point between the least count locations of the cathode ray tube. The scanner was programmed to measure tracks from 10 to 230 μ wide, whereas the approximate width of good tracks was, on the average,

40 μ. In order to measure tracks with reasonable accuracy, the MASS system measured 13 points in each gap of the wide gap spark chambers. In both views, the measurements along the tracks, the event number, and the measured position of four fiducials were recorded on magnetic tape.

Interacting events were measured at the University of Wisconsin on a Nuclear Research Instruments microscope. Eight points were measured in each gap along each visible track. The measurement information was recorded on magnetic tape via a CDC-924 computer. This film plane digitizer had a least count of 1 μ and was also used to measure photographs of a fiducial grid used in the optics study discussed in the next section.

B. Optics and Reconstruction

In order to achieve good resolution, necessary optical corrections were studied in detail. A sheet of 0.25 inch thick lucite with 32 fiducial marks was mounted and photographed in front of each wide gap spark chamber. The photographs of these fiducials, along with 8 fiducials on the glass of the spark chamber, were measured on the 1 μ resolution microscope. A Chi-squared (χ^2) fit was performed with these measurements to determine coefficients of a second-order polynomial correction function. The functions which corrected for distortions in the film plane were assumed to be

$$y(y_m,z_m) = y_m + F_2 z_m + F_3 y_m^2 + F_4 y_m z_m + F_5 z_m^2 \quad ,$$

$$z(y_m,z_m) = G_1 y_m + G_2 z_m + G_3 y_m^2 + G_4 y_m z_m + G_5 z_m^2 \quad .$$

The vertical coordinate on the film is indicated by z and the horizontal coordinate by y. The functions $y(y_m,z_m)$ and $z(y_m,z_m)$ determine an optics corrected position in the film plane of the measured points y_m and z_m. There were four sets of correction functions determined, one set for each spark chamber in the two orthogonal views. The χ^2 function formed to determine the four sets of F's and G's was

$$\chi^2 = \sum_{i=1}^{40} \left\{ \left[\frac{y_i' - y(y_m,z_m)}{\sigma_{iy}} \right]^2 + \left[\frac{z_i' - z(y_m,z_m)}{\sigma_{iz}} \right]^2 \right\} .$$

The summation covered all the measured fiducials of a spark chamber and the fiducial plate in front of it. The terms y_i' and z_i' were the assigned coordinates of the ith fiducial. The terms σ_{iy} and σ_{iz} consisted of errors in specifying y_i' and z_i' as well as measuring errors in y_m and z_m. The minimization of χ^2 was done by a University of Wisconsin library subroutine, GAUSHAUS. It provides a least squares estimate of the parameters using an iterative technique in which the estimates at each interation were obtained by a method which combines the Taylor series method and the method of steepest descent.

Correction of the measured points by the analytic functions $y(y_m,z_m)$ and $z(y_m,z_m)$ did not remove all of the observed optical distortions. A further non-analytic correction was made to the corrected position of the measured points. This correction was inferred by interpolating between displacements of local points of the fiducial grid.

Optical differences between the MASS measuring machine and the microscope were also corrected by use of a fiducial grid. A transformation, based on measurements of this grid by the two measuring machines, then changed MASS measured points into microscope measured points. The transformation had the form

$$y_{Mic} = A_1 + A_2 y_M + A_3 z_M + A_4 y_M^2 + A_5 y_M z_m + A_6 z_M^2 \quad ,$$

$$z_{Mic} = B_1 + B_2 y_M + B_3 z_M + B_4 y_M^2 + B_5 y_M z_M + B_6 z_M^2 \quad .$$

The subscripts M and Mic refer to MASS measured points and the corrected equivalent microscope measured points, respectively. The χ^2 fit to determine the parameters A and B was similar to the fit just described.

The measured points of all events, once in the microscope coordinates, were rotated, translated, and applied a differential magnification so as to properly orient them with respect to the optical axis. This transformation had the form

$$y_m = C_o + C_1 y_{Mic} + C_2 z_{Mic} \quad ,$$

$$z_m = (C_3 - C_2 z_{Mic} + C_1 y_{Mic})/C_4 \quad .$$

The quantities y_m and z_m represent the measured points which were corrected in the film plane for optical distortions. The corrected position of a measured point on the film defined a ray through an ideal optical system back into the spark chambers. The coordinate system into which rays were projected is shown in Fig. 12. This is the real space coordinate system used to describe the experiment and reconstructed

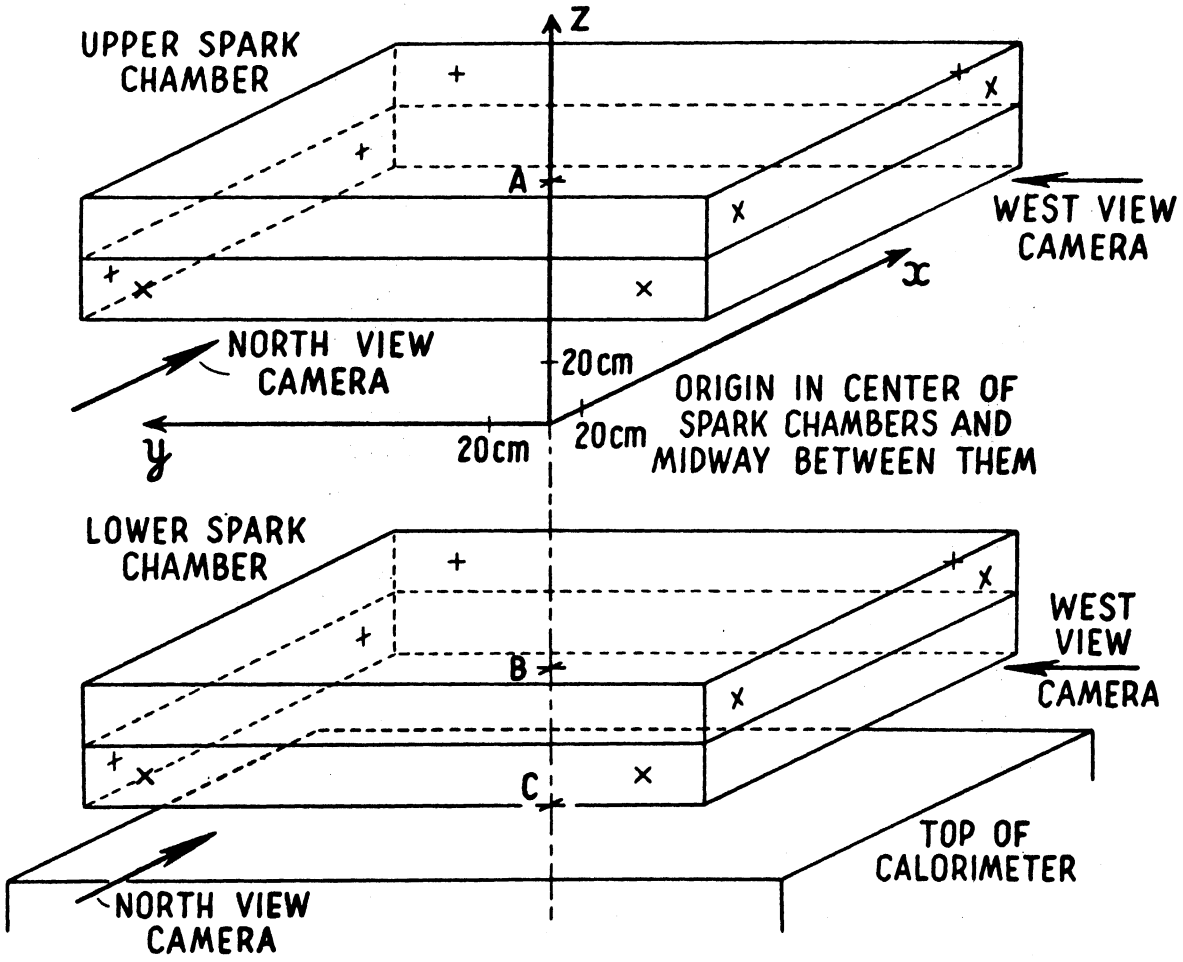

FIG. 12 DIAGRAM OF THE COORDINATE SYSTEM USED TO DESCRIBE THE EXPERIMENT. A AND B INDICATE THE CENTERS OF THE UPPER AND LOWER WIDE GAP SPARK CHAMBERS. POSITION C IS THE CENTER OF THE TOP OF THE CALORIMETER.

events. The origin is midway between the centers of the spark chambers. This point was within 1 cm of the center of hydrogen target.

The parameters describing the hadron trajectory were defined in the real space coordinate system shown in Fig. 12. A point on the trajectory along with a set of direction cosines completely defined the path of a particle. If only one spark was measured in a spark chamber, five independent parameters were used to characterize the event. These parameters are labeled in Fig. 13, as α, β, x_o, y_o, and δ. The α and β are direction cosines, x_o and y_o are coordinates in the plane $z = 0$, and δ is a drift parameter of the measured track in the z-direction. The electrons, produced in ionization caused by the charged hadron, drift toward the center foil of the spark chamber as the spark is developing. For reconstruction purposes this vertical drift was projected into the x, y plane to correct for the observed shift of the sparks in the upper and lower gaps of a spark chamber. The third direction cosine of the real space track is not an independent parameter, but is determined by α and β. These parameters are illustrated in Fig. 13.

The parameters characterizing a track were determined by the use of an analytic expression for the distance between two skew lines in space. One of these lines represented the trajectory of the hadron, and the other a ray projected from a measured point on the film through an optical system into the spark chamber. The χ^2 function which was minimized to determine the parameters of the trajectory was

$$\chi^2 = \sum_i \frac{d_i d_i}{\sigma^2} \quad ,$$

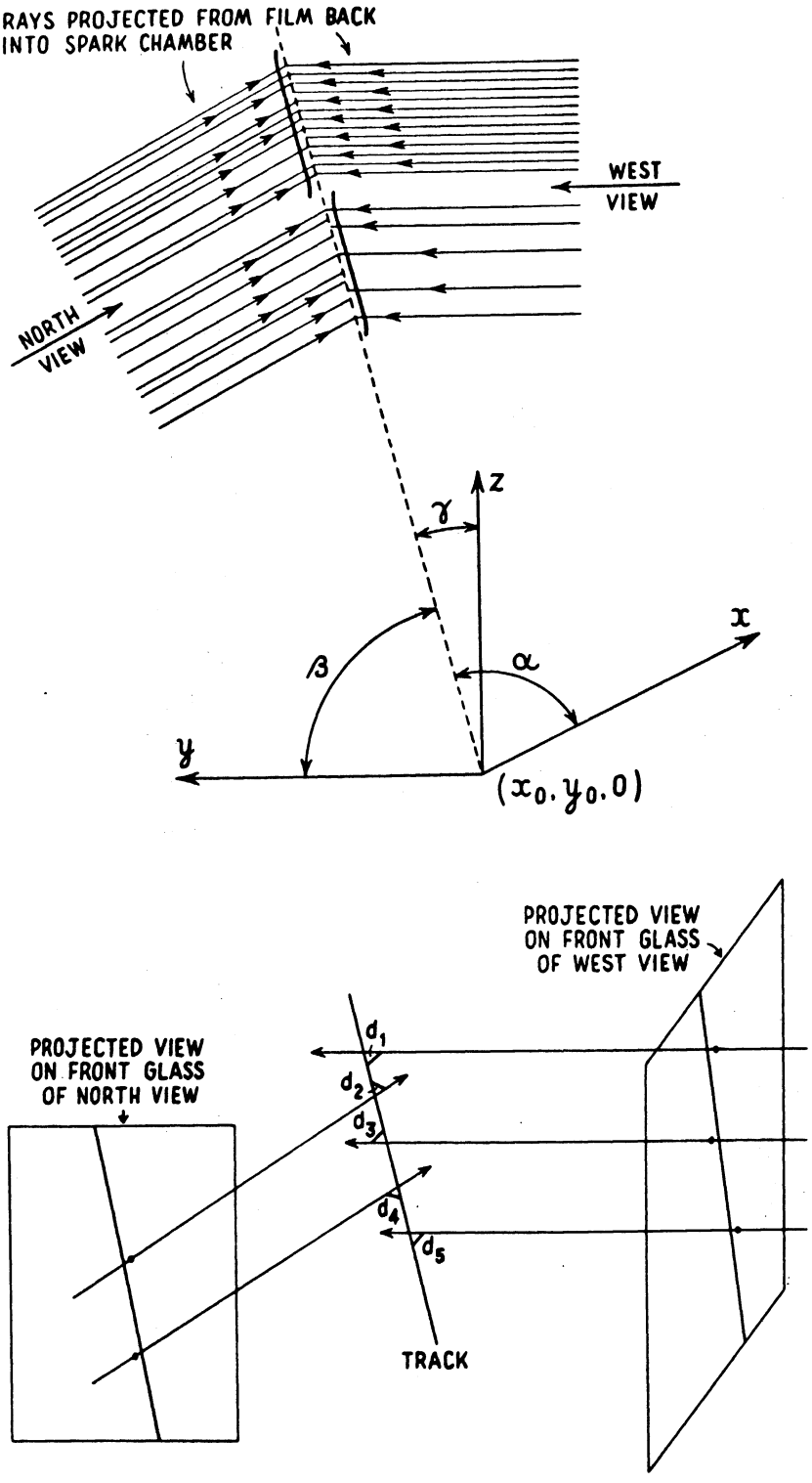

FIG. 13 DIAGRAM SHOWING SOME OF THE RECONSTRUCTION PARAMETERS. THE POINT $(x_o, y_o, 0)$ IS WHERE THE INCIDENT TRACT CROSSES THE MIDPLANE OF THE HYDROGEN TARGET.

$$d_i = [(x' - x_i)(\beta\gamma_i - \gamma\beta_i) + (y' - y_i)(\gamma\alpha_i - \alpha\gamma_i) + (z' - z_i)$$

$$\cdot (\alpha\beta_i - \beta\alpha_i)]/\sin\theta_i \quad ;$$

$$\cos\theta_i = \alpha\alpha_i + \beta\beta_i + \gamma\gamma_i \quad ; \quad \gamma = -\sqrt{1 - \alpha^2 + \beta^2} \quad ;$$

$$x' = x \pm \frac{\delta\alpha}{\sqrt{\alpha^2 + \beta^2}} \quad ; \quad y' = y \pm \frac{\delta\beta}{\sqrt{\alpha^2 + \beta^2}} \quad .$$

The quantity d_i, is the perpendicular distance between two skew lines. The subscript i, refers to the projected ray from the ith measurement on the film of a track. If there was one track in the spark chamber and the event was measured on MASS, then the summation covered a possible 52 measurements. Some of the projected rays from measurements of both views are illustrated in Fig. 13 along with the fit trajectory.

The secondaries of an interacting event were fit in each view of the lower spark chamber separately. No correlation was attempted between secondaries produced in the target and seen in the two views of the lower spark chamber. A projected trajectory of a secondary was fit from rays of measured points projected into the spark chamber. The secondaries were fit in a plane containing the incident hadron and the x- or y-axis in the west or north view, respectively.

The interaction vertex was found using the information from both projected views simultaneously. The point of interaction was determined by minimizing the square of the distance between a point x_I, y_I, z_I and all the fit tracks in the upper and lower spark chambers. The resolution

of the system for reconstructing interactions in this manner was ± 1.0 cm in z and ± 0.2 cm in x and y. This resolution was important in order to separate interactions that occurred in the target walls from those occurring in the liuqid hydrogen.

The angle between the charged tracks of a non-interacting event that were observed in the upper and lower wide gap spark chambers was, on the average, 3 mr. This result was based on the independent reconstruction of tracks in the two spark chambers. The angle between the two trajectories, ϕ, was defined by the equation

$$\phi = \text{Arc cos } (\alpha_u \alpha_L + \beta_u \beta_L + \gamma_u \gamma_L)$$

The subscripts u and L on the direction cosines refer to the upper and lower spark chamber fits respectively. Figure 14 shows the shape of the distribution of the logarithm of the number of events as a function of the scattering angle squared. This distribution is the result of measuring errors and is so broad that elastic scattering results could not be obtained. The average elastic scattering angle is expected to be 2 mr at 100 GeV and decreases with increasing energy.

C. Energy Determination

Since calorimeters were first suggested by Grigorov, Murzin, and Rapoport [23], they have been studied as a means of energy estimation of energetic hadrons. During the summer and fall of 1966 an experimental calorimeter was operated at the University of Denver High Altitude Laboratory. The analysis of that calorimeter by D. Lyon and A. Subramanian [24] led to the design of the calorimeter used in this experiment. Details of the construction have been discussed in a

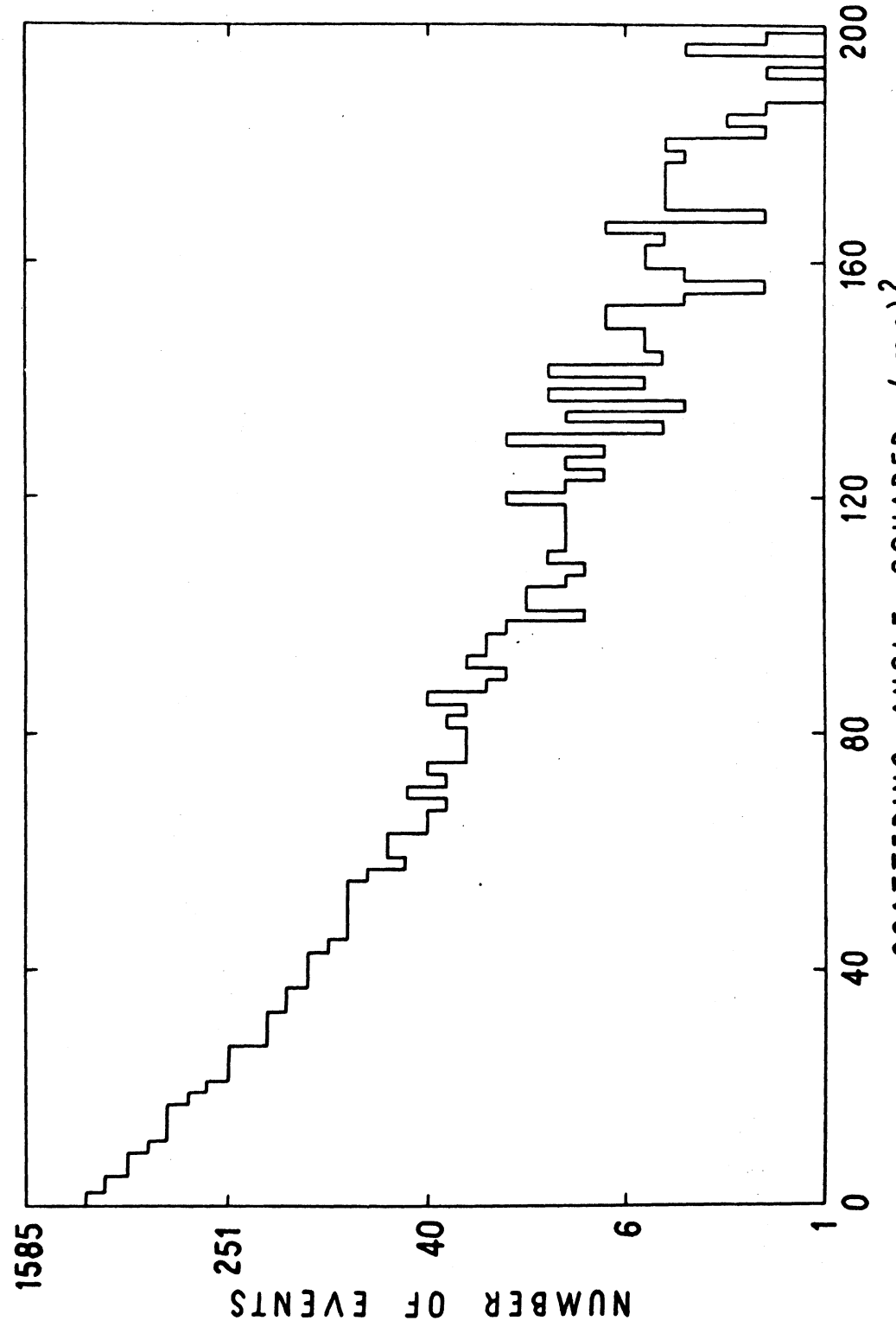

FIG. 14 DISTRIBUTION OF THE SQUARE OF THE SCATTERING ANGLE OF NON-INTERACTING EVENTS.

previous section.

Hadrons traversing material such as iron, dissipate their energy in electromagnetic and strong interactions [22]. A cosmic ray hadron incident upon the calorimeter initiates a cascade of hadrons. When a neutral pion is produced at an interaction site of the cascade, it decays into γ-rays which begin an electromagnetic shower. An important step in the energy dissipation, both of the charged hadrons and the superimposed electromagnetic cascade, is ionization of the traversed medium. The energy of the incident particle is the sum of the energy which is observed as light from ionization produced in the scintillator, plus a correction for the energy which cannot be detected.

$$E = \int \int \beta N(\beta,t)\, d\beta\, dt + v(E) \quad .$$

The function $N(\beta,t)$, is the number of particles with specific ionization β, at a depth t, in the iron. The integral represents the energy in the form of measureable ionization. The term $v(E)$, is the mean energy dissipated in the calorimeter which is not detected. The three principal contributions to the term $v(E)$, are the nonlinearity of the probes in measuring ionization, energy leaving the calorimeter's volume, and nuclear binding energy supplied to the disintegrated iron nuclei at an interaction site.

The calorimeter was used to determine the energy of the incident hadron on the basis of ionization sampled in ten layers of plastic scintillator. The ionization energy represented by the integral in the last equation was approximated by the following sum

$$E_I = \beta_c \left\{ \frac{N_B f_B w_B}{2} + \sum_{i=B+1}^{L} \frac{(N_{i-1} f_{i-1} + N_i f_i) w_i}{2} + C(L) \right\}.$$

The coefficient β_c, represents the energy lost by a typical muon which would satisfy the muon coincidence requirements. The energy spectrum and typical ionization energy dissipated by the muons used in the calibration procedure was discussed in Chapter II, Section E. It was concluded in that section that the calibrated signal from a single muon represented an ionization energy, β_c, of 1.7 MeV/gm cm^{-2}. Each N_i is the ionization observed in the ith layer divided by the calibrated single muon ionization in that layer. These equivalent numbers of muons N_i, were corrected for the nonlinear response of the scintillator. Each N_i was multiplied by a correction factor f_i, in order to account for the fact that the electromagnetic shower in the calorimeter was sampled by scintillator, not iron. Due to the difference in critical energy of iron and scintillator, the low energy electrons entering the scintillator from the iron were attenuated by ionization more rapidly than they were regenerated by pair production. This resulted in an underestimate of the ionization energy loss in the iron. The correction f_i, referred to below as the transition effect correction, is discussed further in Appendix A. It is based on the work of Crannell et al. [25] and depends on the thickness of the scintillator. For layers 1, 2, and 10 the equivalent numbers of muons observed was corrected upwards by a factor of 1.05, whereas for layers 3 through 9 the correction was 1.11. The weight factors, w_i, are the thickess of iron between layers i - 1 and i in gm/cm^2. The first layer included in the energy calculation, i = B, is the first

layer with greater than five equivalent muons. If the incident hadron interacted in the target the weight factor $w_1 = 45$ gm/cm^2, included 5 gm/cm^2 for the material of the target and spark chamber which absorbed some energy before the event entered the calorimeter. If the incident hadron apparently had its first interaction in the calorimeter, w_B was the material traversed between layer B and the average position of the first interaction in the iron between layers B - 1 and B. The average position of the first interaction was determined from the formula

$$z_{av} = \int_{z_{B-1}}^{z_B} t \, \frac{e^{-t/\lambda}}{\lambda} \, dt \quad .$$

The measurement of λ is discussed in Ch. IV, Sec. B. Finally, the sum terminates at L, the last layer of the calorimeter traversed by the extrapolated trajectory of the incident hadron. Beyond L the energy is approximated by the term C(L). For average shower development at large enough depths into the calorimeter, exponential absorption of the cascade prevails and the area under the shower curve is approximated by the integral C(L).

$$C(L) = \int_{z_L}^{\infty} N_L f_L \, e^{-z/\Lambda} \, dz = \Lambda \, N_L f_L \quad .$$

$\Lambda = 240$ gm/cm^2 was determined from Fig. 32 and is correct for the average shower of 300 GeV incident hadrons. The contribution of this integral to the energy of individual events was occasionally large and depends on the depth of the first interaction. The average increase

in energy of events due to the term C(L) was 2 to 3 percent.

The calibrated equivalent number of muons in the sampling layers of the calorimeter are illustrated in Figs. 15 through 17 for a random selection of events in three energy bins. The energies of the events shown in these figures were calculated by a formula which will be discussed below. When the number of equivalent muons N_i, in each layer i, is corrected by the factor f_i for that layer, then the area under the line connecting the points is proportional to the observed ionization energy E_I, without the correction C(L). The higher energy events, which have a superposition of ionization from more particles in their nuclear-electromagnetic cascade, display smaller layer by layer fluctuations of the observed ionization. Since the fluctuations are large there was no correction made for the presence of the center rib in the calorimeter. Monte Carlo simulation of cascades in a calorimeter by J. Ranft [26] and W. V. Jones [1] indicate that most of the cascade is contained within a radius of 10 cm around the extrapolated incident track. R. Hofstadter [27] suggests that the lateral spread of the cascade is larger than this due to neutrons produced in the cascade. If the event traversed the center rib, the fraction of ionization not being sampled by scintillator was less than fluctuations in the observed ionization. The calculation of ionization energy for the events, E_I, also made no correction for the zenith angle of the incident particle. An event with a zenith angle, θ, traversed a path length in each iron layer of $w_i \sec\theta$ rather than the normal path length w_i, and the ionizing particles traversed a correspondingly longer path length.

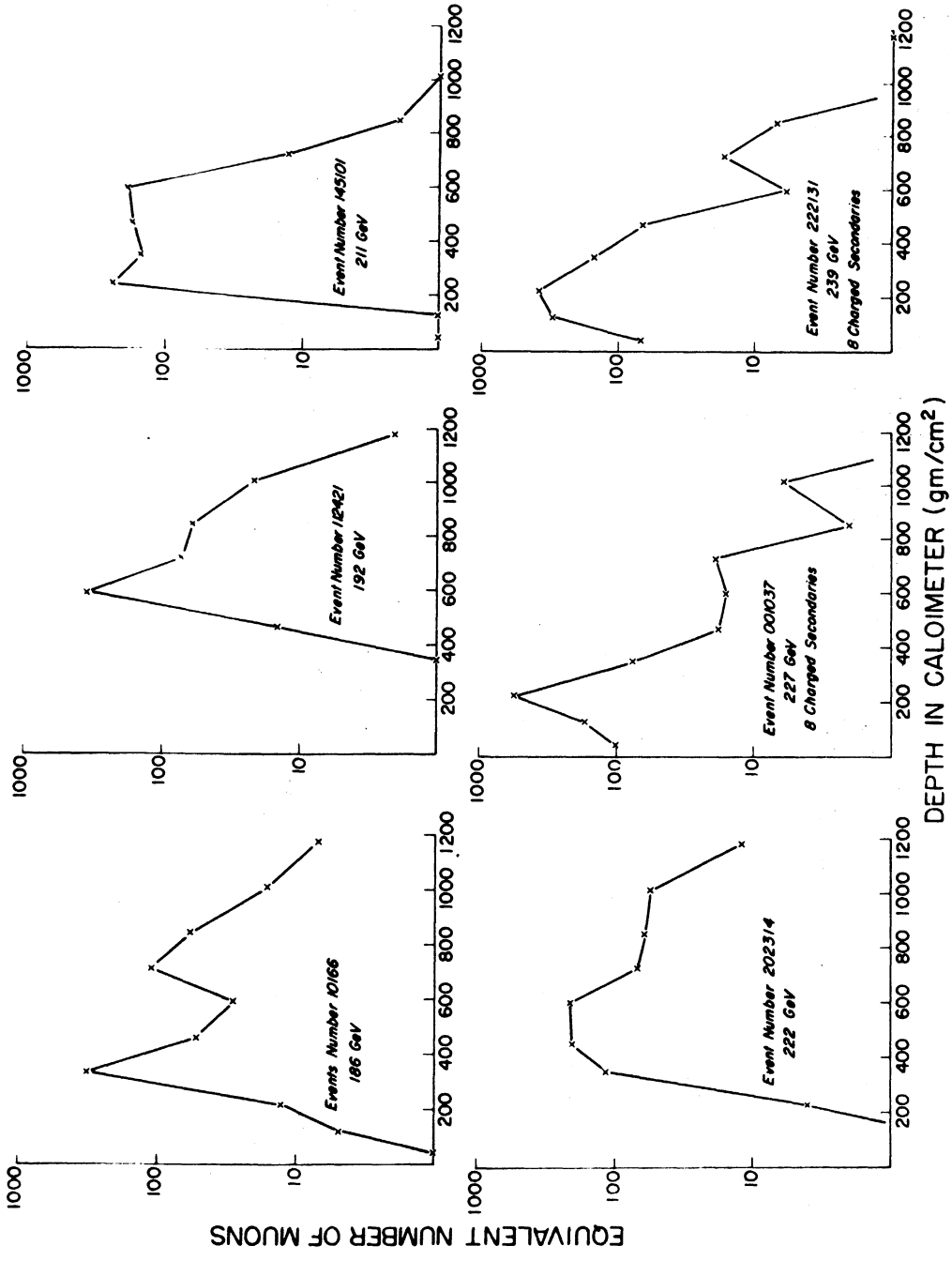

FIG. 15 INDIVIDUAL EVENT IONIZATION CURVES. ENERGY ABOUT 200 GeV.

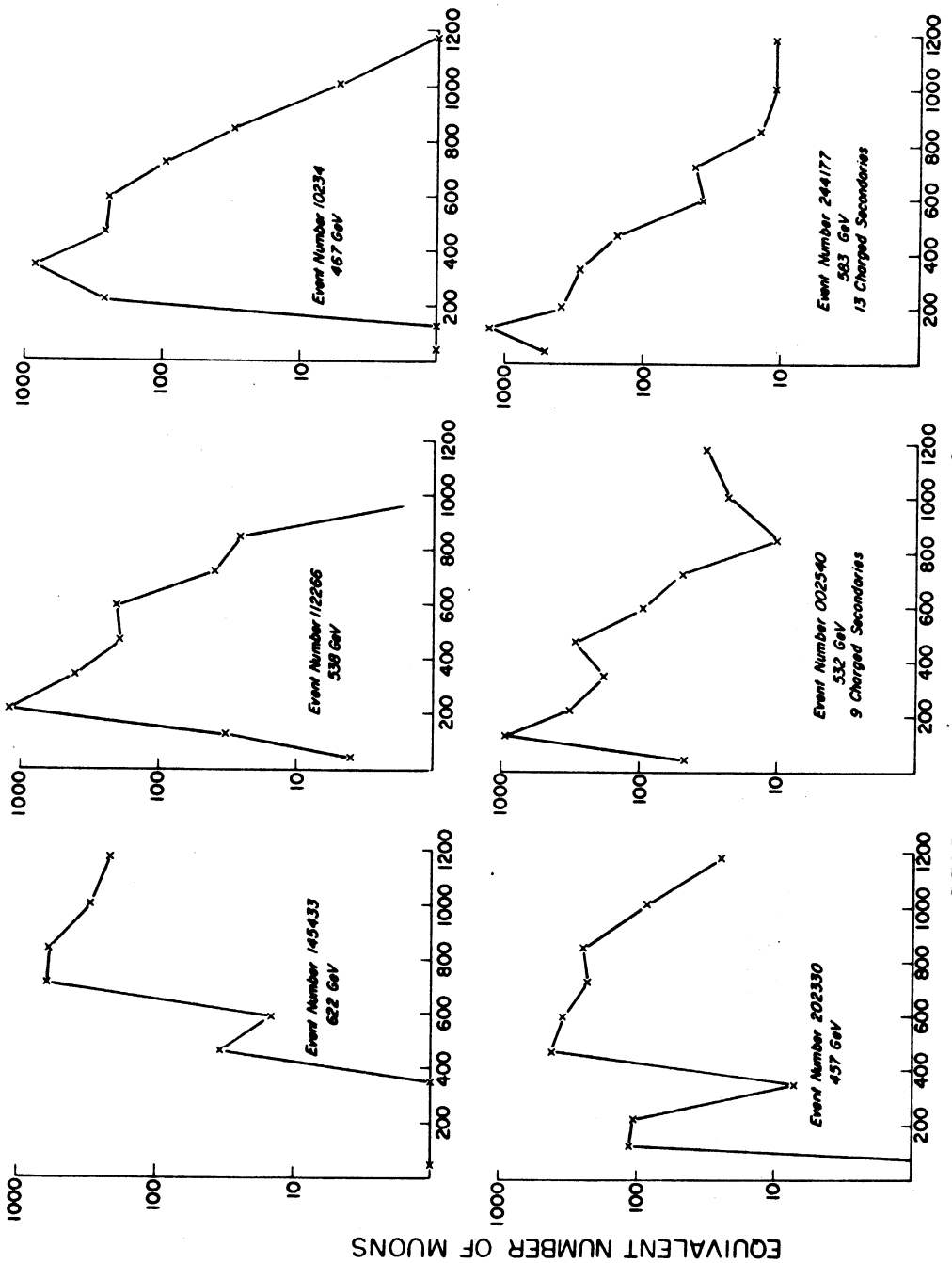

FIG. 16 INDIVIDUAL EVENT IONIZATION CURVES. ENERGY ABOUT 500 GeV.

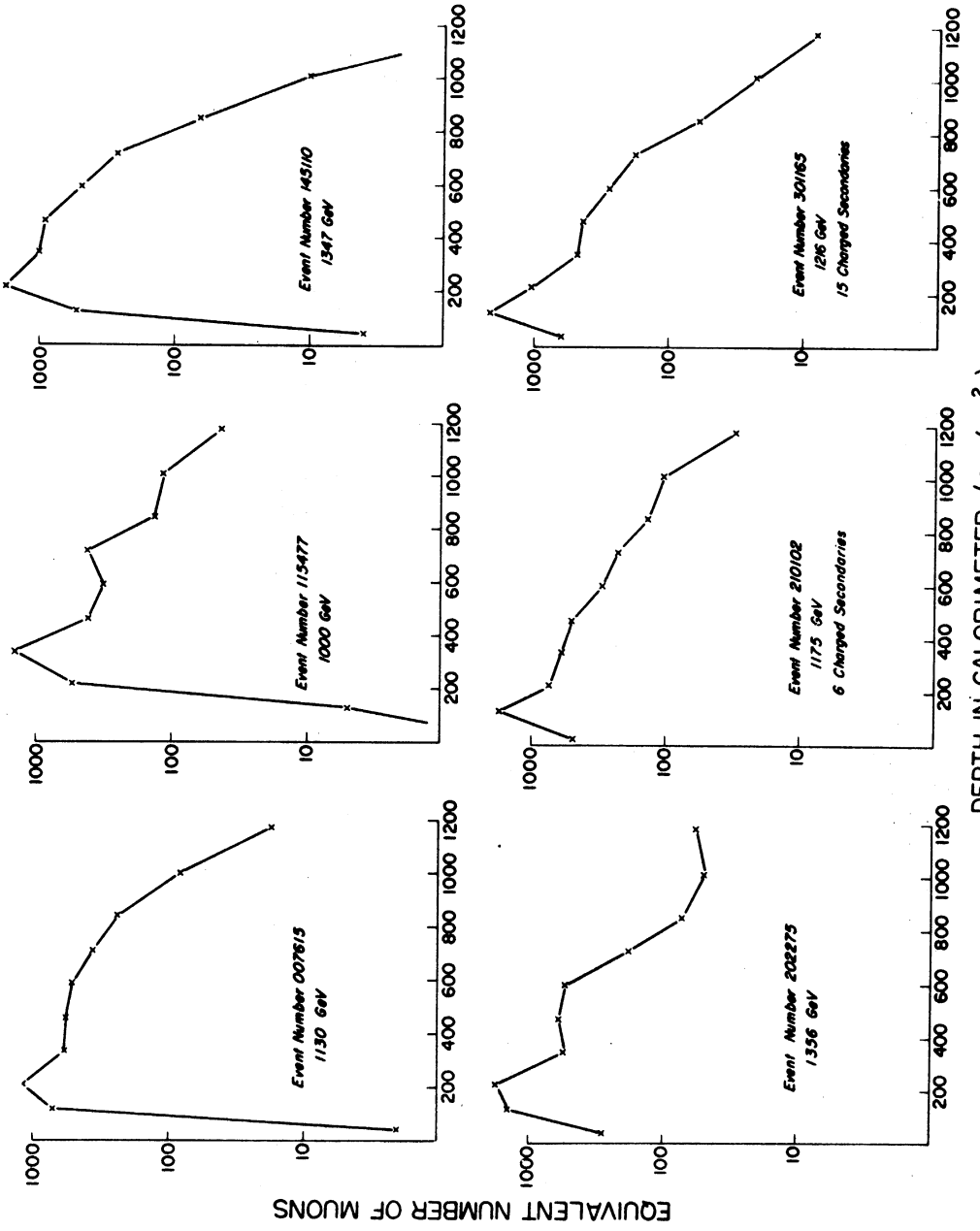

FIG. 17 INDIVIDUAL EVENT IONIZATION CURVES. ENERGY ABOUT 1000 GeV.

in the scintillator. Since each N_i observed already contained sec θ when it was measured, it was not necessary to alter the equation for E_I to account for angles of the incident tracks.

The calculated number of equivalent muons in a layer was the result of sampling ionization from two sources. One source was the predominately relativistic particles in the cascade of charged hadrons that lost energy through electromagnetic interactions with the iron and scintillator as well as produced neutral pions in successive nuclear interactions. The neutral pions in turn decayed into γ-rays and initiated electromagnetic cascades. The other source of ionization was the disintegration products of iron and scintillator nuclei struck by hadrons in the nuclear cascade. The observed energy of an event can be written as the sum of ionization energy from these two sources.

$$E_o = E_{no} + E_{eo} .$$

The subscript o refers to the observed energy, no refers to the energy of the incident hadron observed in nuclear disintegration products, and eo is the remainder. The light output of the scintillators which sampled ionization on the average represented about half of the true energy of the incident hadron which was deposited in nuclear disintegrations, E_{nt}.

$$E_{no} = \frac{1}{2} E_{nt} .$$

This is a consequence of disintegration sites which were in the scintillator or close enough to it to allow measurement of ionization of disintegration products. The details of the calculation to determine the fraction of E_{nt} which was observed are discussed in Appendix A.

The true energy of the event, designated by the subscript t, may also be written as the sum of energy deposited in nuclear disintegrations and a remainder due mainly to electromagnetic cascades resulting from neutral pion decay.

$$E_t = E_{nt} + E_{et} \quad .$$

The ionization resulting from electromagnetic showers and the electromagnetic interactions of the hadron shower is related to the observed ionization energy E_I. The energy calculated from the electromagnetic and hadron shower ionization, E_{et}, in a single layer of the calorimeter, j, is

$$E_{et}(j) = f_j[E_o(j) - E_{no}(j)] \quad .$$

Summing over all layers of the calorimeter containing the shower results in the following equation:

$$E_{et} = \sum_{j=B}^{L} f_j E_o(j) - \sum_{j=B}^{L} f_j E_{no}(j) \quad .$$

The summation over all observed ionization energy is E_I, the calculated energy, neglecting any correction for nuclear disintegration energy losses. The energy E_{et}, is then

$$E_{et} = E_I - \sum_{j=B}^{L} f_j E_{no}(j) \quad .$$

The remaining summation represents that half of the nuclear disintegration energy which was observed and added to E_I with a correction factor for the transition effect, f_j. Since most of the nuclear encounters of the hadronic cascade occur between layers 2 and 10 of the calorimeter it is reasonable to factor $f_j = 10/9$ out of this sum.

$$\sum_{j=B}^{L} f_j E_{no}(j) = \frac{10}{9} \sum_{j=B}^{L} E_{no}(j) = \frac{10}{9} E_{no} \quad .$$

The equation for E_{et}, expressed in terms of E_I and E_{no}, is then

$$E_{et} = E_I - \frac{10}{9} E_{no} \quad .$$

The true energy of the event is

$$E_t = E_{nt} + (E_I - 10/9 \cdot 1/2 E_{nt}) \quad .$$

Dr. W. V. Jones [1] used his Monte Carlo program to simulate the nuclear-electromagnetic cascade in the Echo Lake calorimeter.

Figure 18 indicates his calculation of the fraction of the total energy which goes into nuclear disintegrations, E_{nt}/E_t. This calculated fraction agrees well with the Monte Carlo results of E. V. Denisov et al. [28]. The energy dependence is consistent with the tentative number of nuclear encounters in the cascade calculated by V. S. Murzin [22]. Each nuclear encounter contributes 800 MeV to the energy going into nuclear disintegration in Murzin's model. The central line in Fig. 18 is the mean (E_{nt}/E_t) calculated by Dr. Jones, and the two outer lines indicate one standard deviation on either side of this, assuming a symmetric distribution. The average can be fit very well over the full range of energy by the equation

$$\frac{E_{nt}}{E_t} = \frac{12.22}{E_t + 35.13} + 0.217 \quad .$$

The more efficient sampling at higher energies is due to a larger fraction of the energy going directly and indirectly into neutral pion production resulting in a well sampled electromagnetic cascade.

A reasonable approximation for the energy of each event was made by combining the last two equations. The result is expressed in terms of the measured ionization energy E_I, of the event.

$$E_t = \frac{B + \sqrt{B^2 - 4AC}}{2A} \quad ;$$

$$A = 0.90356 \quad , \quad B = E_I - 26.311 \quad , \quad C = E_I - 35.13 \quad .$$

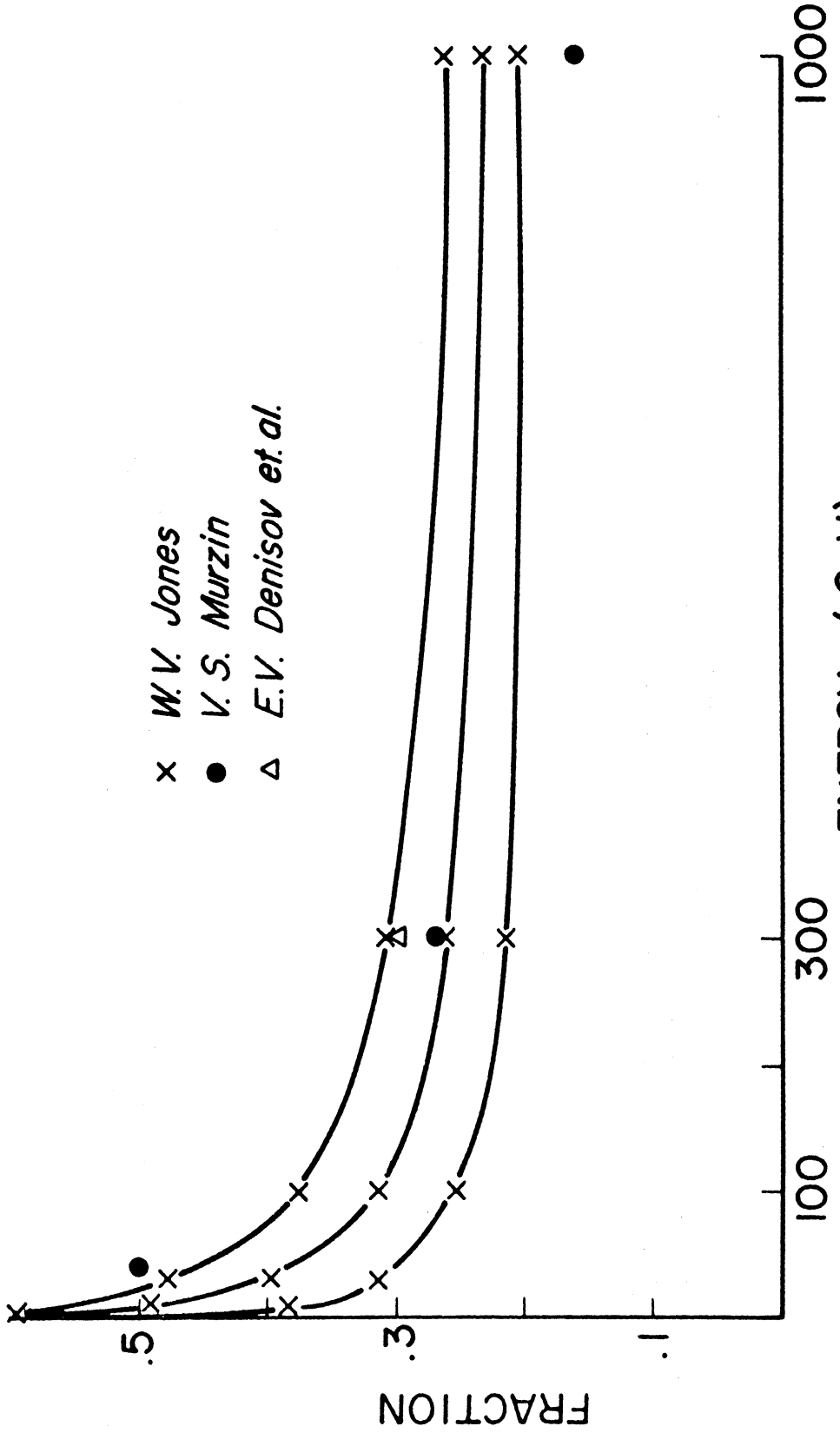

FIG. 18 FRACTION OF INCIDENT ENERGY DEPOSITED IN NUCLEAR DISINTEGRATIONS.

D. Event Selection

The number of interactions N_I, which occur when N particles traverse homogeneous material is

$$N_I = N(1 - e^{-\ell/\lambda_{pN}}).$$

The constant λ_{pN}, is the average distance which a particle travels in target material before it interacts with an atomic nucleus. For the remainder of this paper both the path length in target material, ℓ, and the interaction lengths λ, are expressed in units of gm/cm^2. The relationship between interaction length λ_{pN}, and cross section σ_{pN}, is

$$\lambda_{pN}(E) = \frac{A}{N_o \sigma_{pN}(E)} .$$

The constants A and N_o are the atomic number and Avagadro's number, respectively.

The proton-iron inelastic cross section was determined by measuring the interaction length λ_{pN}. The properly normalized probability distribution for an interaction at a depth ℓ, is

$$p_I = \frac{e^{-\ell/\lambda_{pN}}}{\lambda} .$$

Because of the various directions of the incident hadrons, the distance ℓ was different for each event. A description of the maximum likelihood

fit to the interaction length λ, which uses the probability p_I, is presented in Chapter IV, Section B.

The probability p_I, could have been used to determine the proton-proton inelastic cross section. If a total of N particles was incident on the liquid hydrogen, the number of particles which interact N_I, is

$$N_I = \sum_{i=1}^{N} \int_{o}^{\ell_i} p_I \, d\ell \quad .$$

The upper limit of the integral ℓ_i, is the distance along the trajectory of the incident particles in the liquid hydrogen. Performing the integral and rewriting the last equation, the accumulated number of interactions is

$$N_I = N - \sum_{i=1}^{N} e^{-\ell_i/\lambda_{pN}} \quad .$$

Instead of using this method, a thin target approximation was made to determine the cross section. Assuming that the proton-proton inelastic cross section is 30 mb, the value known at 20 GeV, the corresponding interaction length is 55.3 gm/cm^2. The ratio of the average path length in hydrogen, 3.86 gm/cm^2 to this interaction length is

$$\frac{\ell}{\lambda} \simeq 0.07 \quad .$$

Since this ratio is small, the probability for an interaction was almost the same for all ℓ in the hydrogen. The upper limit for the integral

over p_I was taken as the average value of the path length for non-interacting events.

$$N_I = N \int_0^{\ell_{av}} \frac{e^{-\ell/\lambda}}{\lambda} d\ell \quad .$$

This equation, rewritten in terms of the cross section, σ_{pp}, is

$$\sigma_{pp} = \frac{A}{N_o \ell_{av}} \log_e \left[1 - \frac{N_I}{N} \right] \quad .$$

The numbers for N_I and N used to determine the proton-proton inelastic cross section were from the scanned number of events within a specific fiducial volume. The events were scanned according to the criteria listed in Section A of this chapter. Reconstruction of all interactions was attempted. Those events which were measured and failed reconstruction were remeasured up to three times. Those that still failed reconstruction were distributed into all energy bins as 5.5 percent of the number of reconstructed events in the bins. Events which did not interact in the target were also reconstructed. From the scanned number of events, including non-interacting events with an accompanying δ-ray, a sample of 5×10^4 events was reconstructed. This amounted to 77 percent of the scanned one prong events. Here again the events which were not measured were distributed like the reconstructed events. Discussion of this treatment of events, along with tables of numbers will be presented in Chapter IV, Section D.

Not all events that triggered the system were acceptable for use in calculating a cross section. There were three criteria for determining useful events. First, the reconstructed trajectory of the event must have passed within a specified fiducial volume. Second, for the proton-proton cross section, interacting events must have had a vertex in the liquid hydrogen, not the target walls. Third, the energy of each event must have been above the low energy region where the triggering threshold affects the binning of events.

The parameters that determined fiducial volume were defined in the coordinate system shown in Fig. 12. For each event, the trajectory of the incident particle was determined by the reconstructed track in the upper spark chamber and then extrapolated through the calorimeter.

Events were considered hydrogen interactions only if they did not have a vertex within 1 cm of the stainless steel flask or the fill and vent pipes within the target. The 1 cm corresponded to the z-vertex resolution for target interacting events. With this restriction, most of the interactions that occurred in the steel flask and aluminum container were eliminated. Some hydrogen events were also discarded. The average path length in hydrogen along the trajectory of the event was determined from events which did not interact in the target. The depth of liquid hydrogen in the target as a function of time was shown in Fig. 6. The level of hydrogen in the target for a particular event was determined by combining that information with the approximate

elapsed time between the last target fill and when the event occurred. The level of the hydrogen or the upper dome of the flask was the entry point into liquid hydrogen and the lower dome was the exit point. The distribution of path lengths, of which the average value is 54.6 cm, is shown in Fig. 19. The extrapolated primary trajectory was required to pass within 91.4 cm of the x- and y-axis at the level of the top counter, within 90.0 cm of these axes at layer two of the calorimeter, and within 110.0 cm at layer eight. These boundaries were chosen so that at least for events that did not interact in the target, the nuclear-electromagnetic cascade would be fairly well contained within the calorimeter. Table II shows the amount of scintillator in layers 1 through eight which continued beyond the fiducial volume boundaries.

The energy of each reconstructed event was calculated with a layer by layer ionization correction based on the extrapolated trajectory of the incident hadron. The energy used in the hadron coincidence to trigger the system was determined only by ionization with no correction for the area through which shower particles traversed the scintillator. Therefore, close to threshold the trigger tended to select events which showed considerable ionization because they traversed the scintillator close to the phototubes. The energy of reconstructed events was often quite different from the trigger energy, and for the 90 GeV threshold, events down to 30 GeV triggered the system. Energy bins for reconstructed events were chosen to be $\pm$ 20 percent of the mid-energy of a bin with the lower edge of the first bin set at 34 GeV. Two triggering threshold energies were used, one of 36 GeV and the other of 90 GeV.

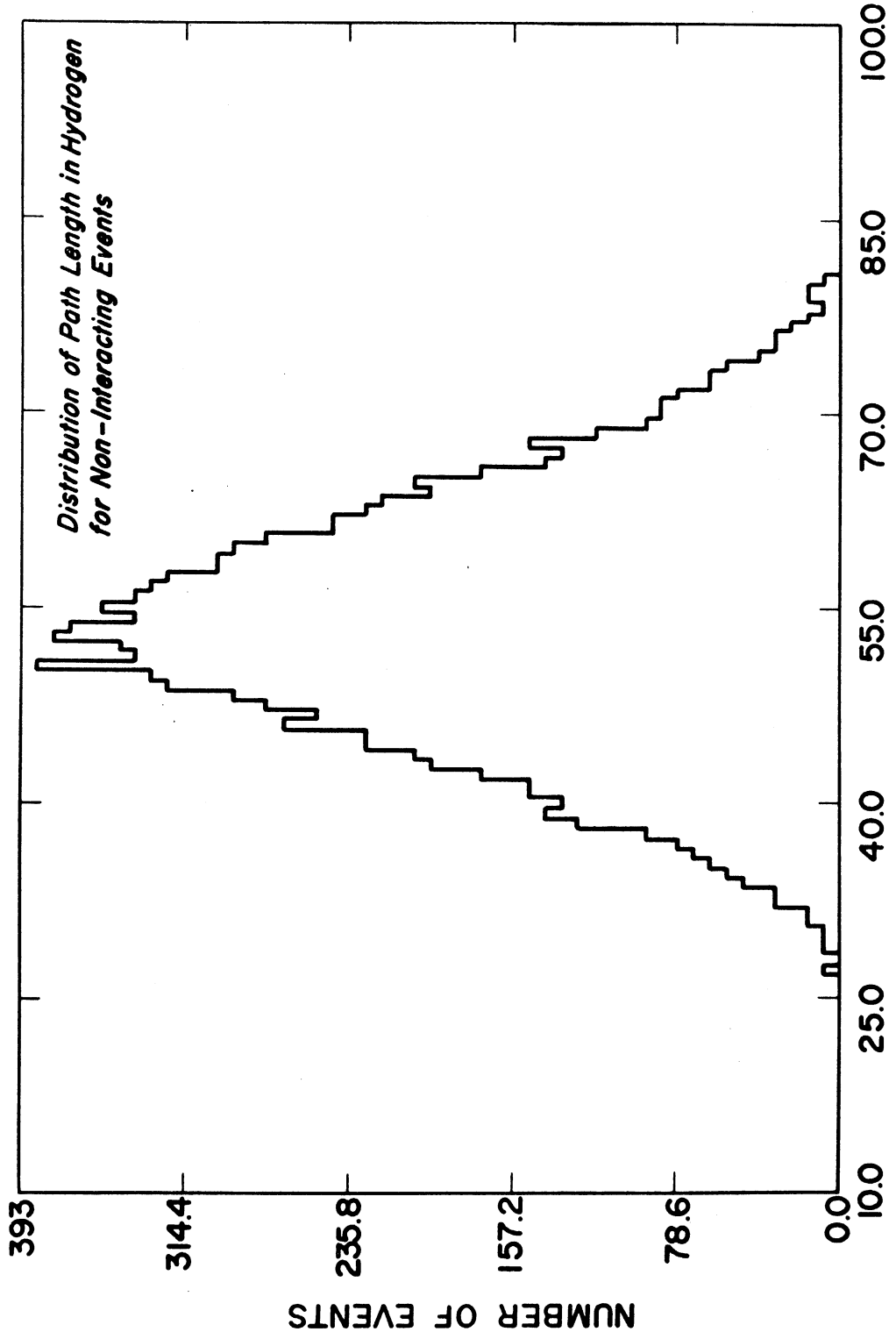

FIG. 19 DISTRIBUTION OF THE PATH LENGTH IN THE HYDROGEN TARGET OF NON-INTERACTING EVENTS.

Table II

The Distances from the Edge Extremes of the Fiducial Volume Cut to the Edge of the Scintillator

Calorimeter Layer	Vertical Coordinate (cm)	Margin (cm)
Top Counter	120.13	0
Layer		
1	-131.3	1.4
2	-155.7	1.44
3	-184.9	27.5
4	-205.8	24.3
5	-226.4	21.2
6	-247.0	18.1
7	-267.6	15.0
8	-287.9	11.9

The energy bins just above threshold energy were adversely affected by the triggering method. The coincidence which indicated that an interesting event had occurred included a calorimeter signal which was a discriminated pulse of a weighted sum of the voltages from the various phototubes of the calorimeter. Structure in the pulse which was discriminated resulted in many events above threshold energy not triggering the system. The energy of reconstructed events was calculated with the corrected LADC output which was a measure of the area under the voltage pulse, not the voltage pulse height at some instant. The dispersion of the electron collection times in the photomultiplier tubes makes the area under the voltage pulse a more reliable measure of the total amount of light observed in the scintillator. Because of differences between the energy sum used in the trigger and the energy of reconstructed events, the most populated energy bins that are near threshold were not used in the calculation of cross sections. In order to use energy bins that were not affected by the triggering threshold, only events above 211 GeV were used from the 90 GeV threshold running, and events above 71 GeV from the 36 GeV running. At these energies threshold effects were no longer apparent. Three of the most apparent effects of the trigger biases were a reduction in the cross section near threshold, a cascade development which reached its maximum deeper in the calorimeter and a leveling off of the energy spectrum that at higher energies was proportional to E^{-3}. The second effect was caused by the combination of an energy underestimate by the trigger and an ionization overestimate of events close to the phototubes in layers 3 through 9 of the calorimeter.

E. Interacting Events

Multiple prong events were studied to determine if the secondaries were indeed from a strong interaction vertex. Events with two and three visible charged tracks in the lower wide gap spark chamber were examined to make sure that the secondaries were hadrons and not electrons (δ-rays) produced in a "knock-on" process. Delta rays posed a serious problem to the proper counting of events. Spark chamber efficiency, prongs not traversing the lower spark chamber, one prong interactions, and the resolution of the opening angle between tracks, also affected the counting of events.

Events with two and three tracks in the lower spark chamber were studied on the scanning table to determine whether the tracks were from a strong interaction or if there was only one hadron with accompanying δ-rays. If a track in the lower spark chamber showed any deviation from a straight line it was called a δ-ray. Electrons produced in a "knock-on" process with less than 50 MeV were very likely to Coulomb scatter noticeably, about 0.5 degree in the 51 μ aluminum foils of the spark chamber. The remaining two and three prong events, which had straight tracks in the lower spark chamber, were grouped into categories depending upon how deeply the tracks accompanying the on-going particle penetrated into the iron plate spark chamber. Secondaries from a strong interaction, which are mostly pions, would penetrate all ten gaps of the iron plate spark chamber or interact and initiate a nuclear-electromagnetic cascade in the iron. The kinetic energy of the

pions and protons that penetrate to the depths of the various gaps of the iron plate spark chamber is given in Table III [29]. A Monte Carlo program was developed by D. Lyon and C. Risk to investigate properties of a Reggeized multiperipheral model and compare it with the observed interacting events [30]. This Monte Carlo program, that is referred to later, indicated that 8 percent of the pions which produce tracks in the lower wide gap spark chamber would not penetrate all ten gaps of the iron plate spark chamber. Moreover, virtually none of the charged pions would have a range of less than five gaps.

Interactions in which only neutral pions were produced would most often result in one prong events which would be grouped incorrectly. Monte Carlo results indicate that some of the recoil protons have a range in the calorimeter no greater than that of the electrons and some of the recoil protons completely miss the lower wide gap spark chamber. The neutral pions decayed into γ-rays which sometimes produced electron-positron pairs in the target. These charged particles appeared as a track in the wide gap spark chamber and as an electromagnetic cascade in the iron plate spark chamber. The number of inelastic one-prong events was estimated, on the basis of Monte Carlo analysis, to be 4 percent of the number of inelastic interactions. It is significant to note that the number of events grouped as δ-rays and included as non-interacting events is very close to the calculated number of δ-rays that should be observed.

Hadronic secondaries were differentiated from δ-rays on the basis of their observed range into the iron plate spark chamber. In order to check the scanning procedure, the number of δ-rays with minimum

Table III

Approximate Range Energy Relations for Pions and Protons in Iron

Range (gm/cm^2)	Kinetic Energy (MeV)	Total Energy (MeV)
	Protons	
15	115	1053
35	188	1126
60	260	1198
80	310	1248
100	353	1291
120	400	1338
145	450	1388
165	490	1428
185	525	1463
205	560	1498
	Pions	
15	53	193
35	92	232
60	133	273
80	164	304
100	193	333
120	225	365
145	260	300
165	290	430
185	310	450
205	350	490

energy E_m, sufficient to penetrate to the first, second, and third gaps of the iron plate spark chamber was calculated. These calculated numbers were than compared with the number of δ-rays observed in the three gaps. The calculated numbers of δ-rays were based on an incident flux of 66,000 charged hadrons consisting of both pions and protons. The differential collision probabilities [31] for a proton and pion of mass m, and energy E, to produce an electron with energy between E' and E'+dE' while traversing a thickness $d\ell$, are:

$$\Phi^{P}_{col}(E,E')\,dE' = \frac{2Cm_e c^2}{\beta^2}\,\frac{dE'}{(E')^2}\left[1 - \beta^2\,\frac{E'}{E'_M} + \frac{1}{2}\left(\frac{E'}{E + mc^2}\right)^2\right]$$

$$\Phi^{\pi}_{col}(E,E')\,dE' = \frac{2Cm_e c^2}{\beta^2}\,\frac{dE'}{(E')^2}\left[1 - \beta^2\,\frac{E'}{E'_M}\right] .$$

The maximum transferrable kinetic energy E'_M, for protons and mesons with $\gamma >> 1$ is approximated by the relation

$$E'_M \simeq E .$$

The other terms in the equations are m_e, the mass of the electron, and C, which is

$$C = 0.150\,\frac{Z}{A} \;;\; cm^2/gm .$$

The probability that an event will produce a δ-ray in the target materials with an energy greater than E_m is

$$P(E_m < E < E_M) = 2C \frac{m_e c^2}{\beta^2} \left[\frac{1}{E_m} - \frac{1}{E_M} - \frac{\beta^2}{E_M} \ln\left(\frac{E_M}{E_m}\right) + \frac{F_P}{2E_M^2} (E_M - E_m) \right] .$$

The coefficient F_P, represents the fraction of the flux which is protons, about 0.77. This fraction is discussed in the following section. The function $P(E_m < E < E_M)$, is the probability that the incident hadron produce a δ-ray while traversing a thickness $d\ell$ of target material. The effect of producing "knock-on" electrons in the three materials of the target may be included in the coefficient:

$$\frac{2Cm_e c^2}{\beta^2} = 2m_e c^2 \left[\ell_{Al} \frac{Z_{Al}}{A_{Al}} + \ell_{Fe} \frac{Z_{Fe}}{A_{Fe}} + \ell_H \frac{Z_H}{A_H} \right] = 0.9677 \text{ MeV} .$$

High energy electrons lose energy while traversing the material of the target, lower wide gap spark chamber, and iron plate spark chambers. The range of δ-rays in the absorbing material indicated the energy of the knock-on electrons produced. The quantity E_m, was the energy necessary for a δ-ray, produced half way through the target by a 200 GeV hadron, to persist through the different materials to the first, second, and third gaps of the iron plate spark chamber. The calculation of E_m was based on the results of R. Wilson [32]. A comparison between the number of predicted and observed δ-rays is shown in Table IV.

The number of observed and predicted δ-rays was in reasonable agreement in gaps 2 and 3. The low number of observed δ-rays in gap 1

Table IV

Comparison of the Observed and Predicted Number of Delta-Rays. Predicted Number of Delta-Rays Was Calculated on the Basis of 66,000 Hadrons Traversing the Target.

Gap of Iron Spark Chamber	E_m (MeV)	$P(E_m<E<E_M)$	Number Predicted	Number Observed
1	77	1.253×10^{-2}	827	437
2	586	1.679×10^{-3}	111	107
3	4890	1.828×10^{-4}	12	31

is due to inefficient sparking in this particular spark gap. If a track continued more than three layers into the calorimeter it was considered as a hadron. Some observed two prong events where one prong is a very low energy hadron, $E_p < 1.25$ GeV or $E_\pi < 0.3$ GeV, may have been rejected by deleting two prong events in this way. These events will eventually be added in a correction to the cross section based on Monte Carlo results.

The smallest angle between tracks which could be resolved on the scanning table was between 2 and 3 mr, depending on the spark quality. Here again Monte Carlo results indicate that the number of events with all tracks within this small an opening angle in the laboratory is negligible. Only 2 percent of all secondary prongs have an opening angle less than 2.5 mr and less than 20 percent of the interactions are observed as two prong events. The resulting correction would be less than 0.4 percent and was neglected.

F. Non-Interacting Events

The group of events which satisfied the selection criteria and traversed the target without interacting consisted of incident protons, pions and muons. Included in the group of one-prong events were elastically scattered particles as well as some inelastic interactions with missing or no charged prongs. This section is concerned with the proper counting of non-interacting events and the necessary corrections to the cross section to eliminate systematic biases.

In order to correct the measured cross sections so that they correspond to proton-proton and proton-iron results, the fraction of pions in the incident hadron flux was determined. This was done by

experimentally determining the neutral to charged particle ratio in the incident flux. The neutral particles were neutrons produced in the interactions of primary cosmic ray protons with the atmosphere. The model of Pal and Paters [33], which considers the production of neutrons in proton air collisions, was used to calculate the neutron to proton ratio of the incident hadron flux. With this ratio and the neutral to charged ratio the fraction of pions in the incident beam was calculated. The following analysis was done by P. Viswanath [34].

Charged hadrons which trigger the system are mainly protons and charged pions. In order to estimate the ratio of pions to protons in the flux, the system was triggered with a threefold coincidence of layer 2 of the calorimeter, the summed calorimeter signal, and no signal from the anti-shower counter array. A run with this trigger yielded 7900 useable events which were analyzed to determine the neutral to charge ratio of the incident hadrons. Events passing through the central portion of the spark chamber were grouped into two energy bins: 100-200 GeV, and 200-500 GeV. Events with tracks in both wide gap spark chambers and in the iron plate spark chambers were called charged hadrons. Events with no track in the upper wide gap spark chamber, which was 100 percent efficient for single tracks with the geometry cut used, and with a definite cascade developing in the iron plate spark chamber were called neutral hadrons. Only a very few neutral events had tracks in the lower wide gap spark chamber. Table V indicates the observed number of neutral and charged events and a corrected number of neutral events. It was necessary to correct the observed number of neutrons to also include neutrons

Table V

Observed and Corrected Number of Neutral Events and the Neutral to Charged Particle Ratio

	Energy Range	
	100-200 GeV	200-500 GeV
Observed Number of Neutral Events	184	91
Corrected Number of Neutral Events	298	146
Number of Charged Events	466	210
Neutral to Charged Ratio	$.63 \pm .07$	$.70 \begin{smallmatrix} + .11 \\ - .10 \end{smallmatrix}$

which had not interacted by layer 2. This correction was based on a neutron iron interaction length of 124 gm/cm^2.

The model of Pal and Peters [33] predicts a proton to neutron ratio at 700 gm/cm^2 of atmosphere of 1.20. This results in an estimate of the pion to proton ratio to be

$$\frac{\pi}{P} = 0.32 \begin{matrix} + 0.15 \\ - 0.13 \end{matrix} \qquad \text{for 100-200 GeV}$$

$$\frac{\pi}{P} = 0.19 \begin{matrix} + 0.18 \\ - 0.15 \end{matrix} \qquad \text{for 200-500 GeV}$$

This result is very sensitive to small errors in the proton to neutron ratio. However, the correction to the proton-proton inelastic cross section for a small admixture of pions is small. Comparing these results with other experiments adjusted to 700 gm/cm^2 a reasonable value of the π/P ratio is 0.3. Assuming the ratio of the pion to proton inelastic cross sections to be the same as at machine energies

$$\frac{\sigma_{\pi-P}}{\sigma_{P-P}} = \frac{2}{3} \ ,$$

the correction to the observed cross section for a π/P ratio of 0.3 is

$$\sigma_{obs} = \frac{3}{13} \cdot \frac{2}{3} \ \sigma_{PP} + \frac{10}{13} \sigma_{PP} \ ,$$

$$\sigma_{PP} = \frac{13}{12} \ \sigma_{obs} \ .$$

It was stated in the last section that some of the events which were inelastic interactions were observed as one prong events because of

missing tracks. The most likely candidates for this kind of event were non-interacting events which had a relatively large scattering angle between the tracks in the upper and lower wide gap spark chambers. A sample of 7900 hadron triggers which satisfied the selection criteria was compared with 7500 in-geometry muon triggers taken without the hydrogen target in place. The muons were measured without first scanning the film, and the spark quality on the film did not vary as much as it did for the long hadron run. Thus the MASS measurement of muon triggers was somewhat better than the measurement of hadron triggers. For both sets of data the distribution of apparent scattering angles between the tracks was fit to a Gaussian distribution over the range from 3 to 9 mr. as shown in Fig. 20. The number of events above the tail of the fit distributions for scattering angles greater than 8 mr was larger for hadrons than muons. The difference amounted to 3.4 percent of the number of observed events. From this analysis, the upper limit of the number of one prong events, based on a proton-proton inelastic cross section of 30 mb, is 33 percent of all interactions. It is more reasonable to consider the difference in the two distributions as a result of trying to measure some poor quality hadron pictures on the MASS scanning machine. This is substantiated by the fact that non-interacting events with a clearly associated cascade development in the iron plate spark chamber, as from a neutral secondary, were very rarely observed. Thus 33 percent was regarded as an upper limit and the Monte Carlo result of 4 percent was used.

High energy muons occasionally triggered the system. Muon triggers were generally the result of bremsstrahlung or direct pair

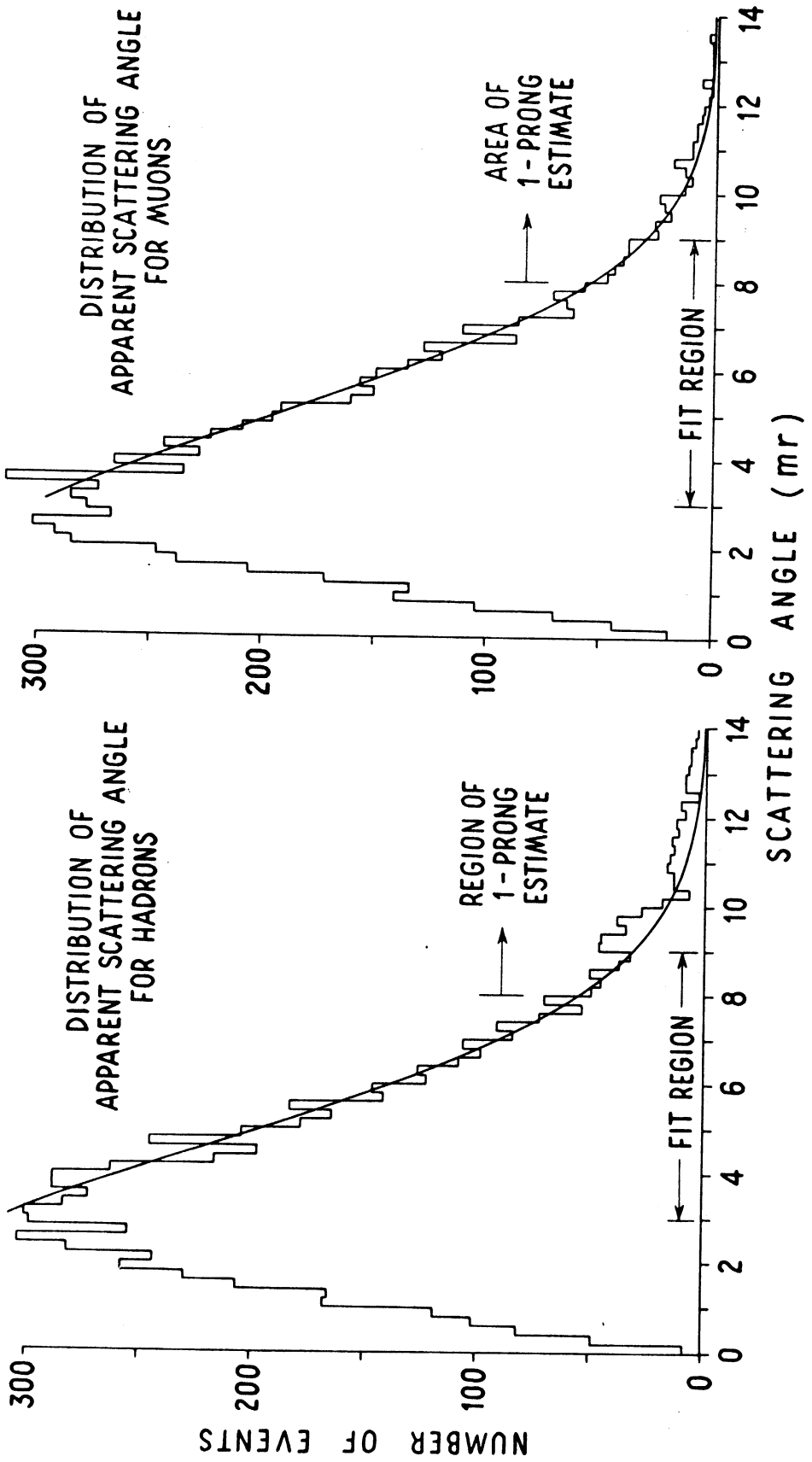

FIG. 20 COMPARISON OF THE SCATTERING ANGLE DISTRIBUTIONS OF HADRONS AND MUONS.

production which produced an electromagnetic cascade. These cascades would persist only one or two calorimeter layers in contrast to the longer shower induced by hadrons. The observed ionization of incident hadrons is also mostly from electromagnetic cascades. However, the shower of charged hadrons which develops in the calorimeter produces neutral pions in successive interactions that initiate electromagnetic showers which are distributed through many layers of the calorimeter. The muon initiated showers begin at all depths into the calorimeter, whereas the hadron interactions are distributed as $e^{-\ell/123}$. The background of one and two layer showers beginning at all depths was 5 percent of the one-prong events. Hence, the number of observed events that did not interact in the target was corrected downward by 5 percent.

An estimate of the fraction of triggers which were caused by muons is discussed in Appendix C. This estimate is based on the calculations of P. V. Ramana Murthy [35]. The result is that between 1 and 5 percent, probably about 2.5 percent, of the triggers are caused by muons. This calculation supports the 5 percent correction to the data.

CHAPTER IV. DATA AND RESULTS

The data presented and discussed in this chapter are related to three topics: the energy measurement of the calorimeter, the proton-iron inelastic cross section, and the proton-proton inelastic cross section. The observed calorimeter data is presented and compared with some pertinent Monte Carlo results of Dr. W. V. Jones [1]. The calorimeter plays an important role in the interpretation of the cross section results and is discussed in some detail. The survival length of single hadrons entering the calorimeter is used to determine proton-iron inelastic cross sections. The energy determination of events that interact in the target is somewhat different from the energy determination of single hadrons entering the calorimeter. The corrections to the observed proton-proton inelastic cross sections and the corrected cross sections are also presented and discussed.

A. Calorimeter Results

Reconstructed events within the fiducial volume were sorted into energy bins according to their energy, which was calculated as indicated in the previous chapter. The events were grouped into bins that were ± 20 percent of the center of the energy bin. However, the energy spectrum of the incident hadrons resulted in the average energy of events in the bin to be 0.96 of the energy at the center of the bin. A few examples

of the observed ionization of single events were shown in Figs. 16 through 18. The fluctuations in the number of equivalent muons are due to the statistical development of the nuclear-electromagnetic cascade. These fluctuations often result in events being binned either above or below the bin including the true energy of the event. Events wherein an extrapolation of the incident trajectory traverses the full ten layers of the calorimeter contain the maximum amount of information about the cascade development. There are some differences between the determination of energy of events which interact in the target as opposed to those that do not. If an event interacts in the target, the lateral spread of secondaries incident upon the calorimeter may result in some prongs exiting from the side. Also, the correction to the observed ionization in a scintillator was not as accurate inasmuch as it was based on the intersection of the extrapolated trajectory of the incident particle with the scintillators in the calorimeter. Therefore, the following results are based on energy bins populated only by single hadrons incident upon the calorimeter which are within the fiducial volume and have an extrapolated trajectory that traverses all ten scintillator layers.

Distributions of the number of equivalent muons in a scintillator layer of the calorimeter are shown in Figs. 21 through 25 for the energy interval from 211 to 303 GeV. Events were sorted into this interval if their energy, determined from a weighted sum of the corrected number of equivalent muons, fell within the specified energy range. Because of

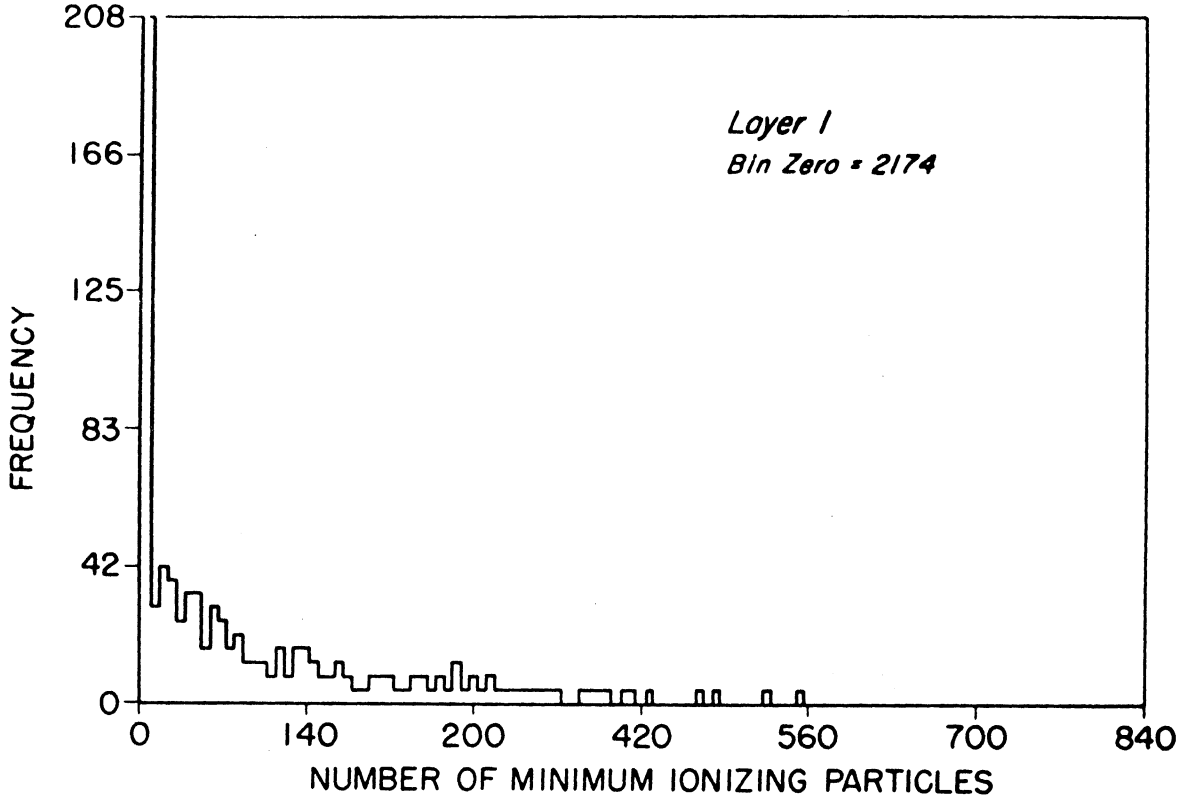

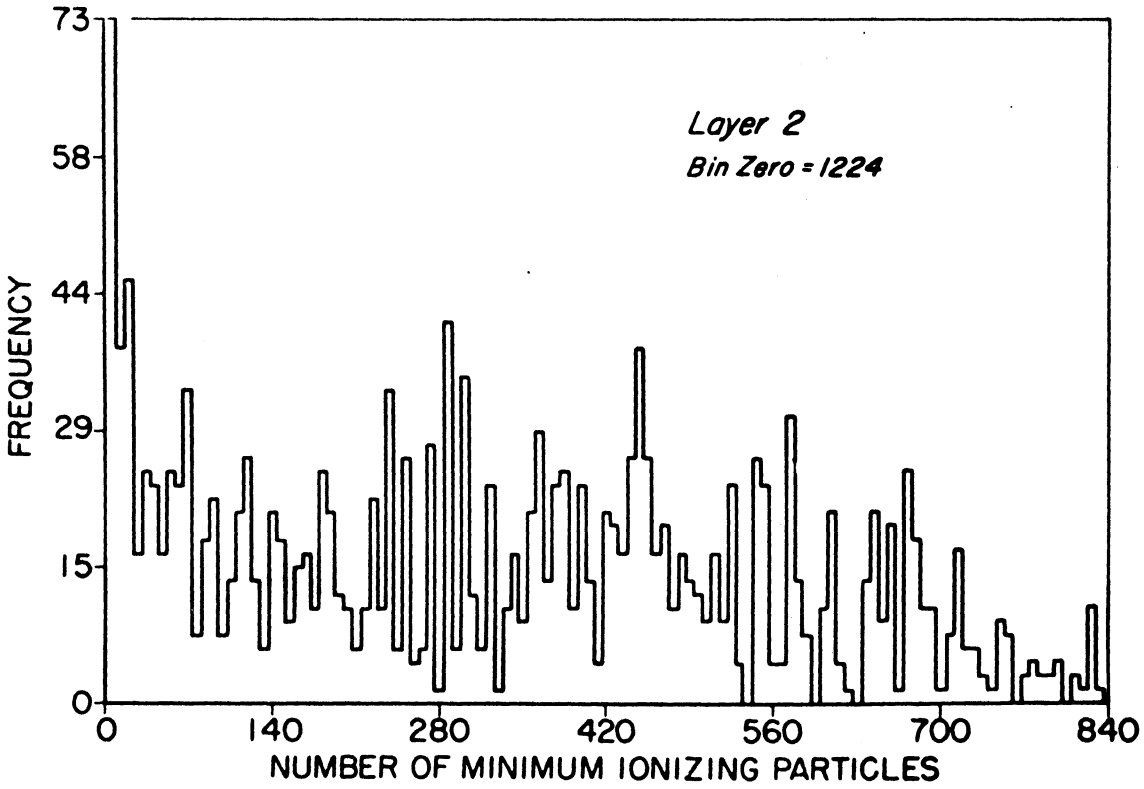

FIG. 21 DISTRIBUTIONS OF THE NUMBER OF MINIMUM IONIZING PARTICLES. (LAYERS 1 AND 2)

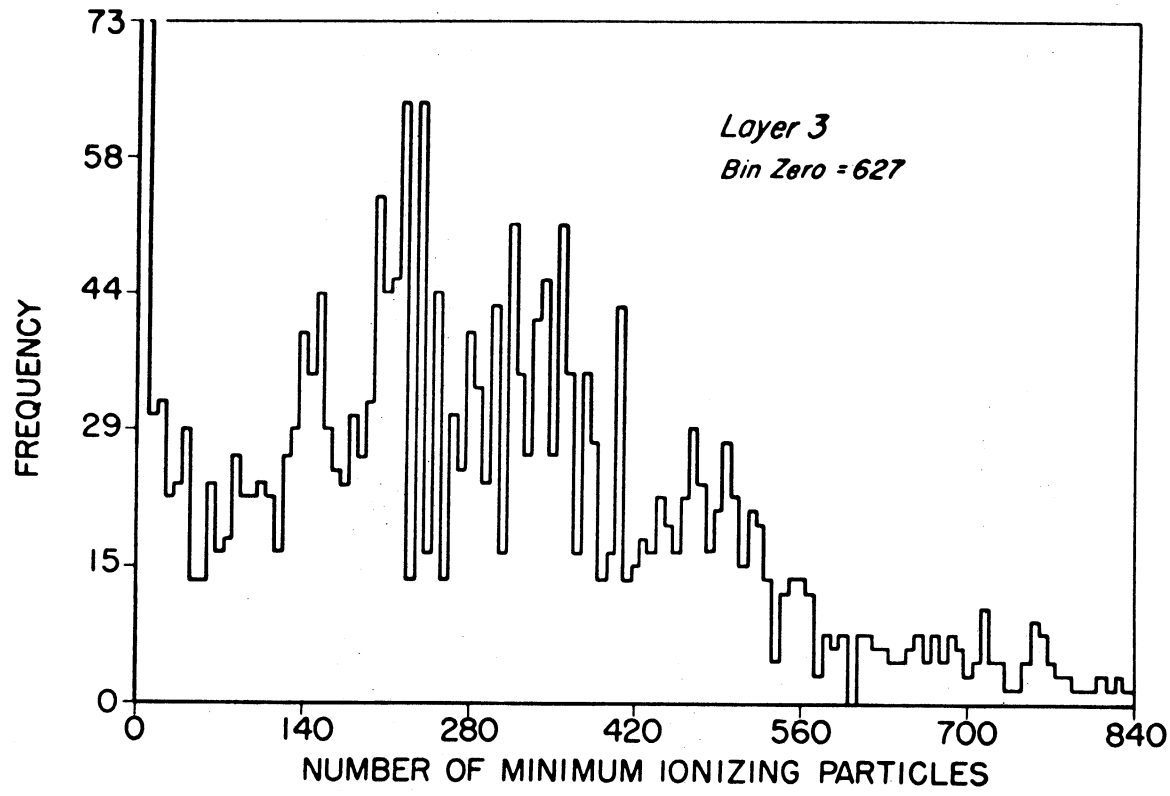

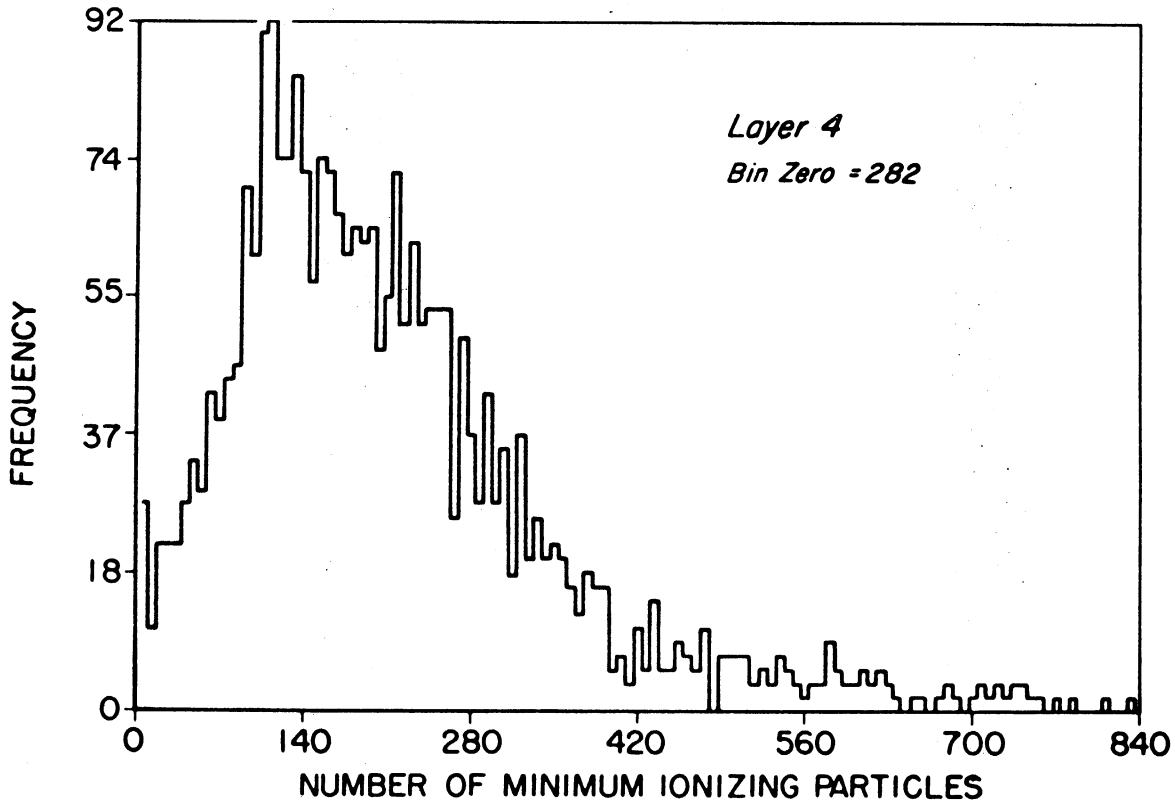

FIG. 22 DISTRIBUTIONS OF THE NUMBER OF MINIMUM IONIZING PARTICLES. (LAYERS 3 AND 4)

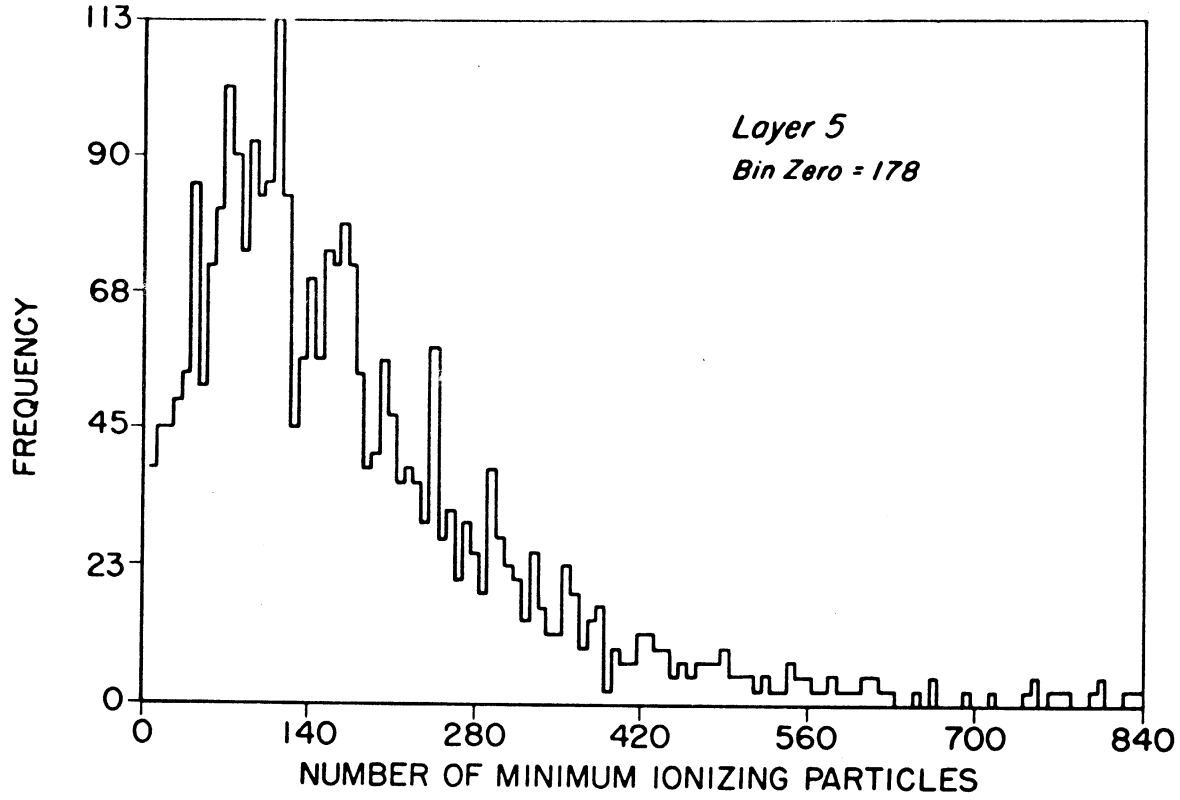

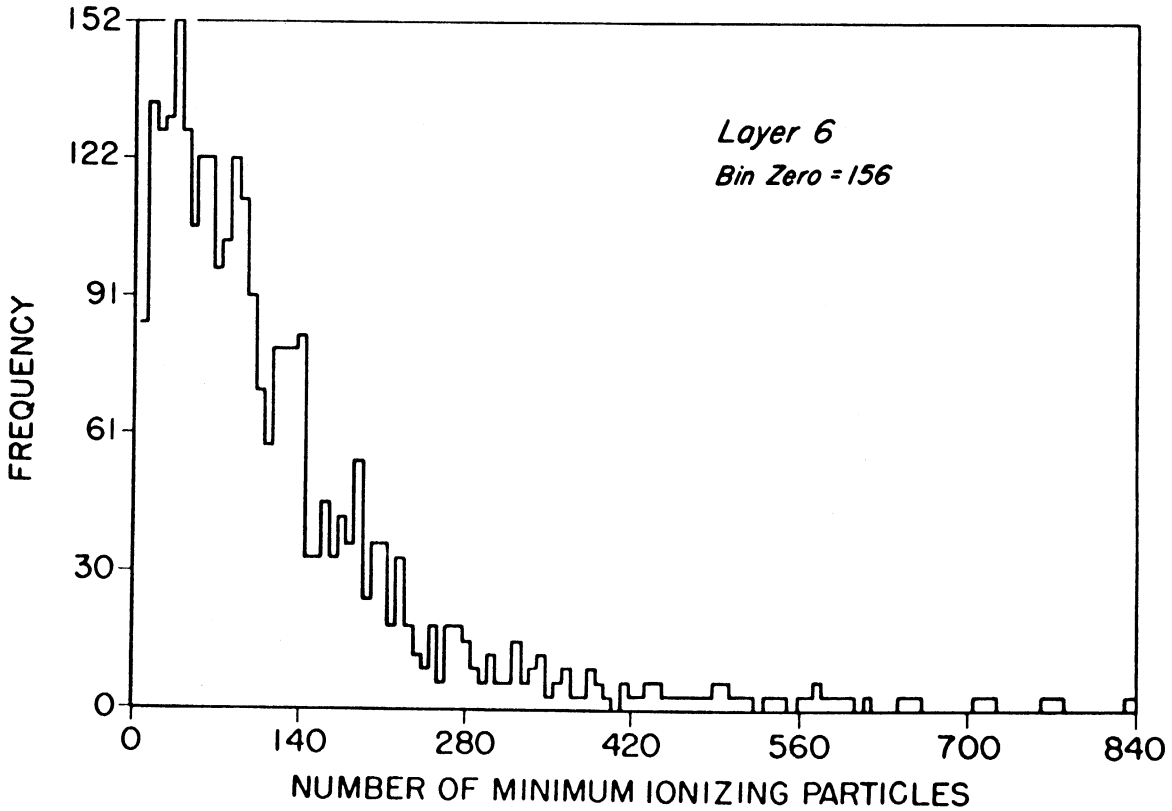

FIG. 23 DISTRIBUTIONS OF THE NUMBER OF MINIMUM IONIZING PARTICLES. (LAYERS 5 AND 6)

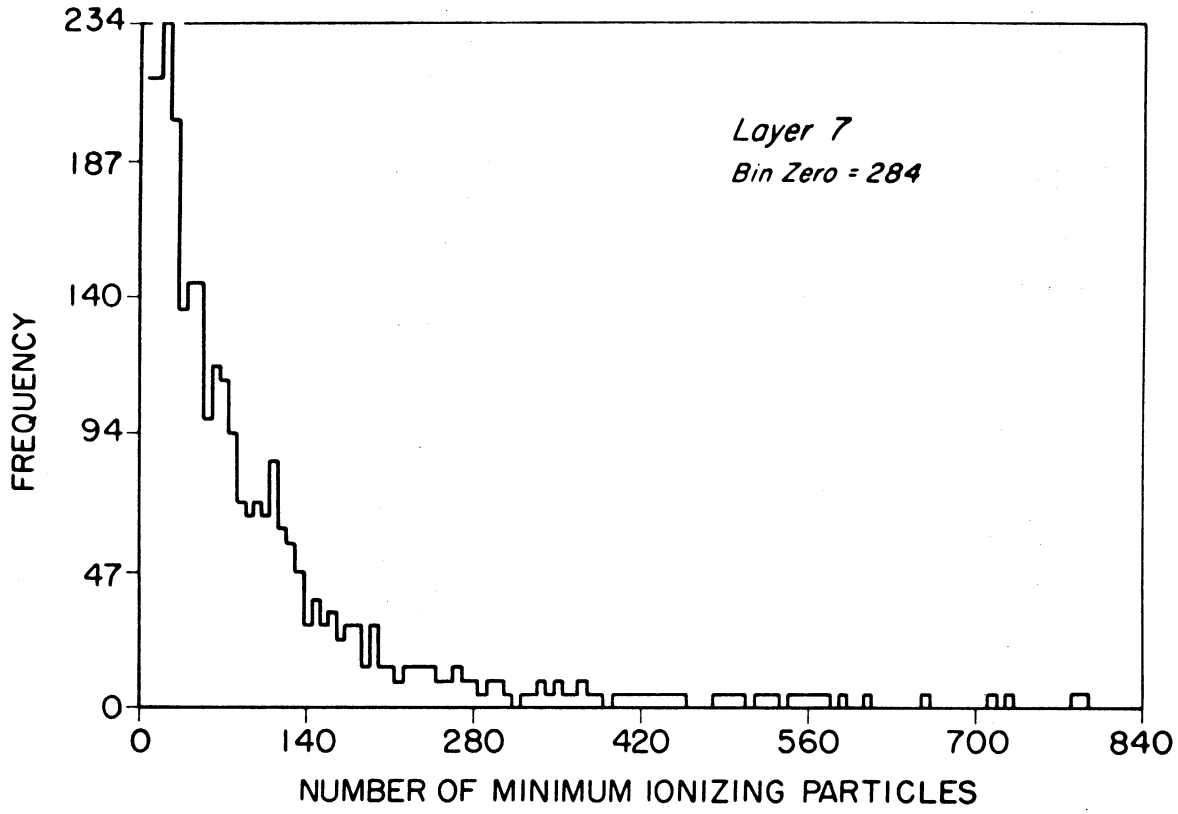

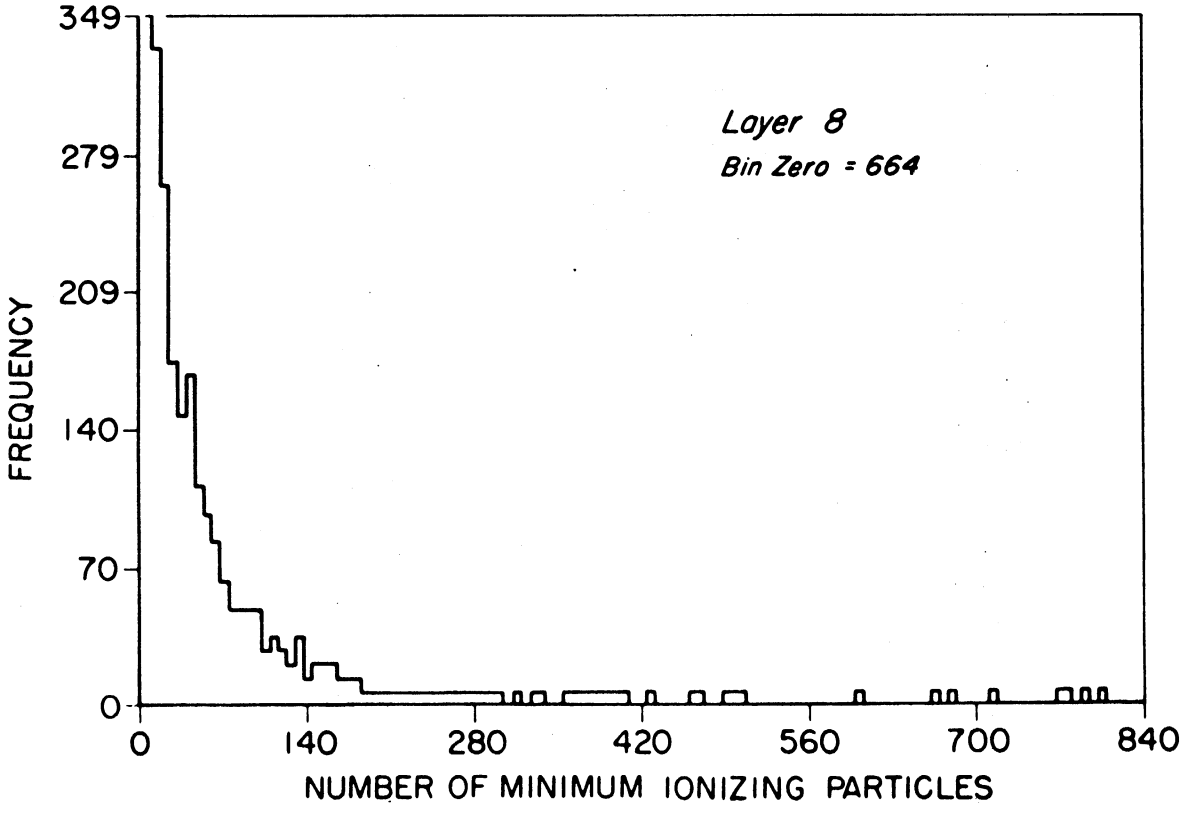

FIG. 24 DISTRIBUTIONS OF THE NUMBER OF MINIMUM IONIZING PARTICLES. (LAYERS 7 AND 8)

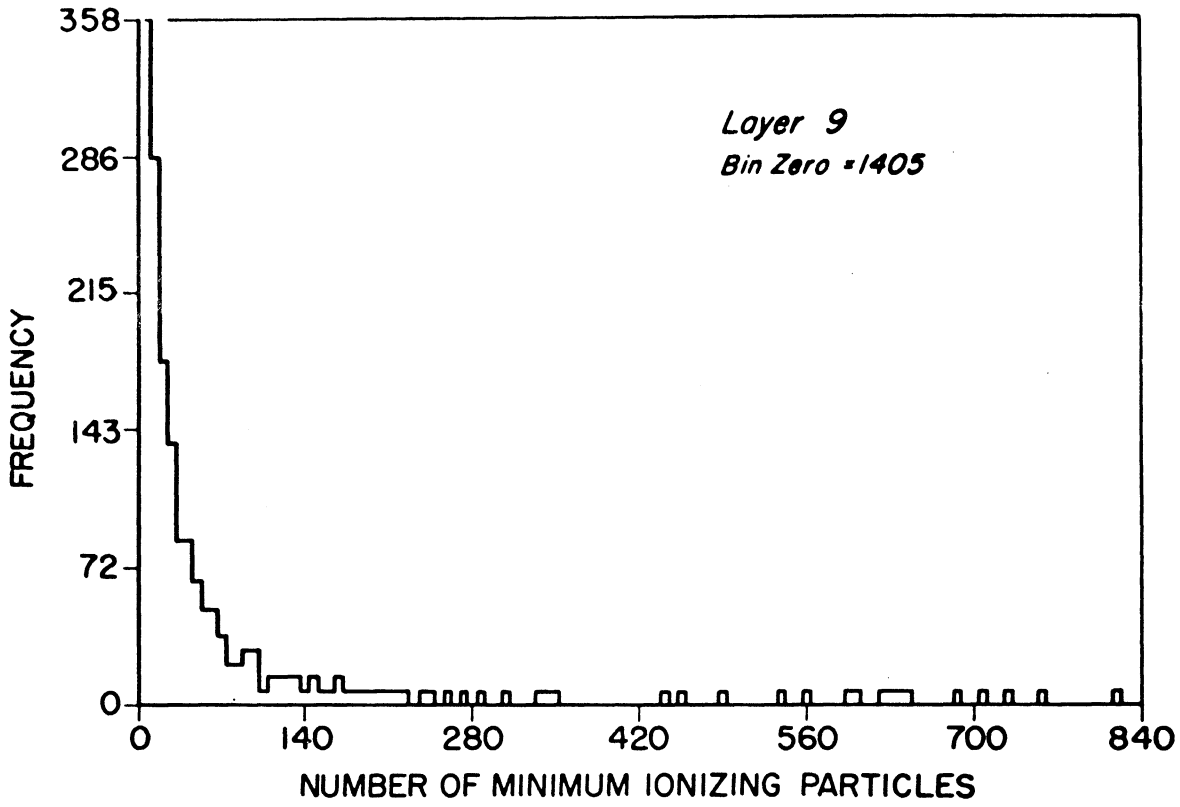

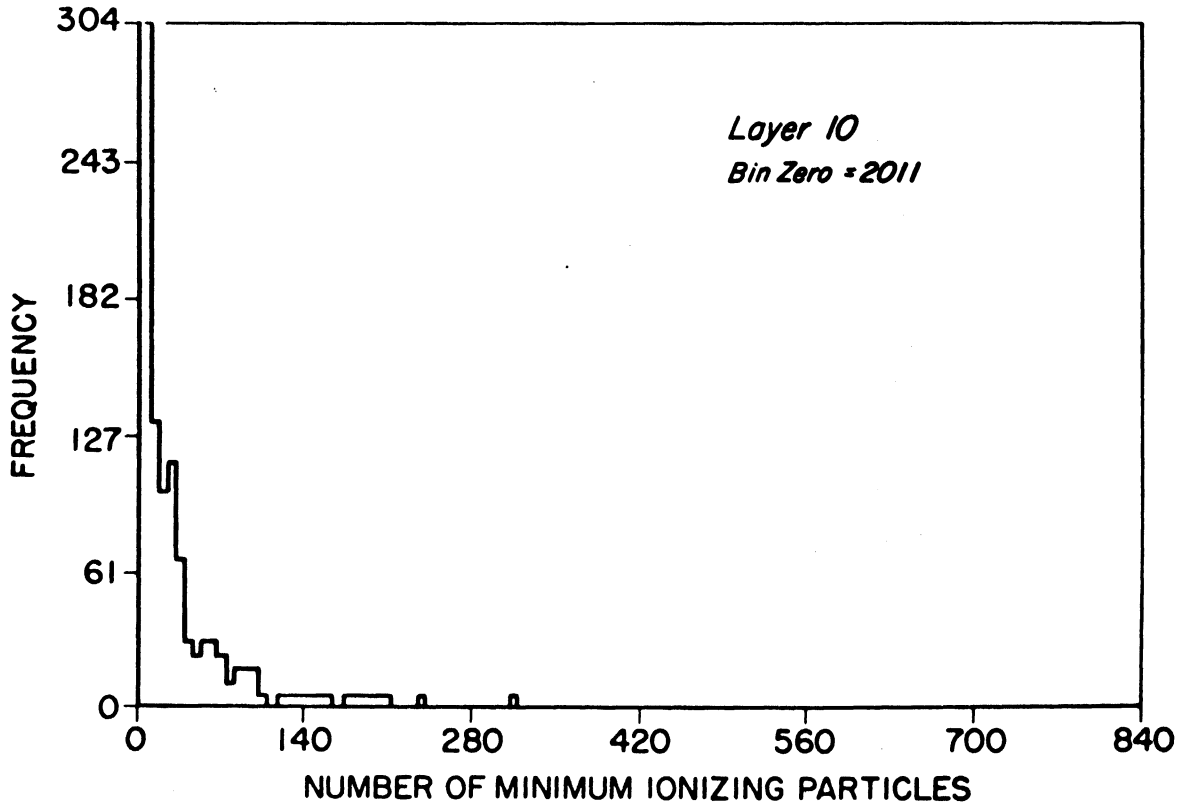

FIG. 25 DISTRIBUTIONS OF THE NUMBER OF MINIMUM IONIZING PARTICLES. (LAYERS 9 AND 10)

this binning procedure, these distributions are strongly correlated. The width of the distributions is indicative of the large fluctuations in ionization which are characteristic of shower development. The largest fluctuations are in the first two layers. The best shaped distributions are at a depth of 200 to 400 gm/cm^2 into the calorimeter, in the area of maximum average calorimeter shower development. The results of ionization bursts in the scintillators are inseparably tangled with fluctuations in the nuclear-electromagnetic cascade. The events in the zero equivalent muons bin in the first few layers are hadrons which did not interact until they penetrated deeper into the calorimeter. After layers three and four most of the incident hadrons had initiated a cascade and the peak of the distribution shifts toward the left because most of the energy of events which interact at a shallower depth in the calorimeter was already absorbed.

A comparison can be made between the energy calculated from a ten layer calorimeter and an energy determined from ionization in a single layer. The difference in the energy calculated in these two ways is

$$\Delta E = E - KN \quad .$$

The term E, is the calculated energy from a ten layer calorimeter and N is the number of equivalent muons in one of the scintillator layers. The constant K, simply converts the ionization in a single scintillator at some depth into energy. The fluctuations in the energy resolution of single events assuming that the calculated energy of the ten layer calorimeter is correct is

$$\frac{\Delta E}{E} = 1 - K(N/E) \quad .$$

Distributions of the term N/E, for various energy bins are shown in Fig. 26. It is clear from this figure that although the distributions are rather broad, the peak is fairly well defined. An indication of how these distributions vary with depth in the calorimeter is shown in Fig. 27. The optimum thickness of absorber above the scintillator in a one layer calorimeter is two to three interaction lengths.

In each energy bin, the function

$$N(z) = KE(z - z_o)^P \exp(-(z - z_o)/\Lambda_S)$$

was fit to the average number of equivalent muons at each calorimeter layer. The parameters K, z_o, P and Λ_S were determined by a least squares fit. Figure 28 shows the data points as +'s and x's and a series of curves representing the fit functions of the various energy bins. The parameter z_o, was necessary to accommodate the fast rise and sharp peak of the data. The Λ_S, which controls the decay of the showers at large depths, is a function of energy and becomes larger for higher energies. The maximum of the shower curve at $z = P\Lambda_S$ does not seem to move appreciably and changes in Λ_S are balanced by changes in P. The average ionization sampled at each layer is a superposition of showers from many events, some of which travel some distance in the iron before interacting for the first time. The parameterization $N(z)$, is therefore not exactly representative of the average shower starting from the interaction point. The average shower parameters will be discussed more completely in a following section.

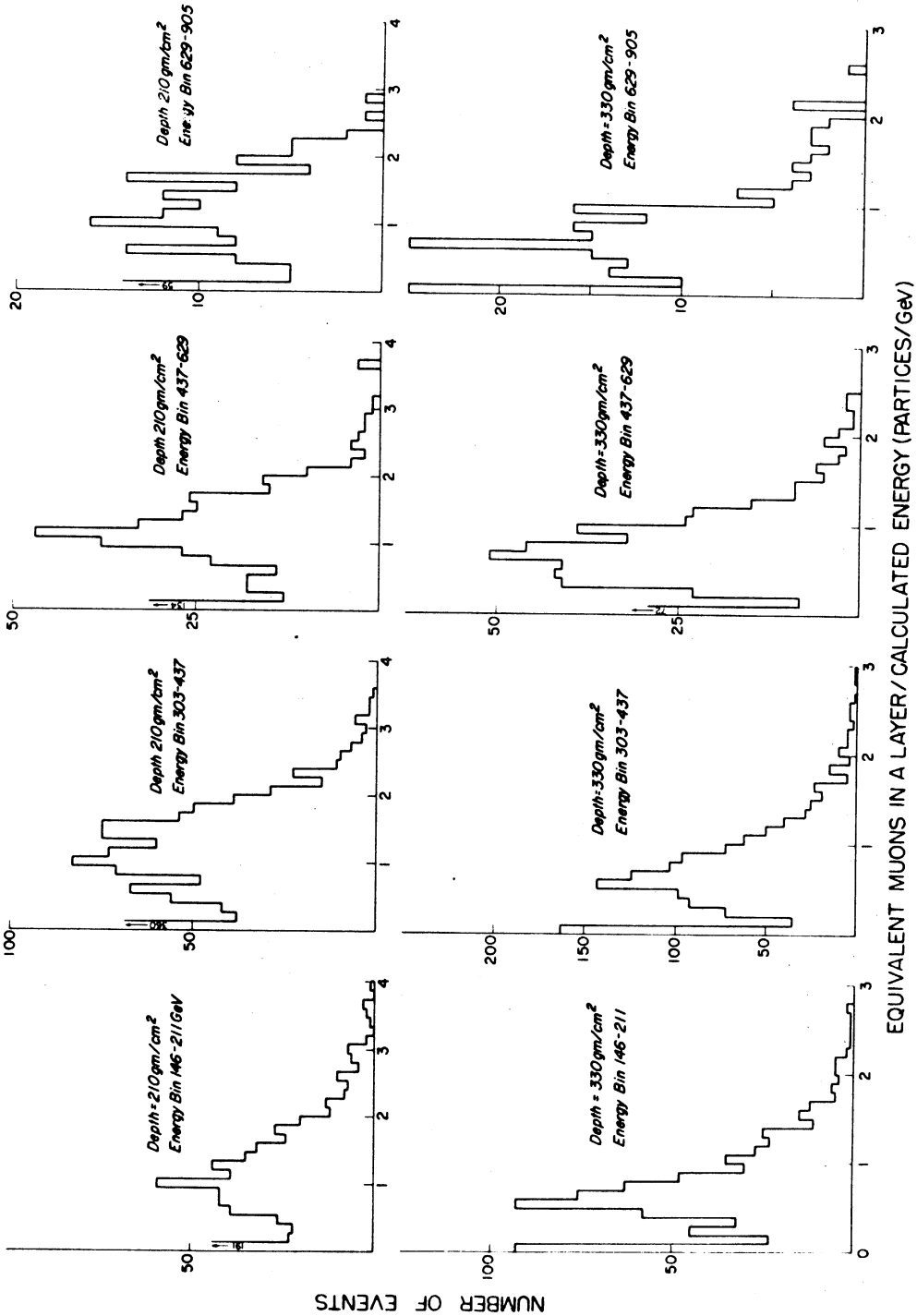

FIG. 26 COMPARISON OF IONIZATION IN A SINGLE LAYER TO THE CALCULATED TOTAL ENERGY.

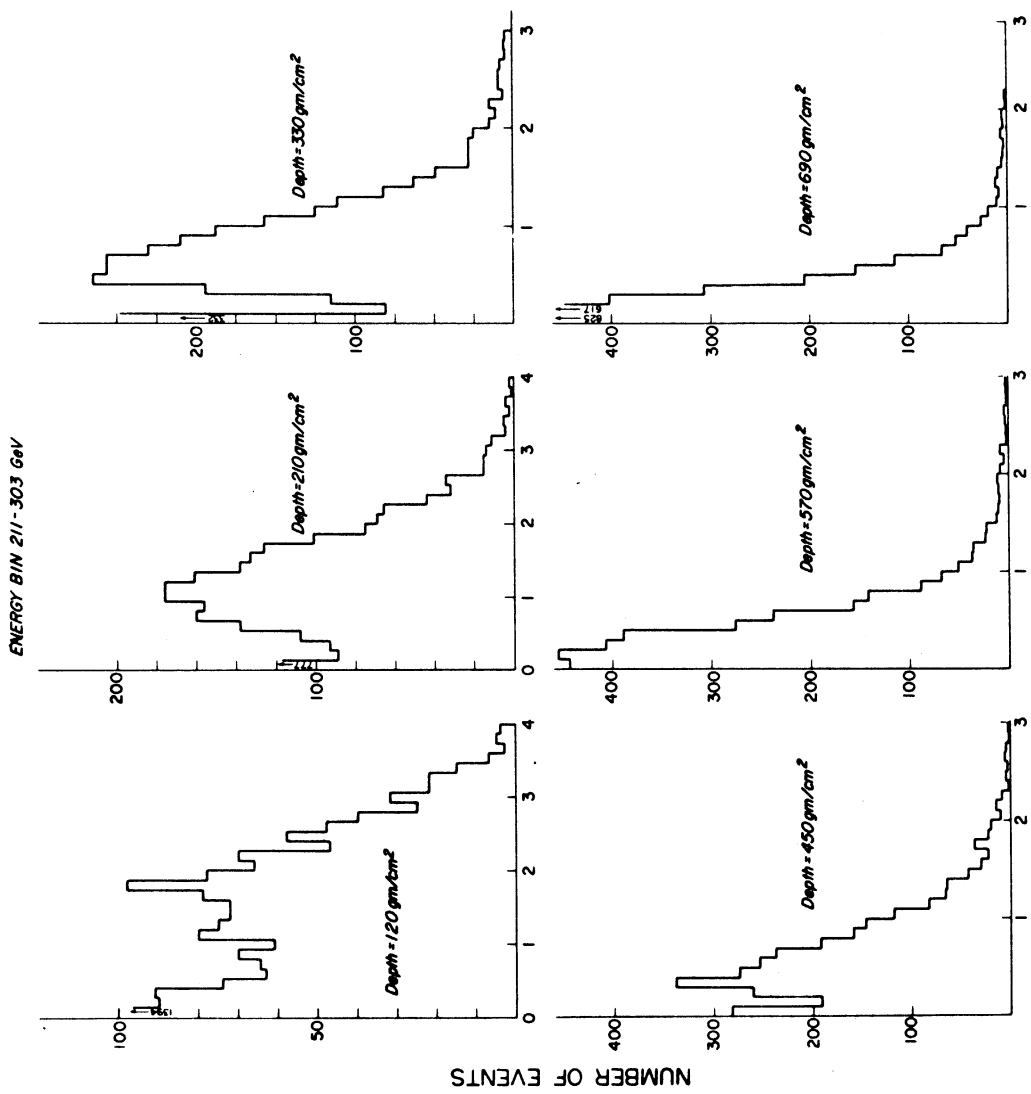

FIG. 27 COMPARISON OF IONIZATION IN A LAYER AT VARIOUS DEPTHS TO THE CALCULATED ENERGY.

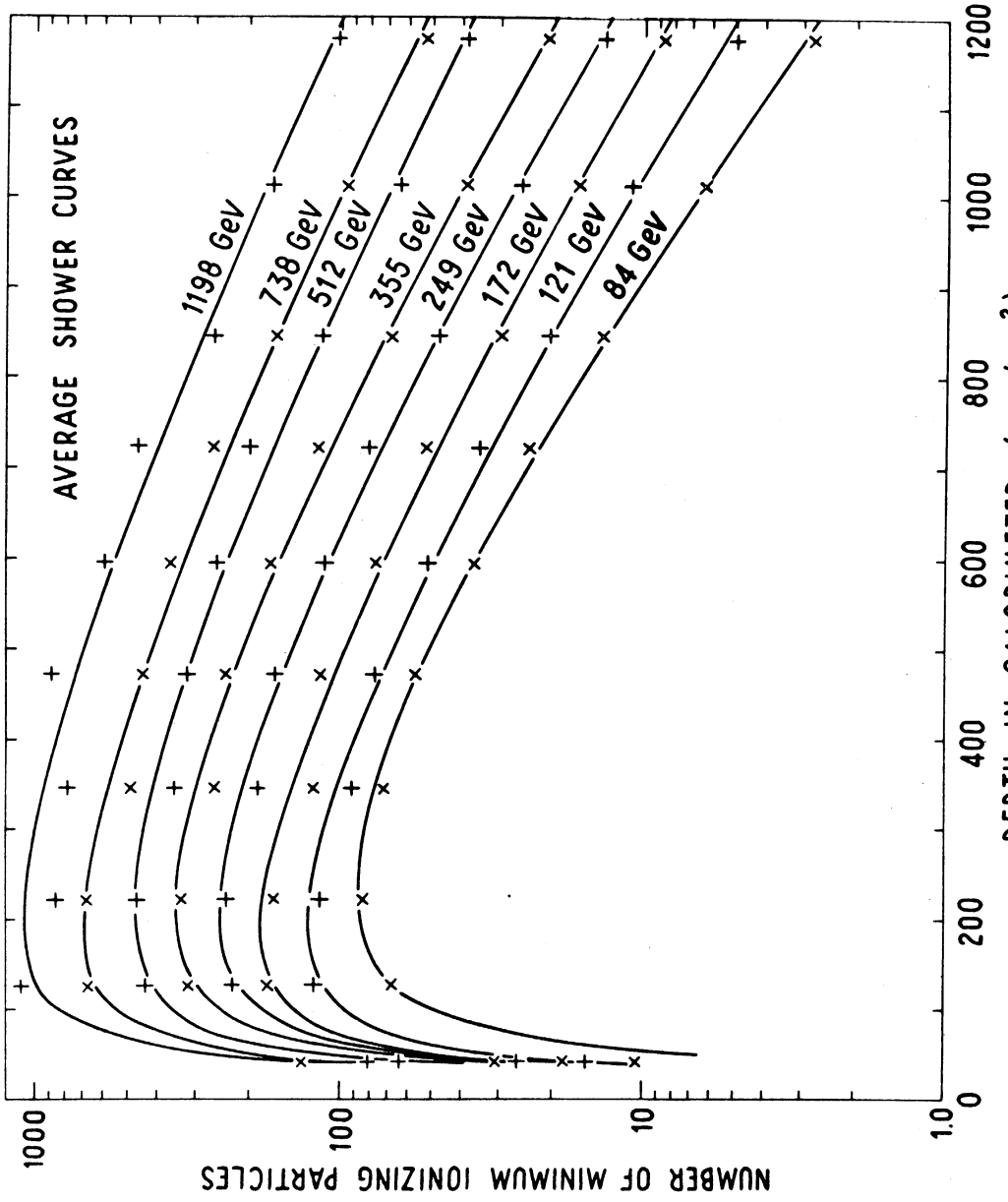

FIG. 28 AVERAGE SHOWER CURVES OF EVENTS WITH THEIR FIRST INTERACTION DISTRIBUTED IN THE CALORIMETER.

Dr. W. V. Jones [1] used his Monte Carlo program to calculate the mean and standard deviation of the number of electrons at the depth of each of the scintaillator layers in this calorimeter. Also included in his calculations were the fraction of energy going into nuclear disintegrations in each layer and the energy escaping laterally from each layer. In order to make a comparison between these results and experimental results the number of electrons in each layer n_{ej}, was converted into equivalent muons $n_{\mu j}$, and half of the nuclear disintegration energy was included with a transition effect f_j,

$$n_{\mu j} = 1.126\, n_{ej} + \frac{f_j}{2} \frac{E_{NT}(j)}{\beta_c w_j} \quad .$$

This notation is the same as that defined in Chapter III, Section D. The agreement between Monte Carlo and experimental results is shown in Fig. 29. There are two differences between the results shown. First, the ideal calorimeter, modeled by the Monte Carlo program, was of pure iron and the number of particles calculated was electrons at a particular depth. However, the calorimeter at Echo Lake was made with plastic scintillators of finite thickness in which the path length of ionizing particles was increased by a factor sec θ, where θ is the zenith angle of the tracks. Second, the Monte Carlo results were determined by generating events of a specific energy and observing shower development , whereas the experimental results are from binning a spectrum of energies.

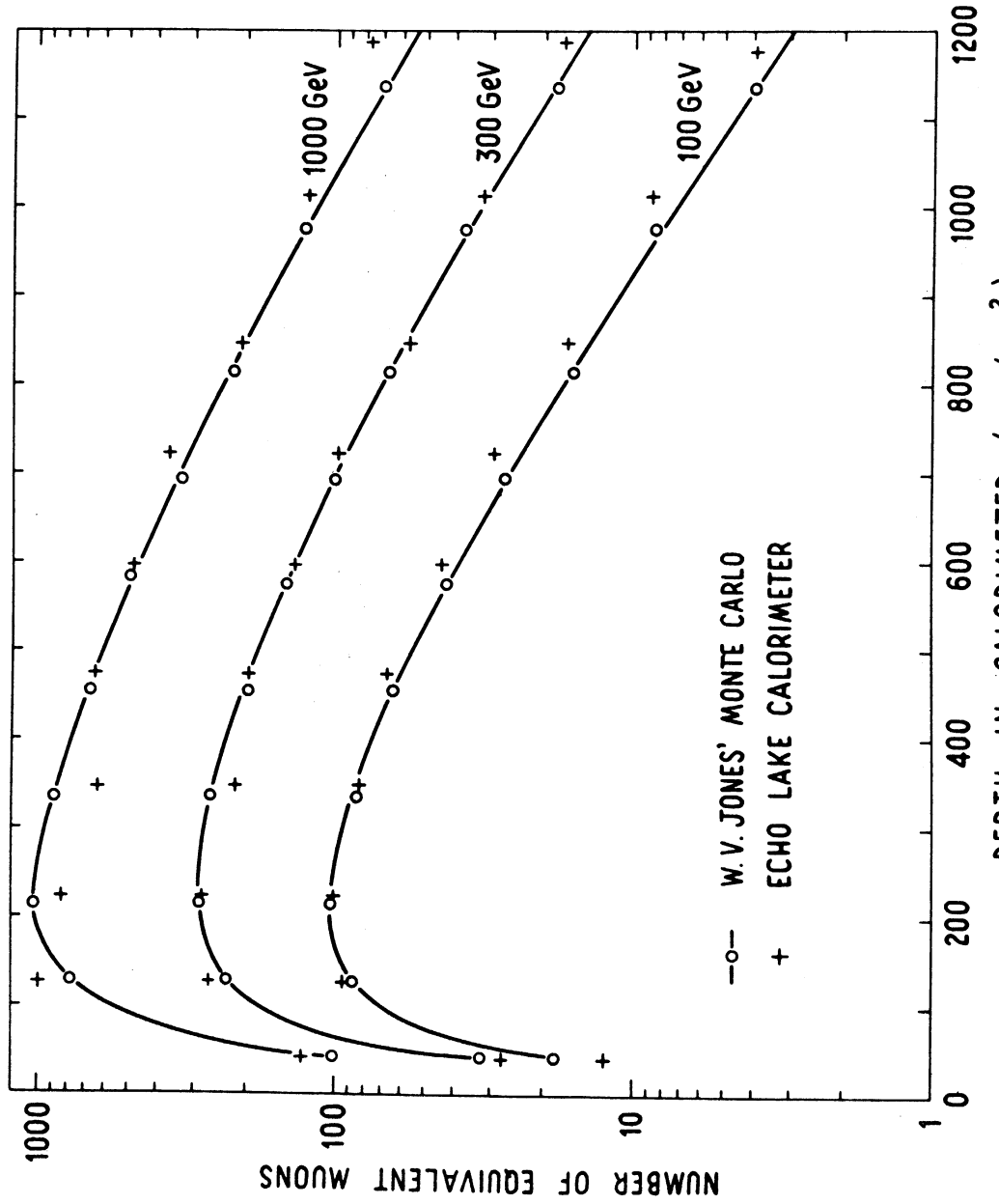

FIG. 29 COMPARISON OF THE AVERAGE SHOWER CURVES WITH THE MONTE CARLO RESULTS OF W. V. JONES.

The calorimeter calculations of Dr. Jones include a standard deviation as well as a mean for the weighted sum over the layers of the calorimeter. The ratio of these two quantities σ/μ, which is the resolution of the calorimeter is about 0.15 at 100 GeV and 0.08 at 1000 GeV. The energy resolution for large calorimeters was also estimated by Ramana Murthy et al. [36] for energies less than 100 GeV by comparing the calculated energy with the energy measurement of a Cherenkov counter. The result was an energy resolution of ± 20 percent for his calorimeter. The widths of the energy bins, into which events were sorted, are ± 20 percent of the mid-energy of the bin. This width is larger than one standard deviation in the dispersion of measured energy about the true energy of the event.

The events which both entered the calorimeter with more than twice the threshold energy for triggering and remained within the fiducial volume, were used to determine the differential energy spectrum of observed hadrons, D(E). The data was used in a maximum-likelihood fit to determine the power of the energy, E in GeV, for the equation

$$D(E) = 6 \times 10^{-3} E^{-(3.0 \pm 0.2)} \ (\mathrm{cm}^2 \ \mathrm{sr} \ \mathrm{sec})^{-1} \ .$$

Other experiments have determined this parameter to be 2.67 ± 0.05, for the primary hadron spectrum [32]. If hadrons in the accepted flux have already undergone an interaction in the atmosphere, the events with higher energy will, on the average, have more particles which are closer together than events of lower energy. This will result in the

shower counter array rejecting more of the higher energy events, and in so doing, make the slope of the spectrum steeper. This differential energy spectrum was determined from this experiment to an accuracy of $\pm$ 10 percent.

B. Proton-Iron Inelastic Cross Sections

The cosmic ray hadrons which had their first inelastic collision within the calorimeter were used to determine the proton-iron inelastic cross sections as a function of energy. The event selection criteria for this analysis were the same as the selction criteria for the calorimeter study with one additional constraint. This constraint, that the observed cascade in the calorimeter last a minimum of three calorimeter layers, eliminated most muon induced electromagnetic showers which triggered the system. The survival length in absorber of the selected events was then used to determine λ, the interaction length of hadrons in iron. The first scintillator layer after the interaction was taken to be the first layer with five or more equivalent muons.

The properly normalized probability that a particle will survive a thickness ℓ, of iron without interacting is

$$P(\ell,\lambda) = \frac{e^{-\ell/\lambda}}{\lambda} .$$

In this equation λ is the average distance in iron that the incident particle travels before it undergoes an inelastic collision. The

likelihood function of a series of independent events is the product of all the probability functions. The number of particles which survive a distance ℓ, into the iron is

$$N(\ell) = N_T e^{-\ell/\lambda} \quad .$$

The number N_T, is the total number of incident particles. The likelihood function, $\mathcal{L}$, for N_T particles each traversing a distance ℓ_{ik}, through k layers of the calorimeter is

$$\mathcal{L} = \prod_{i=1}^{N_T} \prod_{k=1}^{B-1} \frac{e^{-\ell_{ik}/\lambda}}{\lambda} \quad .$$

The distance the ith particle traveled in iron before it intersected the kth scintillator layer of the calorimeter is ℓ_{ik}. This distance includes a factor of sec θ to account for the zenith angle of the event. Each particle i, is in the product once for each layer of the calorimeter in which the particle has not yet interacted. The product over k then accounts for the fact that the number of particles $N(\ell)$, which do not interact in a distance ℓ_k, consists of all particles which survive a distance ℓ_k, or greater. The parameter λ, and the error in the parameter, $\delta\lambda$, are determined by the following equations:

$$\frac{\partial}{\partial\lambda} \ell n \mathcal{L} = 0$$

$$\delta\lambda = \left[- \frac{\partial^2}{\partial\lambda^2} (\ell n \mathcal{L}) \right]^{-1/2} \quad .$$

Explicitly these equations are:

$$\left[\sum_{i=1}^{N_T}\sum_{k=1}^{B-1} \ell_{ik}\right] \Big/ \left[\sum_{i=1}^{N_T}\sum_{k=1}^{B-1} 1\right] = \lambda$$

$$\delta\lambda = \left\{ \left[2\sum_{i=1}^{N_T}\sum_{k=1}^{B-1} \ell_{ik} - \lambda \sum_{i=1}^{N_T}\sum_{k=1}^{B-1} 1 \right] \Big/ \lambda^3 \right\}^{-1/2} .$$

The procedure used to calibrate the calorimeter in terms of equivalent muons made the various scintillators of the calorimeter equally sensitive to ionization. The layer position sensitivity, which made the region of scintillator close to the phototubes much more sensitive to ionization, was also corrected for. Therefore, the five or more equivalent muons, which were used to determine the first scintillator layer after an interaction, is a uniform criterion for interactions in all regions of the calorimeter. Events with increased ionization from δ-rays produced in the iron and from fluctuations in the ionization loss of the hadron in the scintillator are generally not counted as interactions because of this threshold criterion level. The parameter λ, is insensitive to the choice of threshold level. A noise level of either three or ten equivalent muons only changes the value of λ about 1 percent.

Muons interact within the calorimeter and simulate hadron events. The muons in the flux of hadron like events which do not

interact in the target were discussed in Chapter III, Section F. The muons result in two kinds of cascades within the calorimeter. Electromagnetic interactions of muons resulting in pair production cause relatively short cascades. Muon-photo-nuclear interactions should result in cascades exactly like those initiated by hadrons. The cascade in the calorimeter was required to persist a minimum of 240 gm/cm^2 of iron and, on the average, was required to persist 300 gm/cm^2. This requirement eliminates most of the muon induced electromagnetic showers which may trigger the calorimeter. The muon-photo-nuclear interactions occur equally likely at any depth of iron and constitute a small constant background of events which survive to any depth. Both hadron and muon events whose first interaction in the iron is deeper than layer six of the calorimeter are not used in the fit to determine interaction length. When an event occurs after layer six, the hadron coincidence trigger samples ionization from only three layers. Because of layer by layer fluctuations in the observed ionization, these events do not always trigger the system. Therefore, the maximum likelihood fit to interaction length λ, was terminated at layer six. This cutoff eliminates further consideration of muon-photo-nuclear interactions.

The results of the analysis of the survival lengths of hadrons in iron are plotted in Fig. 30 and listed in Table VI. Also shown in Fig. 30 are two empirical equations that were fit to the maximum likelihood parameter λ, determined for seven energy intervals. These two equations are

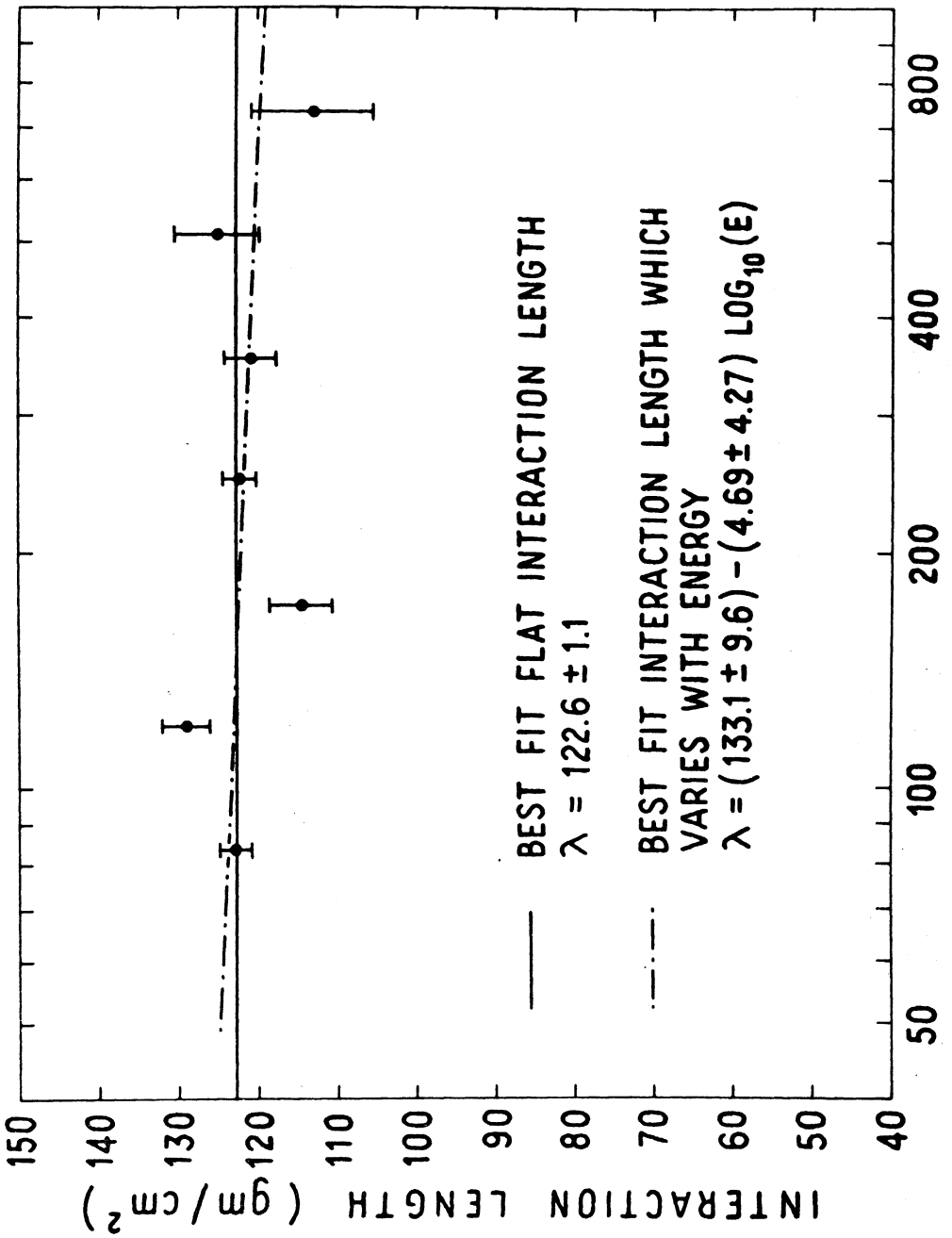

FIG. 30 RESULTS OF THE MAXIMUM LIKELIHOOD FIT TO THE PROTON-IRON INTERACTION LENGTH.

Table VI

Results of Maximum Likelihood Fit to Iron Interaction Length

Energy (GeV)	Number of Events	Interaction Length (gm/cm^2)	Error in Interaction Length (gm/cm^2)
84	2198	122.92	2.07
121	1255	129.02	2.98
172	583	114.47	3.98
249	2375	122.29	2.14
355	1017	120.80	3.29
512	427	125.09	5.28
738	179	113.02	7.71

$$\lambda(E) = 122.6 \pm 1.1 \quad gm/cm^2$$

and

$$\lambda(E) = (133.1 \pm 9.6) - (4.6 \pm 4.27) \log_{10}(E) \quad gm/cm^2 .$$

The energy E, in this second equation is in GeV. These data are consistent with a constant cross section over the energy range from 70 to 900 GeV. The constant inelastic cross section calculated for the constant interaction length is

$$\sigma_{hFe}(E) = 756.3 \pm 7.0 \quad mb .$$

The incident hadron flux for which the interaction length was determined consisted of both pions and protons. The correction to the observed cross section due to pions was calculated from a pion to proton ratio of 0.3 and the ratio of pion-iron to proton-iron cross sections. The ratio of the pion-iron to the proton-iron inelastic cross sections were determined from accelerator measurements and used to find the inelastic proton-iron cross section from the observed interaction length. As an alternative way of determining this correction the optical model calculations of P. Sievers [37] were also used to calculate the pion-iron and proton-iron total cross sections. Here the nucleus is represented by a radius and a mean free path of the incident hadron in the nuclear material x_o. The difference between the pion-iron and proton-iron cross section can be found by associating with each a characteristic x_o leaving the radius of the nucleus the same.

P. Sievers developed his model by assuming a constant opacity and a nucleus with an absorption probability that depends on the amount of

nuclear matter traversed. The optical thickness of the nucleus a(b), in an impact parameter representation is

$$a(b) = 1 - \exp\left(\frac{-2\sqrt{R^2 - b^2}}{x_o}\right) ,$$

where $R_{PN} = r_P A^{1/3}$ and A is the atomic weight of the nucleus. The two parameters in his model are x_o, the nucleon mean free path in nuclear matter, and r_p, the radius of the nucleons. The amount of nuclear matter presented to the incident pions and protons for most impact parameters is large compared to their mean free path in nuclear material. Therefore, the difference between the proton-iron and pion-iron cross sections is due to large impact parameter events where the collision occurs near the periphery of the nucleus. The scattering amplitude for this model was approximated by the expression

$$f(\theta) = ik \int_0^R b\, a(b)\, J_o(kb\theta)\, db .$$

This equation, combined with the optical theorem, results in a total cross section

$$\sigma_T = 2\pi \{R^2 - 2[1 - (qR + 1)e^{-qR}]/q^2\} .$$

where $q = 2/x_o$. There is good agreement between predicted and experimental values of the proton-nucleus total cross section when $x_o = 3f$ and $r_p = 1.27$ f. [38].

The optical radius R_1 used in this model was the effective radius of the target nucleus when the incident particle has no dimensions.

In order to calculate a pion-iron total cross section the mean free path of the pion in nuclear material, x_o = 5.35 f, was chosen holding R constant such that the pion-proton total cross section predicted by the model was 27.02 mb. The ratio of the pion-iron and proton-iron total cross sections calculated with this x_o was

$$D = \frac{\sigma_{\pi Fe}}{\sigma_{pFe}} = 0.798 \quad .$$

Using the pion to proton ratio of the flux, (which was discussed in Chapter III, Section F,) F = 0.3, the proton-iron cross section is expressed in terms of the observed cross section σ_{hFe}, by the equation

$$\sigma_{hFe} = \frac{1 + F}{1 + FD} \sigma_{hFe}$$

$$\sigma_{pFe} = 1.049 \, \sigma_{hFe} = 793.3 \pm 7.4 \text{ mb} \quad .$$

The pion-nucleus and proton-nucleus cross sections measured in accelerator experiments yield a somewhat different ratio F. The pion-iron and proton-iron inelastic cross sections were both calculated by interpolating between the reported aluminum and copper cross sections. The pion-nucleus inelastic cross sections were reported by J. V. Allaby et al. [39] at 40 GeV/c. The proton-iron cross section was determined in a less direct procedure using the neutron nucleus results of J. Engler et al. [17] at 21 GeV/c. It was assumed that the proton-nucleus and neutron-nucleus total cross sections were the same. The aluminum and copper total cross sections were multiplied by the ratio of inelastic to total cross section reported by G. Bellettini et al. [16] and the

results interpolated to give a neutron-iron inelastic cross section. The ratio of the calculated inelastic cross sections was

$$D = \frac{\sigma_{\pi Fe}}{\sigma_{pFe}} = \frac{554 \text{ mb}}{727 \text{ mb}} = 0.762 \quad .$$

The corrected proton-iron cross section is then

$$\sigma_{pFe} = 1.058\, \sigma_{hFe} = 800.2 \pm 7.4 \text{ mb} \quad .$$

Thus the pions in the flux result in a 5 to 6 percent correction to the observed hadron-iron cross section to convert it into a proton-iron cross section. The correction based on accelerator measurements is probably most nearly correct.

The proton-iron inelastic cross section reported here is identical to the inelastic cross section which may be calculated from the proton-nculeus cross sections reported by G. Bellettini et al. [16], at 20 GeV/c. The proton-iron cross section calculated by interpolating between the measured aluminum and copper absorption cross sections is

$$\sigma_{pFe} = 800 \pm 50 \text{ mb} \quad .$$

The neutron-nucleus total cross sections reported by J. Engler et al. [17] are somewhat different from this. A proton-iron cross section calculated from Engler's measurements was given in Chapter I, Section D as

$$\sigma_{pFe} = 727 \pm 50 \text{ mb} \quad .$$

E. L. Andronikashvili et al. [20] have also measured a hadron-iron cross section using a calorimeter and the cosmic ray hadron flux.

However, they did not correct their results for the fraction of pions in the "beam." Their hadron-iron cross section was

$$\sigma_{hFe} = 710 \pm 35 \text{ mb} .$$

This result is somewhat lower but is consistent with the uncorrected hadron-iron cross section reported here. Some of the difference may be associated with the different kinds of detectors used in the calorimeter and a somewhat different pion to proton ratio. However, both experiments are consistent with a flat cross section over the energy range from 50 to 1000 GeV.

The interaction length λ, is somewhat dependent both on the number of calorimeter layers which are included in the maximum likelihood fit and on the parameter Λ, in the energy calculation which is used to correct for the amount of energy which leaves the calorimeter, C(L). It is evident from Fig. 32 that the shower decay parameter Λ, is energy dependent. The value of $\Lambda(E)$ used, 240 gm/cm^2, is correct for a 300 GeV hadron shower. Typically, for a 730 GeV event which interacts near layer six, about halfway through the calorimeter, the correction C(L), amounts to 15 percent of the energy of the event. Because this correction is so small, on the average, the number of events in an energy bin is insensitive to the choice of $\Lambda(E)$. Changing Λ to 200 or 300 gm/cm^2 results in a change of about 1 percent in the fit interaction length. The change is less when the shower decay parameter $\Lambda(E)$, is diminished. The calculated interaction length for the energy

bins is more dependent on the depth in the calorimeter at which the maximum likelihood fit is terminated. If λ is fit using information from only the first four layers of the calorimeter, the resultant proton-iron inelastic cross section is considerably flatter and about 820 ± 7 mb. Therefore, there is a possible systematic error of about 7 percent in the cross section results. There seems to be no justification for not using layers five and six in the fit. Rather, these layers add to the information determining the interaction length.

C. Monte Carlo Corrections

Because of the method used to determine the proton-proton inelastic cross section, a small systematic energy underestimate of target interacting events relative to the energy of non-interacting events will result in a large decrease in the calculated cross section. This extreme sensitivity to energy biases is a result of the binning of events from the energy spectrum of incident hadrons, $\propto E^{-3}$, discussed in Section A of this chapter. The effect on the measured cross section caused by an energy bias is discussed in detail in Appendix B. This sensitivity of results to small systematic energy biases motivated further study of the calorimeter and a Monte Carlo program. Biases resulting from the following three effects were studied.

1. The secondaries and the nuclear-electromagnetic cascades of events which interact in the target do not always remain within the volume of the calorimeter. Secondaries from an interaction may miss or leave the side of the calorimeter. Also the observed cascades of

the secondary particles may be truncated if the shower exits from the calorimeter.

2. The lateral spread of secondaries from target interactions results in uncertainty in corrections to the observed ionization necessitated by the nonuniform scintillator response. The individual layer ionization corrections were calculated using the extrapolated incident track and the formula discussed in Chapter II, Section C. The radius of the calorimeter shower about this exptrapolated track is greater when the first interaction occurs above the calorimeter and may result in a systematic energy bias.

3. The measured energy of an event may depend on the position of the first interaction relative to the scintillators in the calorimeter. The events which did not interact in the target had a distributed first interaction position in the calorimeter, whereas the interactions in the hydrogen all occurred about 5 ± 3 gm/cm^2 above the top of the calorimeter.

The same events that were used in the calorimeter studies of the previous sections were also used to study the effect of the position of the first interaction on the measured énergy. A total of 1,338 events from the energy bin between 211 and 303 GeV were grouped according to the first gap of the iron plate spark chamber in which significant ionization was observed. The results are shown in Fig. 31. There is no preference within this energy bin to select events because they interact at some optimum position for energy

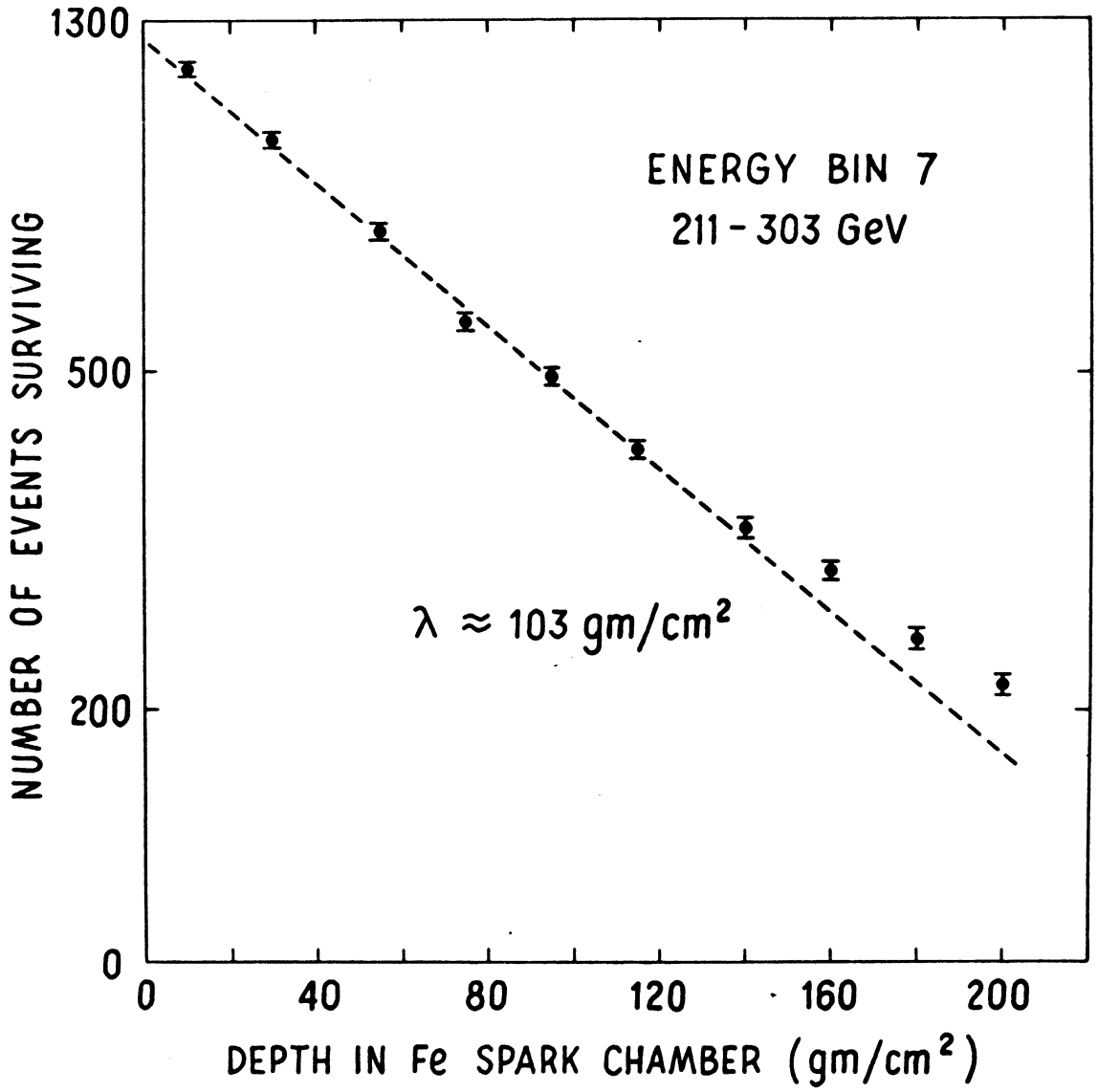

FIG. 31 DISTRIBUTION OF THE SURVIVAL LENGTH OF EVENTS WITH THEIR FIRST INTERACTION IN THE IRON-PLATE SPARK CHAMBER.

measurement. If there were, the line indicated in Fig. 31 would not be continuous at the positions of the scintillators. These scintillators are between the second and third gap and the sixth and seventh gap. The number of events interacting at some position and appearing in this energy interval is determined only by the proton-iron cross section. The proton-iron interaction length determined from the line in Fig. 31 is 103 gm/ cm^2. This measurement is not as accurate as the results discussed in the preceding section for several reasons. The procedure of determining the first interaction position by scanning is not as reliable as using the scintillator layers that were calibrated with muons. The scanning method is dependent upon consistent spark chamber efficiency and good resolution of closely grouped secondaries. Neither of these qualities was achieved in the iron plate spark chambers. Furthermore, the path length of surviving hadrons was not used. Instead, the vertical thickness of iron from the top of the calorimeter was used to calculate the interaction length.

The Monte Carlo program used to investigate energy biases consisted of a method of generating proton-proton interactions and a scheme for generating the calorimeter showers resulting from the secondaries of the interaction. The method used to generate the proton-proton interactions has been discussed briefly in a paper reporting the angular distributions of the secondaries of interacting events [30]. The method of generating the calorimeter showers is of more concern here. Table VII illustrates the average effects of the energy measurement of a 600 GeV interaction, comparing it with the shower development of just one incident hadron. The event which interacts in the hydrogen

Table VII

Comparison of the Measured Energy of an Event Which Interacts in the Target with One Which Does Not.

	Non-Interacting Event	Interacting Event			
	p^+	π^o	π^+	π^-	p^+
Energy of Particle	600 GeV	100 GeV	100 GeV	100 GeV	300 GeV
Fraction of Energy Not Seen	0.118	0.0	0.154	0.154	0.127
Energy Measured by Calorimeter	529 GeV	100 GeV	84 GeV	84 GeV	262 GeV
Energy Measured for Event	529 GeV			530 GeV	

has an inelasticity of 0.5 and produces three pions; 2/3 charged and 1/3 neutral. The neutral pions were assumed to produce an electromagnetic cascade. The energy of the charged secondaries was adjusted so that a fraction of this energy, taken from the curve in Fig. 18, was not observed. Energy of the recoil proton was ignored. The measured energy in the calorimeter is the same for the interacting event and the single charged hadron.

The calorimeter cascades generated by the Monte Carlo program were not concerned with the details of the cascade but developed an average shower similar to those exemplified in Fig. 32. These calorimeter curves differ from the average curves of Section A of this chapter. Previously the ordinate began at the top of the calorimeter and indicated average ionization in each of the ten layers. In Fig. 32 the cascade begins at the average position of the first interaction in the thickness of iron between scintillator layers. The average position of the first interaction was calculated using an interaction length of 124 gm/cm^2. It was further assumed that all information concerning the observed fluctuations was contained in the average shower curve. The generated shower curves were

$$N(\ell) = Kt^{0.7} e^{-t/\Lambda_S} ,$$

where

$$t = \ell - 20 \quad \text{gm/cm}^2$$

and

$$\Lambda_S(E) = 28.24 \log_e E + 32.94 .$$

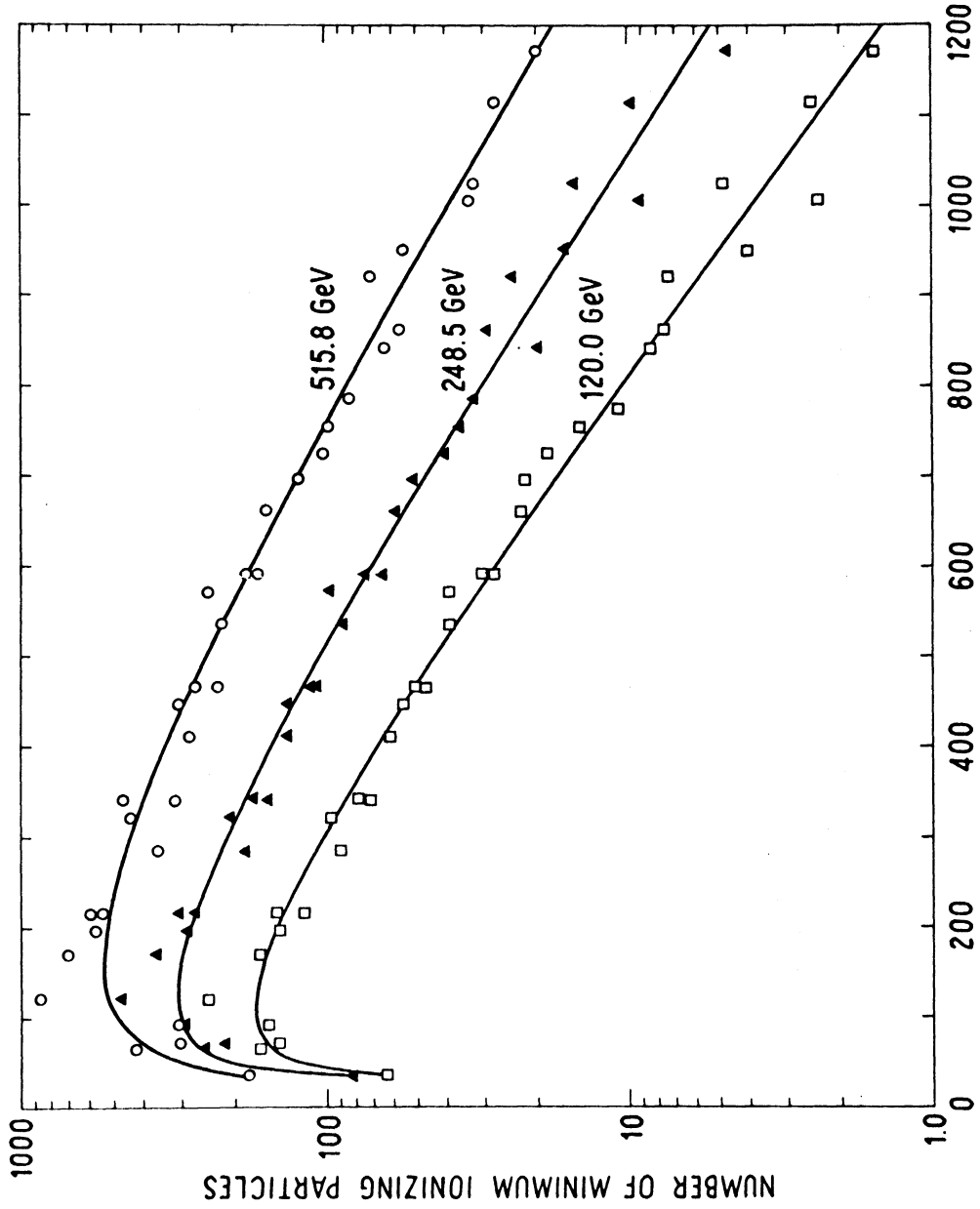

FIG. 32 AVERAGE SHOWER CURVES WITH ORIGIN OF EVENTS SHIFTED TO THE AVERAGE POSITION OF THE FIRST INTERACTION IN THE CALORIMETER LAYER WHERE THE FIRST INTERACTION OCCURRED.

The constant K, was chosen to normalize the area under the shower curve so that

$$E = \int_{\ell=20}^{\infty} KN(\ell)\, d\ell$$

The calorimeter cascades caused by the neutral pions produced in the first interaction were generated as if they were cascades produced by single electrons. The electromagnetic shower curves of Snyder and Serber given by Rossi [31] were approximated by the function

$$N'(\ell) = K_E\, t^{\alpha}\, e^{-t/\Lambda_S} ,$$

where

$$\alpha(E) = 0.29 \log_e(E/\varepsilon_o) + 1.638 ,$$

and

$$\Lambda_S(E) = 0.814 \log_e(E/\varepsilon_o) + 15.174 \text{ gm/cm}^2 ,$$

$$t = \ell - 6.5 \text{ gm/cm}^2 .$$

The constant K_E, was chosen so that the area under the shower curve was the energy.

$$E = \int_{\ell=6.5}^{\infty} K_E\, N'(\ell)\, d\ell .$$

The number of observed equivalent muons in a layer of the calorimeter was the sum of ionization from all cascades which traversed the layer. The ionization of each cascade observed in a layer at a

depth ℓ, along the path of the shower was adjusted by

$$1.0/[1.0 - 3.7013 \cdot 10^{-5} \cdot x^2]$$

for the scintillator response, by the appropriate transition effect, and by a factor of sec θ for the path length in the scintillator. After adding the ionization from all secondary showers traversing the layers, the energy was calculated exactly as if the event was an experimentally observed event.

Events were generated with an energy spectrum of E^{-3}. The energy determination of events which interacted in the liquid hydrogen has been described. The energy of events which underwent their first interaction in the calorimeter was calculated by generating the first interaction exactly as if it were a proton-proton collision. The interaction vertex of these events occurred at a distance S into the calorimeter which was distributed as $e^{-S/124}$. The event flux in energy bins corresponding to the experimental energy bins was observed to determine the correction to the cross section, necessary because the calorimeter, on the average, systematically measured a different energy for interacting and non-interacting events. The corrections to the cross sections were calculated from the relative rate of interacting and non-interacting events in an energy bin. These Monte Carlo corrections are shown in Fig. 33. The lowest energy corrections are not as reliable as the others since the program did not exactly duplicate the behavior of the trigger. The Monte Carlo results also include two other small corrections. There is a correction for four percent of the interactions that were two-prong events but appeared

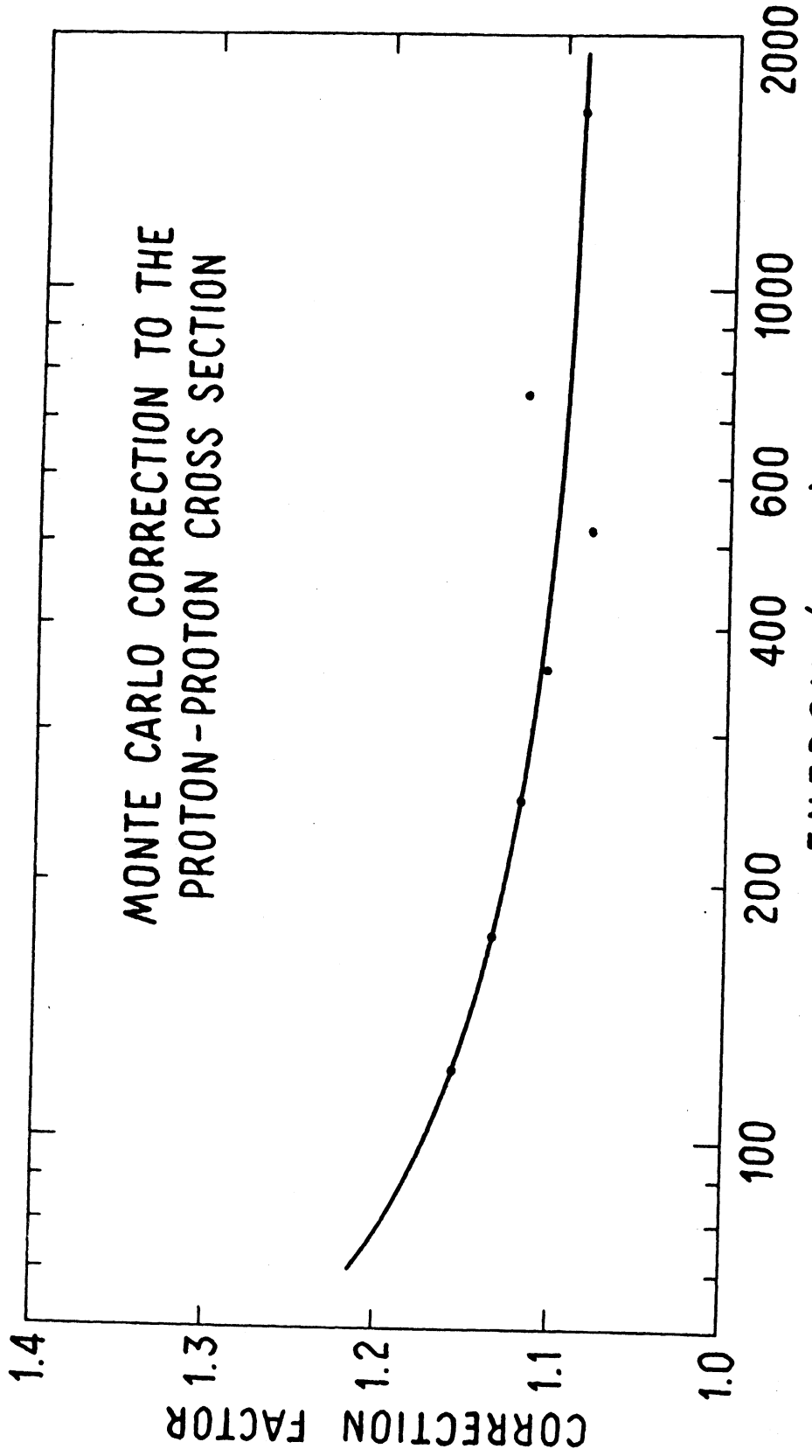

FIG. 33 RESULTS OF THE MONTE CARLO ANALYSIS.

as non-interacting one-prong events. There is also a small correction for the charged pion secondaries of the first interaction which decay into muons before developing a cascade in the calorimeter. This is much less than 1 percent.

D. Proton-Proton Inelastic Cross Sections

The proton-proton inelastic cross section was calculated using a thin target approximation and a corrected number of scanned events. The procedure was discussed in Chapter III, Section D. Corrections to the scanned number of interacting and non-interacting events were discussed in preceding sections along with the corrections to the observed cross section. In this section the numbers of events and the appropriate corrections are presented and used to calculate cross sections. Cross sections were calculated from the scanned number of events adjusted so that the same fraction of scanned events and reconstructed events satisfied the selection requirements. These event selection criteria were discussed in Chapter III, Section D. Table VIII shows, for both interacting and non-interacting events, the number of reconstructed events and the reduced number of events meeting the fiducial volume, z-vertex, and energy requirements.

The validity of this procedure for determining the number of scanned events which satisfied the same criteria was checked by rescanning the events which failed reconstruction. All but 5.5 percent of the events which interacted in the target were reconstructed. The remaining events were not reconstructed as a result of measuring errors. Reconstruction failure was not correlated with multiplicity, energy, or event type. This small fraction of events was distributed over all energy bins

Table VIII

Summary of the Effects of the Event Selection Requirements on the Number of Reconstructed Events. The Numbers of Interactions in This Table Pertain Only to Events with Three or More Observed Secondaries

Interacting Events

	Number of Events	Fraction of Total Remaining
Number of events	2228	
Number remaining after geometry cut	1420	0.64
Number remaining with interaction vertex in liquid hydrogen	806	0.36
Number of events in useful energy bins	382	0.17

Non-Interacting Events

Number of events	50,000	
Number remaining after geometry cut	30,766	0.62
Number remaining in useful energy bins	8,004	0.16

as 5.5 percent of the number of events already in each bin. Events which apparently did not interact in the target and were not reconstructed were distributed over the energy bins in a similar way. Only 77 percent of the non-interacting events were reconstructed and the remaining 23 percent were distributed over all energy bins. Some events were not measured and some measurements were discarded due to magnetic tape recording problems and event number mismeasurement in one of the two stereo views. However, 12.4 percent of the events which were measured failed to reconstruct. Of these failed events, 73.6 percent were caused by poor fiducial measurements by the MASS system. Most of the other reconstruction failures were due to intensity and resolution difference between the periphery of the MASS scanning field and the center. Some of the events were definitely bad events reflecting a difference between the scanning criteria for interacting and non-interacting events. This prompted a rescan of 10 percent of the film. An average of 3 percent of the events which were grouped as "good" events which did not interact in the target should not have been counted if the scanning criteria had been identical between interacting and non-interacting events.

Further corrections to the scanned number of events which met the selection criteria were discussed in the last two sections of the previous chapter. The scanned number of "good" events is shown for two triggering threshold categories in Table IX along with the subsequent corrections to this number. The correction for a 5 percent muon simulation of non-interacting hadron events and the 3 percent overcount are lumped together in the first 8 percent correction. The number of

Table IX

Summary of the Counting of Events Which Did Not Interact in the Target. Both the Size of the Correction and the Number of Events After the Correction Are Shown.

	36 GeV Threshold		36 and 90 GeV Threshold	
	Correction	Number of Events	Correction	Number of Events
Scanned number of events		21,343		65,884
Fraction which satisfies the geometrical requirements	0.53819	11,508	0.61532	40,540
Correction for muons and scanning	1/1.08	10,655	1/1.08	37,537
Additional number of events which traversed the hydrogen and interacted in the lower dome of the target	+ 407 events	11,062	+ 1,080 events	38,617
Final number of events to be distributed over energy bins		11,062		38,617

interactions within the fiducial volume which apparently traversed the hydrogen and interacted in the lower stainless steel dome or lower aluminum jacket of the target was added to the observed non-interacting flux. Although the observed number of interactions that occur in the target walls may be as much as 50 percent low, as will be shown shortly, it amounts to less than 4 percent of the straight through flux. This error introduced into the cross section will make the result less than 2 percent too high.

Cross sections were calculated from the scanned number of events shown in Table IX. The number of events in the eight useful energy bins was calculated from the fraction of in geometry reconstructed events in each bin. These fractions are listed in Table X. The numbers of events which did not interact in the target and are distributed into the energy bins of Table X are the scanned numbers of events. The corrected numbers of interactions also listed in that table correspond to a scanned number of interactions including two prong interactions that were not eliminated as δ-rays. The cross section calculated from these numbers is labeled in Table XI as an "apparent cross section." These cross sections were calculated using the following formula introduced in Chapter III, Section D.

$$\sigma_{pp} = \frac{A}{N_o \ell_{av}} \log_e \left[1 - \frac{N_E}{N} \right] .$$

The average path length in hydrogen ℓ_{av}, was 3.34 gm/cm^2 for events from the 36 GeV threshold running and 3.87 gm/cm^2 for all events with

Table X

Summary of the Corrected Number of Events

Energy Bin (GeV)	Triggering Threshold (GeV)	Fraction of Non-Interacting Events In Each Energy Bin	Number of Events Which Did not Interact in the Target	Corrected Number of Interactions
71-102	36	0.204616	2263.5	87.86
102-146	36	0.117494	1300.0	55.05
146-211	36	0.055105	610.1	28.05
211-303	36 and 90	0.079912	3086.0	128.1
303-437	36 and 90	0.034501	1332.3	69.34
437-629	36 and 90	0.014220	549.13	21.17
629-905	36 and 90	0.006029	232.82	10.59
> 905	36 and 90	0.002490	96.16	4.23

Table XI

Summary of Corrections to the Measured Cross Sections.

Average Energy of Bin (GeV)	Apparent Cross Section (mb)	Cross Section with Correction for Pion flux (mb)	Cross Section with Monte Carlo Corrections (mb)
84	18.95	20.53 ± 2.15	24.43 ± 2.56
121	20.64	22.36 ± 2.95	26.51 ± 3.50
172	22.37	24.23 ± 4.13	27.48 ± 5.07
249	17.46	18.92 ± 1.64	21.10 ± 1.83
355	21.78	23.60 ± 2.76	26.15 ± 3.06
512	16.24	17.59 ± 3.75	19.35 ± 3.75
738	19.10	20.69 ± 6.22	22.66 ± 6.22
1198	18.48	20.02 ± 9.53	21.82 ± 9.53

energy greater than 211 GeV. The pions in the flux of incident hadrons was discussed in Chapter III, Section F. The correction for an admixture of pions does not make a large difference in the cross section and the size of the correction was assumed to be the same for all energies. At accelerator energies the pion cross section is about 2/3 of the proton cross section so a constant π/p ratio of 0.3 gives a correction to the observed cross section of 13/12. The cross section incorporating this correction for the pion flux is also listed in Table XI. Finally, the calculated cross section including the Monte Carlo corrections discussed in the previous section are listed in Table XI and displayed in Fig. 34. The indicated error in the cross section, $\delta\sigma$, represents statistical errors only and was calculated with the formula

$$\delta\sigma = \sigma \left[\frac{N - N_I}{N N_I} \right]^{1/2} .$$

Cross sections were also calculated using target empty information instead of the requirement that the vertex be at least 1 cm from the target walls. The number of observed interactions $N_I(H,W)$, is the sum of interactions in the walls $N_I(W)$, and in the hydrogen $N_I(H)$. The ratio of the number of interactions in the hydrogen to the total number of incident hadrons N_T, is

$$\frac{N_I(H)}{N_T} = \frac{N_I(H,W)}{N_T} - \frac{N_I(W)}{N_T} .$$

Since the flux of incident particles is much larger than the number of hydrogen interactions, the ratio of the wall interactions to the flux

hydrogen interactions, the ratio of the wall interactions to the flux

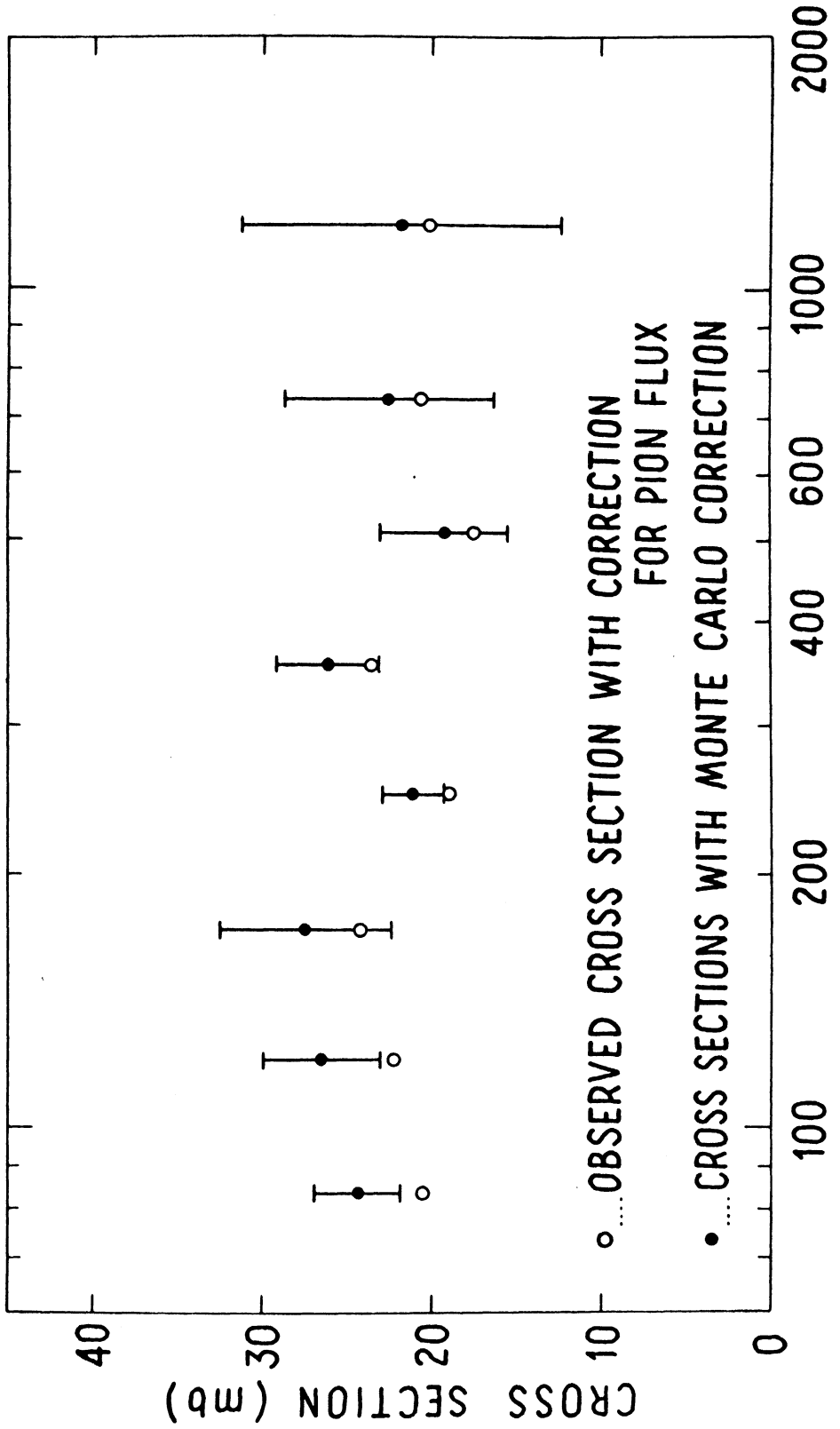

FIG. 34 PROTON-PROTON INELASTIC CROSS SECTIONS.

is approximately determined by the target empty ratio of interactions, $N_I(TE)$, to the flux, $N_T(TE)$.

$$\frac{N_I(W)}{N_T} \simeq \frac{N_I(TE)}{N_T(TE)} .$$

The cross section was calculated from the number of events with energy greater than 146 GeV, using the equation

$$\sigma_{pp} = \frac{A}{N_o \ell_{av}} \left[\frac{N_I(H,W)}{N_T} - \frac{N_I(TE)}{N_T(TE)}\right] .$$

This equation with the corrected numbers of events is

$$\sigma_{pp} = 429\text{mb} \left[\frac{789.2}{11823.6} - \frac{30.86}{1349.5}\right] .$$

This cross section, after applying a correction of 13/12 for the pion component of the flux, is 20.4 ± 3.6 mb. This result does not contain the Monte Carlo correction but requires the same correction as the proton-proton cross section previously calculated. It is in excellent agreement with the "cross section with correction for pion flux" listed in Table XI. This result shows that the requirement that a hydrogen interaction have a vertex at least 1.0 cm from the target walls determines the total number of hydrogen and the total number of target wall interactions correctly.

There is good experimental evidence that the cross sections listed in Table XI are low even after the Monte Carlo corrections. This information was obtained from an analysis of the number of interactions which occurred in the upper and lower domes of the target vessel. The

which occurred in the upper and lower domes of the target vessel. The

interactions that occurred both in the target walls and in the hydrogen were measured and reconstructed. The selection of events with a vertex in the hydrogen was made after reconstruction. The interactions which occurred in the aluminum and stainless steel of the target were subjected to the same energy and geometrical requirements as the hydrogen events. The remaining number of events is the result of event selection biases similar to those determining the number of hydrogen events. The observed number of proton-nucleus events was compared with the number of events expected to occur in the target walls. The expected number of events was based on the proton-iron inelastic cross section already discussed and on the assumption that the proton-aluminum cross section is also independent of energy. The proton-aluminum cross section was approximated by the neutron-aluminum total cross section measured by J. Engler et al. [17] at 20 GeV/c and adjusted to have the same ratio of inelastic to total cross section as those reported by G. Bellettini et al. [16]. The proton-aluminum cross section determined in this way is 444 mb. The probability that an incident hadron interacted in the aluminum and iron of the target walls was calculated using these cross sections. The number of wall interactions expected and observed is shown in Table XI . Not only are there too few observed interactions in the target walls, but there are 414 observed events in the lower dome with three or more charged tracks and only 209 in the upper dome. The number of hydrogen interactions with three or more charged secondaries is shown in Fig. 35. This data also shows some z dependence. This information indicates that the number of observed interactions is a function of the height above the

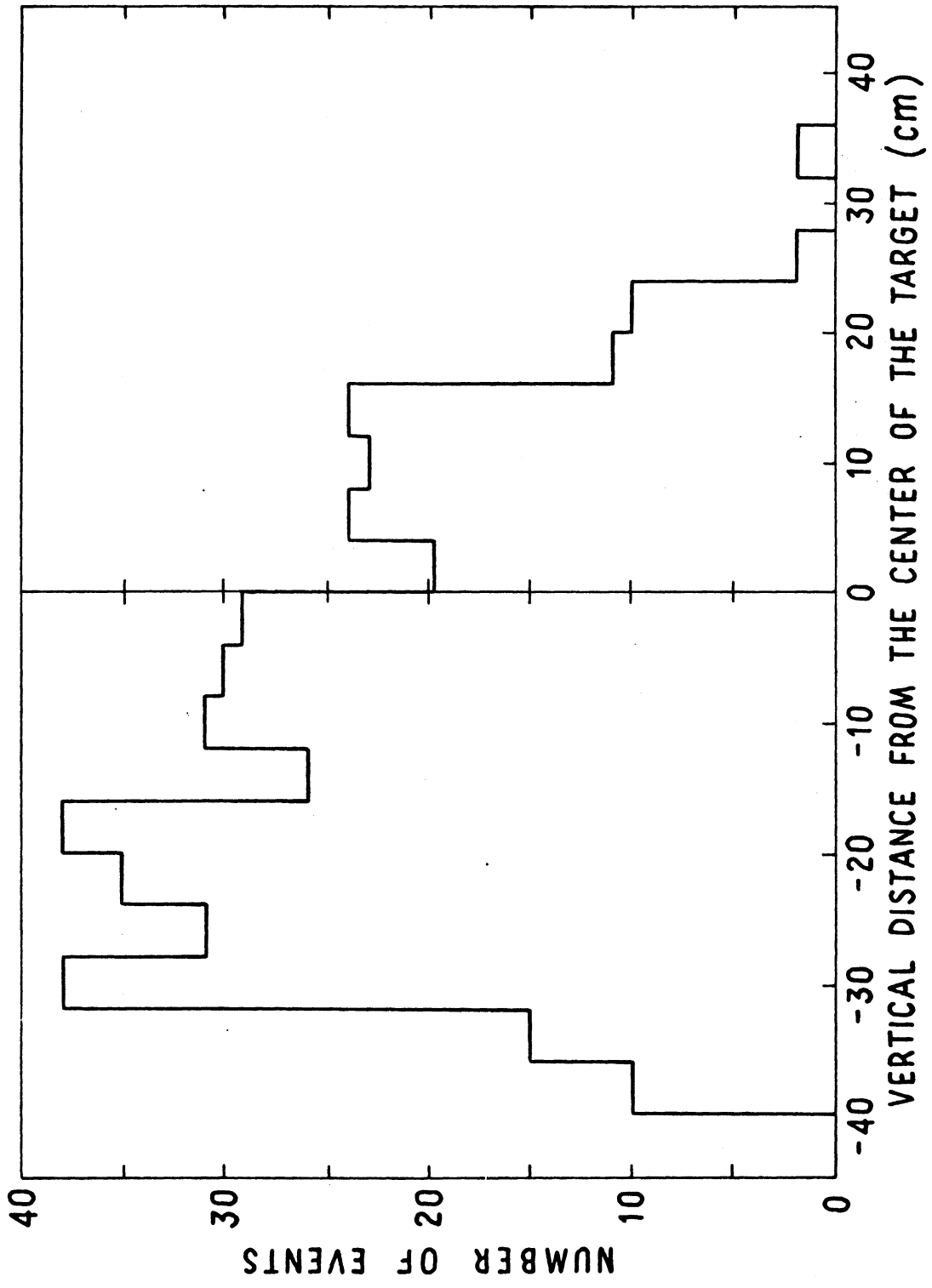

FIG. 35 DISTRIBUTION OF HYDROGEN INTERACTION POSITIONS.

top of the calorimeter. A similar z-vertex bias was not observed if the incident hadron had its first interaction within the calorimeter. If there were a similar z-vertex dependence of the number of events, the line shown in Fig. 31 would have a discontinuity at the scintillator layers. The z-dependence of the number of events which occur above the top of the calorimeter is most probably the result of energy leaving the sides of the calorimeter or energy being dissipated before entering the calorimeter, and not entirely accounted for in the Monte Carlo corrections.

The correction factor necessary to correct the observed proton-proton cross section was derived from the difference between the expected and observed number of target wall interactions. The "corrected number of wall interactions" listed in Table XII corresponds to the scanned number of interactions that occurred in the target walls. Included in this number are two-prong events which were not rejected as δ-rays. The inverse of the "fraction of expected number (of events) Observed" shown in Table XII is the correction factor for the target wall interactions which is close to the cross section correction factor. Since the average position of the liquid hydrogen presented to the beam was 10.1 cm below the average position of the target domes, a correction factor was applied to the hydrogen cross sections that was a linear interpolation between the correction factors of 2.27 for the upper dome and 1.14 for the lower dome. The correction factor for the hydrogen was 91.9 percent of the correction necessary for the iron cross section. The proton-proton cross section data is shown in Fig. 36 and listed in Table XII. It is not clear to what extent differences between the proton-proton and proton-nucleus interactions will affect this correction,

Table XII

Summary of the Interactions Which Occurred in the Walls of the Hydrogen Target and the Renormalized Hydrogen Cross Section.

Average Energy of Bin (GeV)	Total Corrected Number of Particles Incident on Target	Corrected Number of Wall Interactions	Expected Number of Interactions	Fraction of Expected Number Observed	Renormalized Hydrogen Cross Section (mb)
84	2430.4	79.01	129.74	0.6090	30.8 ± 4.7
121	1395.7	40.61	74.20	0.5473	37.3 ± 7.7
172	664.8	26.69	35.49	0.7520	29.4 ± 7.9
249	3318.7	104.69	177.16	0.5909	29.3 ± 3.8
355	1439.2	37.48	76.82	0.4879	44.2 ± 8.9
512	588.5	18.16	31.41	0.5781	27.8 ± 8.8
738	252.0	8.54	13.45	0.6283	30.1 ± 13.7
1198	104.1	3.74	5.56	0.6728	27.2 ± 19.1

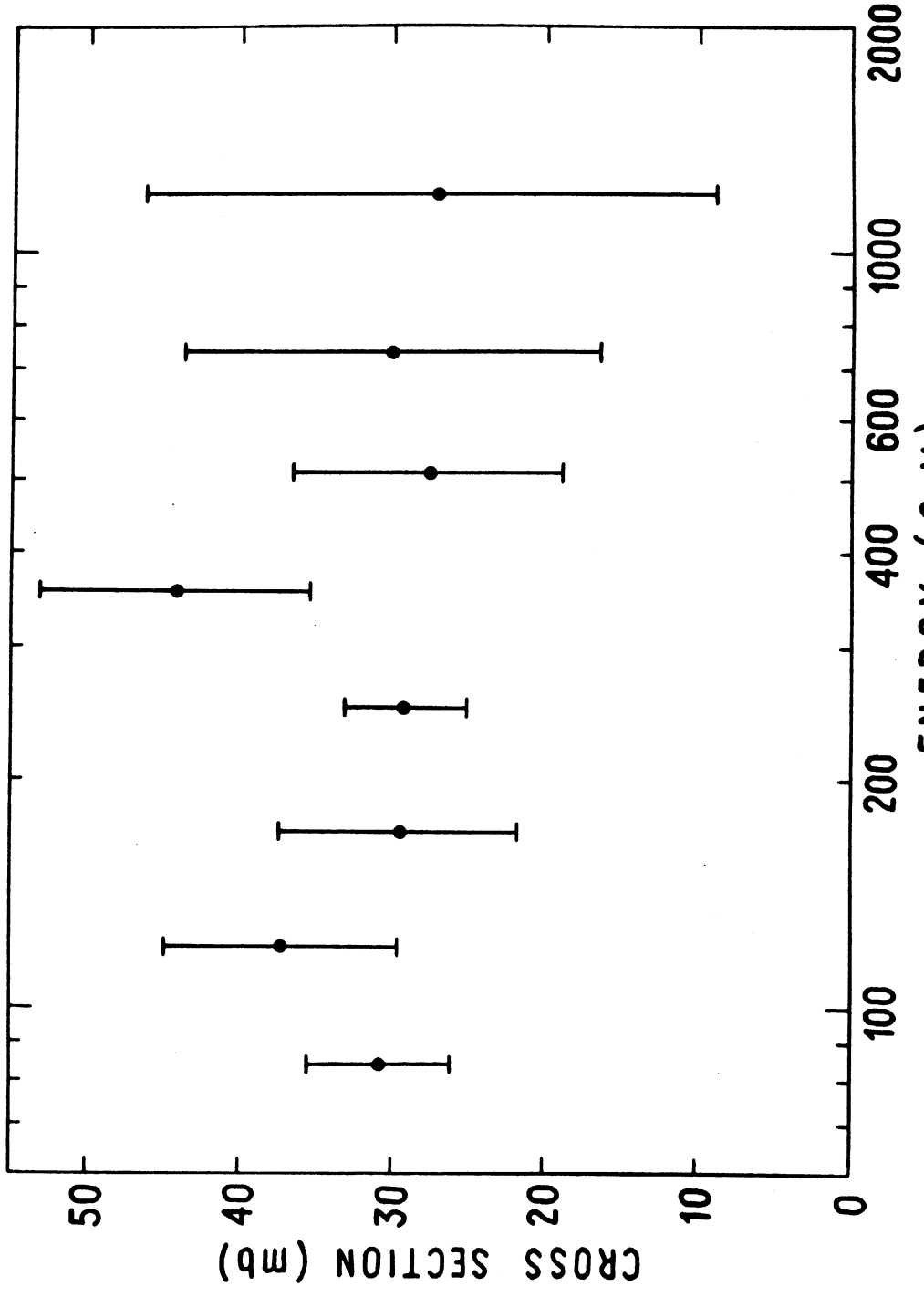

FIG. 36 PROTON-PROTON INELASTIC CROSS SECTION WITH A CORRECTION BASED ON THE PROTON-NUCLEUS INTERACTIONS IN THE TARGET WALLS.

but the proton-nucleus correction is likely to be too large for the hydrogen data. This is because the higher average multiplicity of iron and aluminum interactions may result in more energy escaping both before entering the calorimeter and out the sides of the calorimeter. The proton-proton cross section was recalculated for two energy bins. In an energy bin from 71 to 211 GeV, with an average energy of 109 GeV, the inelastic cross section was 32.4 ± 3.6 mb. For the other energy interval the incident hadrons had a measured energy greater than 211 GeV and an average energy of 342 GeV. The proton-proton cross section calculated for this group of events was 32.3 ± 3.2 mb.

The alternative method of determining the correction factor for the observed proton-proton cross section was the Monte Carlo program for computer generation of events. This Monte Carlo program was discussed in Chapter IV, Section C, and the results of the analysis were presented in Fig. 33. The proton-proton inelastic cross section was presented in Fig. 34, both with and without the Monte Carlo corrections. The corrected cross section calculated for the same two energy bins discussed above was 26.3 ± 2.0 mb at 109 GeV and 23.2 ± 1.5 mb at 342 GeV. These results are different from the cross section which was calculated with a correction determined from the target wall interaction analysis, and they are not a smooth extrapolation of the accelerator data plotted in Fig. 1. There are two apparent weaknesses of the Monte Carlo results that make this correction doubtful. First, the Monte Carlo program did not predict the decrease in the number of observed interactions as the height of the vertex above the top of the calorimeter increases. Second, the method of generating the observed ionization in the scintillators

of the calorimeter did not correctly simulate either the lateral spread or the fluctuations of the real cascades.

CHAPTER V. CONCLUSIONS

The original purpose of this experiment was to make a direct measurement of the proton-proton inelastic cross section. This cross section was determined from the ratio of the number of interacting (multiple-prong) to non-interacting (one-prong) events. Both the events which interacted in the liquid hydrogen and those which did not were grouped into similar energy bins so that the cross section could be calculated as a function of energy. However, because of the steeply falling energy spectrum of incident hadrons, $\propto E^{-3}$, this method of calculating the cross section was very sensitive to small energy biases. A systematically low energy measurement of interacting events relative to non-interacting events resulted in an observed cross section that was about 2/3 of what was expected on the basis of an extrapolation of accelerator data. In order to determine a reasonable correction for the energy bias, the ionization calorimeter used to measure energy was studied in detail.

A study of the first interaction position of incident particles in the calorimeter led to a good experimental measurment of the hadron-iron interaction length. The analysis showed that the corresponding hadron-iron cross section was essentially independent of energy in the interval from 70 to 900 GeV. Although this cross section

$$\sigma_{hFe} = 756 \pm 7 \text{ mb}$$

is somewhat higher than that reported by E. L. Andronikashvili [20], it is consistent with his results. Subsequent corrections to the observed hadron-iron cross section that were used to obtain a proton-iron cross section include some uncertainty. The determined proton-iron cross section was

$$\sigma_{pFe} = 800 \pm 7 \text{ mb} \quad .$$

There is some experimental evidence that the size of this cross section, but not the energy dependence, may be uncertain by as much as 7 percent.

The proton-proton cross sections calculated from the data without a correction for the energy bias were about 20 mb, the necessary correction was based on a comparison of the observed proton-nucleus cross section just discussed. The proton-proton cross sections calculated for two energy intervals with average energies of 109 and 342 GeV were 32 ± 4 and 32 ± 3 mb, respectively. The data indicate that the proton-proton cross section is energy-independent at very high energies. The assumption of an energy independent proton-aluminum cross section was built into these results. However, the uncorrected proton-proton and hadron-iron inelastic cross sections show no energy dependence. The hadron-nucleus cross section determined from the target vessel interactions was energy independent. Thus, the proton-proton cross section corrected with these data was also constant. Results of a Monte Carlo analysis show a larger correction for side leakage at low energies. This indicates that the proton-proton cross section may decrease at higher energies. The proton-proton inelastic cross section results do not distinguish between the three Regge models discussed in Chapter I, Section C.

A proton-iron inelastic cross section that is constant with energy does not necessarily preclude an energy dependent proton-proton or proton-carbon inelastic cross section. Because of the shadowing of particles in the nucleus, the iron cross section may appear almost flat, while the hydrogen and carbon cross sections change. Results of N. L. Grigorov [5] from an attenuation experiment using a carbon target indicate a rising cross section. However, the proton-proton inelastic cross section reported here does not show an increase with energy.

This experiment did not yield an unambiguous measurement of the proton-proton inelastic cross section. The reported cross sections include a correction factor of about 1.6 that was determined for proton-nucleus interactions rather than for proton-proton interactions. The measurements could be improved in either of two ways. One way would be to conduct a similar experiment using an attenuation method to calculate the cross section. The alternative that would also determine the proper correction for this data, is to calibrate the response of the calorimeter for both interacting and non-interacting events. That experiment, which is similar to this one with the exception of an additional magnet and wide gap spark chamber for momentum analysis, is presently under construction at Echo Lake, Colorado [40].

APPENDIX A. CALORIMETER ENERGY MEASUREMENT CORRECTIONS

A single hadron entering the top of the calorimeter interacts and begins a series of nuclear interactions and electromagnetic cascades which ultimately converts most of the energy of the incident particle into ionization in the iron. At each nuclear interaction site, new particles may be produced such as charged pions, neutral pions, and kaons. Nucleons and nuclear fragments may also be emitted from the struck nucleus. The neutral pions quickly decay into γ-rays and start electromagnetic cascades in the iron. The high energy charged mesons and nucleons continue to interact and produce a cascade of hadrons. Among the particles likely to be produced in each successive interaction are neutral pions, which feed the electromagnetic cascade.

The ionization within the iron can be sampled at various depths, and a weighted sum of the number of minimum ionizing particles sampled can be used to calculate an energy for the incident particle. Corrections must be made because the sampled ionization does not represent all of the energy of the incident particle. Two causes of discrepancy will be discussed. These are: 1) a transition effect caused by the difference in critical energy between iron and scintillator, and 2) a poor efficiency for sampling in scintillator the heavily ionizing particles which are produced in a nuclear disintegration. In addition to these, Murzin [22] has calculated that at 50 GeV the neutrinos and fast muons produced by charged pion decay carry away no more than 1 percent of the

energy, and at higher energies the fraction of energy lost in this way becomes even smaller.

1. Transition Effect: The number of minimum ionizing particles in the electromagnetic cascade will be systematically underestimated by the plastic scintillator. Iron has a critical energy $\varepsilon_o \sim 21$ MeV, and the cascade produced in iron will have a larger number of low energy electrons than a cascade produced in scintillator which has a critical energy $\varepsilon_o \sim 70$ MeV. The electromagnetic cascade entering a sampling layer of scintillator will be more quickly absorbed than it is regenerated. Therefore, the amount of ionization sampled is less than the amount of ionization in the iron.

The transition effect was studied experimentally by Crannell, Crannell, Gillespie, Pinkau, and Whiteney [25] using an electron induced cascade. Using their results, the underestimate is about 5 percent for 1.9cm thick scintillator and about 10 percent for 3.8 cm thick scintillator.

2. Nuclear Disintegration: At each interaction site of the nuclear active cascade some of the energy of the incident particle goes into disintegration of the struck nucleus. Various estimates have been made concerning the amount of energy lost in this way. Of special interest is the work of W. V. Jones. It is important to estimate the average fraction of this energy which is sampled in the calorimeter.

The fundamental ideas for interpreting high energy nuclear reactions were first expressed by Heisenberg and Serber [41]. They pointed out that for high energy hadrons incident on a nucleus, the

energy of the incident particle is large compared to the interaction energy of the nucleons with each other. The wavelength of the incident particle is small compared to the average distance between nucleons in the nucleus. Therefore, it is reasonable to think of the incoming particle as interacting with individual nucleons and not with the nucleus as a whole. The struck nucleon or nucleons may be immediately knocked out of the nucleus or may interact with other nucleons before leaving. The extreme case is that in which the recoil nucleon just moves around within the nucleus and does not leave. The recoil nucleon's interaction with other nucleons causes an intra-nuclear cascade. The excited nucleus then evaporates nucleons or clusters of nucleons until it is stable enough to lose energy by longer term processes such as γ emission. Studies of nuclear disintegrations caused by cosmic rays traversing photographic emulsions were reported by Powell, Fowler, and Perkins [42]. This information, along with the response of Nuclear Enterprizes 102 plastic scintillator to heavily ionizing particles as reported by Goodings and Pugh [43], is the basis for the following estimates. Murzin has made similar estimates of disintegration losses for his calorimeter [22].

The nuclear disintegration studies reported by Powell, Fowler, and Perkins used emulsions with an average atomic number of about 80. It was assumed that disintegrations of iron nuclei are similar. The average disintegration energy is 800 MeV, and two "grey" tracks are produced with an average energy of 165 MeV. These "grey" tracks represent recoil protons knocked out of the nucleus by the incident particle.

Since the number of protons and neutrons in a nucleus is roughly equal, an average of two neutrons of comparable average energy would also be produced. Neutrons of this energy travel an average of one collision length before they interact and produce "secondary stars." The ionization resulting from "secondary stars" occurring in the scintillator is predominately due to neutrons from disintegration sites in the iron.

The fraction of disintegration energy measured by sampling the ionization of "secondary stars" produced by recoil neutrons is expressed by the equation:

$$F_N = P_N F_e L_e \quad .$$

In this equation P_N is the average fraction of energy in a "primary star" which is carried away by recoil neutrons. If two neutrons are produced with an average kinetic energy of 165 MeV, then 330 MeV out of 800 MeV is carried by secondary neutrons. The scintillator efficiency term L_e, was necessary because for heavily ionizing particles the light output of scintillator is not directly proportional to the ionization density or energy deposited in the scintillator. The term L_e, estimated for secondary protons having an energy between 10 and 15 MeV, is about 2/3. The fraction of energy that goes into charged particles in "secondary stars," F_e, is about 1/3 of the incident neutron energy. A sizable fraction of the neutron energy supplies the binding energy to the nucleus for release of heavily ionizing particles. Some of this energy also goes into evaporation of very

low energy neutrons from the nucleus. The fraction F_N, is then

$$F_N = \frac{330}{800} \times \frac{1}{3} \times \frac{2}{3} \sim 0.09 \quad .$$

The heavily ionizing evaporation products from "primary stars " occurring in the scintillator will also contribute some measurable ionization. The average fraction of disintegration energy going into the production of these evaporation fragments P_N, is about 1/6 of the total. The evaporation products are similar to those of "secondary stars." The fraction of primary energy measured by sampling the ionization of evaporation products from "primary stars" is

$$F_H = P_H F_e L_e \sim \frac{1}{6} \times \frac{1}{3} \times \frac{2}{3} \sim 0.04 \quad .$$

The charged "grey" tracks produced in "primary stars" will also contribute to the ionization observed. If the "primary stars" occurred in iron, the average percentage of disintegration energy P_P, going into the production of "grey" tracks, mostly recoil protons, is 330 MeV out of 800 MeV. The light output of the scintillator L_P, is almost proportional to the energy going into ionization by a 165 MeV proton. The fraction of observed energy F_P, from the recoil protons produced at disintegration sites in iron is

$$F_P = P_P \times L_P \sim \frac{330}{800} \times \frac{19}{20} \sim 0.39 \quad .$$

Plastic scintillator does not have an atomic number of about 80, but rather an average atomic number for the struck nucleus closer to 12. The nuclear disintegrations that occur within the scintillator will not have as large an intra-nuclear cascade as iron. The number of nucleons struck by the incident particle will be fewer. If both the excitation and the recoil products are roughly proportional to the radius of the nucleus, then carbon has only half the disintegration energy loss of iron. This means that the ionization of "primary stars" which occur in the scintillator is about half of the ionization resulting from "primary stars" which occur in the iron. Therefore, the scintillator samples about half of the ionization from heavily ionizing particles, F_H.

The scintillator also samples energy loss of "grey" tracks of "primary stars" produced in the iron if the interaction site is not too far from the scintillator. The ionization energy loss per centimeter of iron is about five times greater than scintillator. However, the number of nuclear disintegrations per centimeter is also approximately five times larger. "Grey" tracks of an average energy of 165 MeV, have an average path length in scintillator of about five times the thickness used. This means that "grey" tracks produced in the iron close to the scintillator will be sampled quite well. Therefore, F_P is a good approximation for the ionization in iron due to "grey" tracks.

A reasonable estimate for the fraction of disintegration energy in both iron and scintillator that the scintillators sample is

$$F_N + F_P + \frac{F_H}{2} \sim \frac{1}{2} \quad .$$

Murzin has estimated that for a particle incident upon the calorimeter with an energy of 40 GeV, there are 25 "primary stars," for an energy of 300 GeV about 100 "primary stars," and for 1000 GeV about 200. On the basis of Rosenfeld Tables, the ratio of collision lengths of scintillator to iron, for an average layer of this calorimeter, is 0.06. Ionization from the 6 percent of the nuclear disintegrations which occur in the scintillator is measured along with some from the iron close to the scintillator. The ionization which is measured in the scintillator is applied to half the thickness of iron on either side of the scintillator. Therefore, on the average, 1/2 of the energy going into nuclear disintegrations is measured correctly. However, since there are so few sampled disintegrations, what is measured will result in fluctuations of the calculated energy about the true energy.

APPENDIX B. SPECTRUM SHIFTS

The cross section for a target element, in this case hydrogen, can be approximated by the following equation

$$\sigma(E) = \frac{A}{\rho N_o} \frac{1}{\langle z \rangle} \frac{N_I(E)}{N_I(E) + N_S(E)} \quad .$$

In this equation N_o is Avagadro's number, A is the atomic number of hydrogen, ρ the density of hydrogen, and $\langle z \rangle$ the average thickness of hydrogen along the "beam line." The terms N_S and N_I are, respectively, the number of particles which do not interact in the target and the number which do interact. The N's are the number of events in an energy bin, E_k. The differential energy spectrum of the incident particles can be expressed as

$$N(E) = KE^{-\gamma} \quad .$$

γ was determined for this experiment to be about 3. The constant K, properly corrects for the flux entering the fiducial volume chosen. The number of events in an energy bin is then

$$N(E_k) = \int_{E_1}^{E_2} KE^{-\gamma} \, dE = KI(E_k)$$

$$I(E_k) = \frac{1}{\gamma - 1} \left[\frac{1}{E_2^{\gamma-1}} - \frac{1}{E_1^{\gamma-1}} \right] \quad .$$

Suppose that the measured energy of an event interacting in the target is less than if the event had not interacted. Let δ be the fractional energy difference. The number of interacting and non-interacting events can then be written

$$N_I(E_k) = \int_{E_1}^{E_2} K_I(1-\delta)^{-\gamma} E^{-\gamma}\, dE = K_I(1-\delta)^{-\gamma} I(E_k)$$

$$N_S(E_k) = \int_{E_1}^{E_2} K_S E^{-\gamma}\, dE = K_S I(E_k) \quad .$$

The observed cross section for the two fluxes is then

$$\sigma(E_k) = \frac{A}{\rho N_o} \frac{1}{\langle z \rangle} \frac{K_I E^{-\gamma}(1-\delta)^{-\gamma}}{K_S E^{-\gamma} + K_I E^{-\gamma}(1-\delta)^{-\gamma}}$$

$$\sigma(E_k) \simeq \frac{A}{\rho N_o} \frac{1}{\langle z \rangle} \frac{N_{Io}}{N_S + N_{Io}} \frac{1}{(1-\delta)^{\gamma}} \quad .$$

The number of interacting events observed, N_{Io}, are in the energy bin over the interval E_1 to E_2.

It is clear from this last equation that a small shift in the energy spectrum for interacting events will make a large change in the observed cross section. As an example, a $\delta = 0.1$ corresponds to a correction factor of 1.37 in the observed cross section to make it properly normalized. Hence it is evident that this type of experiment is very sensitive to slight energy biases between interacting and non-interacting events.

APPENDIX C. MUON TRIGGERS

High energy muons occasionally lost enough energy within the calorimeter to trigger the hadron coincidence unit. These events were scanned and measured as non-interacting events along with the hadron events which apparently did not interact in the target. The ratio of muon to hadron triggers was

$$R = \frac{r_\mu}{r_h} ,$$

where

$$r_\mu = \int_{E_c}^{\infty} J_\mu(E) P_\mu(E,E_c) F_\mu(\theta) G_\mu(\bar{S}) \, dE \, dA \, d\Omega \, dz$$

and

$$r_h = \int_{E_c}^{\infty} J_h(E) P_h(E,E_c) F_h(\theta) G_h(\bar{S}) \, dE \, dA \, d\Omega \, dz \quad .$$

The subscript μ, refers to muon events and the subscript h, refers to hadron events. The probability that a hadron with incident energy E, greater than 100 GeV would trigger the system is about one.

$$P_h(E,E_c) \simeq 1 \quad \text{if} \quad E > E_c \quad .$$

The angular distribution of the incident hadrons, $F_h(\theta)$, was assumed to be isotropic. The anti-coincidence factor, $G_h(\bar{S})$, is the fraction of particles that do not come associated with showers capable of

giving a signal in the shower counters. The function $J_h(E)$, is the differential intensity of the incident hadrons. The trigger rate of incident hadrons r_h, may be rewritten as

$$r_h \simeq (0.94\ m^2\ sr)\ G(\bar{S}) \int_{E_c}^{\infty} J(E)\ dE \ .$$

This approximation, with $G(\bar{S}) = 1$, was used to determine the integral flux of incident cosmic ray hadrons,

$$\int_{E_c}^{\infty} J(E)\ dE = 3 \times 10^{-7}\ (E/100)^{-2}\ (cm^2\ sec\ sr)^{-1} \ .$$

The trigger rate of incident muons r_μ, was also calculated. The angular distribution of the incident muon flux $F_\mu(\theta)$, is approximately isotropic [44]. Hence, the acceptance for muons was the same as that used for hadrons. Any dependence on the geometrical factor for hadrons $F_h(\theta)$, was not removed from the calculation of the integral hadron flux and therefore is contained in $J_h(E)$. The function $G_\mu(\bar{S})$, is the fraction of muons which are not accompanied by showers which produce a signal in the shower counters. This fraction [45] is

$$G(\bar{S}) = 0.75 \pm 0.15 \ .$$

The function $J_\mu(E)$, is the differential intensity of incident cosmic ray muons and $P_\mu(E,E_c)$ is the probability that an incident particle of

energy E, transfers an energy E_c, in the calorimeter. Thus the ratio of muon to hadron triggers is

$$R = \frac{\int_{E_c}^{\infty} J_\mu(E) P_\mu(E,E_c)\, dE\, dz}{3 \times 10^{-7}(E/100)^{-2}}.$$

The energy dissipated by the incident muon in the calorimeter is the result of three electromagnetic processes: "knock-on" production, bremsstrahlung, and direct pair production. The observed ionization will depend on the position of the electromagnetic cascade with respect to the scintillator. The larger the energy transfer is, the more likely it is that the electromagnetic cascade triggers the calorimeter. As a first approximation assume that only muons with energy greater than 200 GeV contribute to the calorimeter triggers. The probability of an energy transfer greater than 100 GeV by the three electromagnetic processes is

1. "knock-on" production $0.4 \times 10^{-6}/\text{gm cm}^{-2}$
2. bremsstrahlung $1.9 \times 10^{-6}/\text{gm cm}^{-2}$
3. pair production $1.4 \times 10^{-6}/\text{gm cm}^{-2}$

Thus the total probability that more than 100 GeV will be deposited by muons with energy greater than 200 GeV is $3.7 \times 10^{-6}/\text{gm cm}^{-2}$. Since only the first 900 gm/cm^2 of the calorimeter is considered in the trigger, the energy transfer must be contained in this volume. Finally, the flux of incident muons with energy greater than 200 GeV is $2.9 \times 10^{-6}\ (\text{cm}^2\ \text{sr sec})^{-1}$. This integrated muon spectrum is decreasing with energy as E^{-2}.

Inserting this information into the last equation results in an estimate of the ratio of muon to proton triggers

$$R \simeq 0.024 \quad .$$

One of the approximations used in obtaining this result was that only muons with greater than 200 GeV trigger the system. However, even muons with less than 100 GeV could trigger the system by transferring nearly all of their energy into electromagnetic cascades whose peak ionization is sampled. This effect could result in the estimate being a factor of two low. However the ratio of muon to hadron triggers is in the interval

$$0.01 < R < 0.05 \quad .$$

LIST OF REFERENCES

1. Jones, W. V., Physical Review 187, 1868, (1969);

   Jones, W. V., Private Communication, Louisiana State University, Baton Rouge, Louisiana.

2. Erickson, K. N., "Multiparticle Production in Liquid Hydrogen and Carbon by Charged Cosmic Ray Hadrons of Energy Greater than 70 GeV," University of Michigan Report UM HE 70-4, (1970);

   Reeder, D. D., "Some Properties of Proton-Proton Interactions at Energies of 100 to 1000 GeV," Proceedings of the XV International Conference on High Energy Physics, Kiev, USSR, (1970) (to be published);

   Jones, L. W., "Properties of Proton-Proton Interactions Between 70 GeV and 600 GeV," Proceedings of the XI Interamerican Seminar on Cosmic Rays, LaPaz, Bolivia, (1970) (to be published);

   Lyon, D. E., "Proton-Proton Interactions between 90 and 800 GeV/c: Experimental Results from Echo Lake Cosmic Ray Studies," Invited paper for a Symposium on High Energy Interactions and Multiple Particle Production, given at Argonne National Laboratory, November, 1970 (Argonne Report);

   Jones, L. W. et al., Physical Review Letters 25, 1679, (1970);

   Lyon, D. E. et al., "Angular Distribution of Secondaries from Proton-Proton Interactions Above 70 GeV," (1971), (submitted to Phys. Rev. Letters).

3. Galbraith, W. et al., Physical Review 138, B913, (1965);

   Foley, K. J. et al., Physical Review Letters 19, 857, (1967);

   Bellettini, G. et al., Physics Letters 14, 164, (1965).

4. Foley, K. J. et al., Physical Review Letters 11, 425, (1965);

   Harting, D. et al., Nuovo Cimento 38, 60, (1965).

5. Grigorov, N. L. et al., "Measurements of Effective Cross Sections of Inelastic Interactions of Protons with Carbon and Hydrogen Nuclei in the 20-600 GeV Energy Range from the Proton -1,2,3 Satellites," Proceedings of the XI International Conference on Cosmic Ray Physics, Budapest, Hungary, (1969) (to be published).

6. Focacci, M. N. and G. Gaicomelli, "Pion-Proton Elastic Scattering," CERN Report H/154-1500, Geneva, Switzerland, (1966).

7. Reeder, D. D., Private Communication, University of Wisconsin, Madison, Wisconsin.

8. Beznogikh, G. G. et al., Physics Letters 30B, 274, (1969).

9. Gibbard, B. G. and L. W. Jones, "Neutron-Proton Elastic Scattering from 5 to 30 GeV/c," University of Michigan Technical Report, UM-HE-70-11, (1970) (unpublished).

10. Krisch, A. D., Physical Review 135, B1456, (1964).

11. Barger, V. and D. Cline, Phenomenological Theories of High Energy Scattering, W. A. Benjamin Inc., New York, (1969).

12. Barger, V. et al., Nuclear Physics B5, 411, (1968).

13. Cabbibo, N. et al., Nuovo Cimento 45A, 275, (1966).

14. Frautschi, S. and B. Margolis, Nuovo Cimento 61A, 1155, (1968).

15. Berger, V. and R. J. N. Phillips, Physical Review Letters 24, 291, (1970).

16. Bellettini, G., C. Coccini et al., Nuclear Physics 79, 609, (1966).

17. Engler, J. et al., Physics Letters 32B, 716, (1970).

18. Brenner, A. E. and R. W. Wiliams, Physical Review 106, 1020, (1957).

19. Dobrotin, N. A. et al., Proceedings of the IX International Conference on Cosmic Rays, London, (1965).

20. Andronikashvili, E. L. et al., Canadian Journal of Physics 46, 5689, (1968).

21. Ellsworth, R. and G. B. Yodh, "Hadron Spectra in the Atmosphere," Proceedings of the XI International Conference on Cosmic Ray Physics, Budapest, Hungary, (1969) (to be published);

Grigorov, N. L. et al., "The Study of Energy Spectrum of Primary Cosmic Ray Particles of High and Ultra-high Energies from the "Proton" Series of Satellites," Proceedings of the XI International Conference on Cosmic Ray Physics, Budapest, Hungary, (1969) (to be published).

22. Murzin, V. S., Progress in Elementary Particles and Cosmic Ray Physics 9, North Holland Publishing Co., Amsterdam, (1967).

23. Grigorov, N. L. et al., Soviet Physics JETP 7, 348, (1958).

24. Lyon, D. E. and A. Subramanian, "Design of Ionization Spectrometers Using Iron and Scintillators for the Detection of Hadrons in the 100-1000 BeV Range," MURA Report No. 725, (1967) (unpublished).

25. Crannell, C. J. et al., Physical Review 182, 1435, (1969).

26. Ranft, J., "Monte Carlo Calculation of Energy Deposition by the Nucleon-Meson Cascade and Total-Absorption-Nuclear Cascade (TANC)," Rutherford High Energy Laboratory, Berkshire, England (preprint).

27. Hughes, E. B., R. Hofstadter et al., Nuclear Instruments and Methods 75, 130, (1969).

28. Denisov, E. V. et al., Proceedings of the IX International Conference on Cosmic Rays, London, (1965).

29. Rich, R. and R. Madey, "Range-Energy Tables," UCRL 2301, (1954).

30. Lyon, D. E. et al., "Angular Distribution of Secondaries from Proton-Proton Interactions Above 70 GeV," (1971), (submitted to Physical Review Letters).

31. Rossi, B., High Energy Physics, Prentice-Hall, Inc., Englewood Cliffs, N. J., (1952).

32. Wilson, R. R., Physical Review 84, 100, (1951).

33. Pal, Y. and B. Peters, Danske Videnshahernes Selskab: Matematisk-Fysiske Meddelelser 33, No. 15, 3, (1964).

34. Viswanath, P. R., Private Communication, University of Michigan, Ann Arbor, Michigan.

35. Ramana Murthy, P. V., Private Communication, Tata Institute of Fundamental Physics, Bombay, India.

36. Ramana Murthy, P. V., et al., Nuclear Instruments and Methods 23, 245, (1963).

37. Sievers, P., Externer Bericht 3/68-12, Institute fur Experimentelle Kernphysik, Keinforschungszentrum Karlsruhe, Karlsruhe, (1968).

38. Parker, E. F. and L. W. Jones, "Neutron-Proton, Neutron-Deuteron, and Neutron-Nucleus Total Cross Sections at 4.0 GeV/c and 5.7 GeV/c," The University of Michigan Technical Report 03028-3-T, (1969) (unpublished).

39. Allaby, J. V. et al., "Measurements of total cross sections for negative particles on protons in the momentum range 20-65 GeV/c," Proceedings of the Lund Int. Conf., on Elementary Particles, Lund, Sweden, (1969) (to be published).

40. Jones, L. W. et al., "Properties of Proton-Proton Interactions Between 70 GeV and 600 GeV," Proceedings of the Sixth Interamerican Seminar on Cosmic Rays, La Paz, Bolivia, (1970), (to be published).

41. Heisenberg, W., Naturwissenschhafter 25, 749, (1937);

Serber, R., Physical Review 72, 1114, (1947).

42. Powell, C. F., P. H. Fowler and D. H. Perkins, The Study of Elementary Particles by the Photographic Method, Pergamon Press, Inc., New York, (1959).

43. Gooding, T. J. and H. G. Pugh, Nuclear Instruments and Methods 7, 189, (1960).

44. Meada, K., Goddard Space Flight Center, Greenbelt, Maryland, Report No. X-640-63-236, (1963).

45. Wolfendale, A. W., Proceedings of the VII International Conference on Cosmic Rays, vol. 6, 3, Jaipur, (1963).